Developing Nanoparticles as Contrast Agents for Cell Labelling and Multimodal Bioimaging

Thesis submitted in accordance with the requirements of the University of Liverpool for the degree of Doctor in Philosophy by

Oihane Fragueiro

APRIL 2018

Acknowledgements

First, I would like to thank my supervisors for giving me the opportunity to pursue my PhD. I would like to thank especially, Prof. Mathias Brust for all his support through the past years, especially in the tough moments. His guidance helped me in all the time of research and writing of this thesis.

Second, I would like to thank to Dr Joan Comenge for all the time he spent helping me in the lab, his patience as a mentor, advice, the stimulating discussions during the coffee time, for the thesis prove reading and a long list of things that he has done for me and have contributed greatly to this thesis. But more importantly, I am truly grateful for his friendship and his support in the tough moments; my time in Liverpool would have not been the same without him.

My sincere thanks also go to Dr Domagoj Belic for the ESEM, CryoTEM and HRTEM pictures as well as for all his advices and to Dr Marcin Grzelczak, for his help and advice with the persistent luminescence nanoparticles.

This thesis involved a multi-disciplinary work and many people from other groups contributed to the work presented. I would like to thank Dr Patricia Murray for giving me the chance to work in her lab and everybody from her group for the help with the cell culture. Especially, I would like to thank Jack Sharkey for the intracardiac and subcutaneous injections.

Finally, I would like to thank to all the members of the Brust group for creating a really nice atmosphere in the lab and in the office as well as to all the friends I made in Liverpool for all those fun moments.

Abstract

Emergence of new bioimaging technologies requires the development of the most appropriate contrast agents for each application. In this thesis, we present the development of gold nanorods (GNRs) and chromium doped zinc gallium oxide (ZGO:Cr) for labelling mesenchymal stem cells (MSCs), which enabled multimodal *in vivo* monitoring of cells. GNRs are excellent contrast agents for Multispectral Optoacoustic Tomography (MSOT) due to the high absorbance of their longitudinal surface plasmon resonance (LSPR) in the Near Infrared (NIR) region of the electromagnetic spectrum. Persistent luminescent nanoparticles such as ZGO:Cr have arisen as promising optical *in vivo* probes due to their long emission lifetime, in the order of minutes.

First, NPs were synthesised and their surface was modified to improve colloidal stability, biocompatibility and cell uptake. GNRs were prepared by the seed-mediated growth method, and modified *via* ligand exchange using a small thiolated PEG with a carboxylic acid terminal group. For ZGO:Cr a hydrothermal approach was followed and surface was modified with DMSA. Interactions with cells and how these interactions affect the optical properties of the nanoprobes have been also studied here.

To follow a multimodal imaging approach, MSC cells were co-incubated with PEG-COOH-GNRs and DMSA-ZGO. Imaging by means of MSOT and optical imaging was conducted after subcutaneous injection, and also after intracardiac administration of labelled cells. The combination of different imaging modalities is frequently required to overcome limitations of a particular technique. In our case, MSOT offered great resolution deep into the body, enabling sub-organ localisation of labelled cells, which is not possible with pure optical-based techniques. However, organs such as lungs and stomach cannot be visualised and endogenous absorbers with similar optical spectrum than GNRs could lead to false positives. On the other side, persistent luminescence did not present those limitations, however its spatial resolution is much worse than MSOT. Therefore, the two imaging modalities complemented each other to have a more accurate view of the process.

Publications

1. Comenge, J., Fragueiro, O., Sharkey, J. *et al.* Preventing Plasmon Coupling between Gold Nanorods Improves the Sensitivity of Photoacoustic Detection of Labeled Stem Cells in Vivo. *ACS Nano* **10,** 7106–7116 (2016).

2. Comenge, J., Sharkey, J., Fragueiro, O. *et al.* Multimodal cell tracking from systemic administration to tumour growth by combining gold nanorods and reporter genes. *eLife* **7,** e33140 (2018).

Table of Contents

Abbreviations

CCD	Charge-Coupled Device
MRI	Magnetic Resonance Imaging
CT	Computed Tomography
PET	Positron Emission Tomography
SPECT	Single Photon Emission Computed Tomography
US	Ultrasound
PAI	Photoacoustic Imaging
NIR	Near Infrared
PL	Persistent Luminescence
LPP	Long Persistent Phosphors
ICG	Indocyanine Green
MSOT	Multispectral Optoacustic Tomography
OPO	Optical Parametric Oscillator
QDs	Quantum Dots
GNP	Gold nanoparticles
FDA	Food and Drug Administration
SPIONs	Super paramagnetic Iron Oxide NPs
MIONs	Magnetic Iron Oxide NPs
USPIONs	Ultra-small Paramagnetic Iron Oxide NPs
RES	Reticuloendothelial System
SPR	Surface Plasmon Resonance
TSL	Thermally Stimulated Luminescence
GNRs	Gold Nanorods

TSPR	Transverse Surface Plasmon Resonance
LSPR	Longitudinal Surface Plasmon Resonance
RMT	Regenerative Medicine Treatments
GFP	Green Fluorescent Protein
BLI	Bioluminescence Imaging
SAMs	Self-assembled Monolayers
CTAB	Cetyltrimethylammonium Bromide
AR	Aspect Ratio
PEG	Polyethylene Glycol
BSA	Bovine Serum Albumin
EDAC	N-(3-Dimethylaminopropyl)-*N′*-ethylcarbodiimide hydrochloride
NHS	*N*-Hydroxysuccinimide
DLS	Dynamic Light Scattering
FT-IR	Fourier-transform Infrared
CPP	Cell Penetrating Peptides
TAT	Transactivator of Transcription
PLNP	Persistent Luminescent Nanoparticles
ZGO:Cr	Chromium-doped Zinc Gallium Oxide
APTES,	3-Aminopropyl)triethoxysilane
DMSO	Dimethyl Sulfoxide
DMSA	*meso*-2,3-Dimercaptosuccinic Acid
PLNPs	Persistent Luminescent Nanoparticles
PVP	Poly(vinylpolypyrrolidone)
PAH	Poly(allylamine hydrochloride)
EDX	Energy-dispersive X-Ray Spectroscopy
(HR) TEM	High Resolution Transmission Electron Microscopy
CM	Cell Membrane

MPS	Mononuclear Phagocyte System
CDE	Caveolae-dependent Endocytosis
CIE	Chlatrin/caveolae Independent Endocytosis
CME	Chlathrin-mediated Endocytosis
IVIS	*in vivo* Imaging System
DMEM	Dulbecco’s Modified Eagle Medium
PBS	Phosphate-buffered saline
FBS	Fetal Bovine Serum
O.D	Optical Density
PFA	Para-formaldehyde
ESEM	Environmental Scanning Electron Microscopy
MSCs	Mesenchymal Stem/Stromal cell line
AUC	Area Under the Curves
IC	Intracardiac

Chapter 1

Introduction

1.1 Bioimaging: General concepts

Imaging techniques are indispensable tools in both clinical and preclinical studies. They have an important role in the development of different fields of study such as drug delivery, cancer diagnosis, guided surgery and stem cells therapies among others.[1] They can be divided in two main groups: anatomical imaging used in the clinics on a routine basis and molecular or functional imaging.[2] The second group is attracting a lot of attention recently because it provides not only anatomical information, but it also can be used to evaluate physiological processes such as clearance of a specific drug or follow relevant physiological or cellular processes *in vivo*.[3]

Different imaging methodologies are available, and each one presents different advantages and disadvantages. For example, purely optical-based imaging techniques are based on the detection of photons by a charge-coupled device (CCD) and are ideal for molecular imaging due to their high sensitivity and the possibility to work with multiple wavelengths.[4] However they are limited to very superficial regions due to their lack of resolution at depths beyond a few mm.[5] On the other hand, other methods such as MRI are powerful enough for imaging whole human body, although they are not as versatile as optical imaging in terms of molecular imaging, and they are also not as sensitive as other methods.[6] Table 1.1 summarizes the main characteristics of the most relevant imaging techniques. The selection of the appropriate imaging method and contrast depends on the type of information desired, the target and the depth of imaging required or thickness of the subject.

Optical-based *in vivo* imaging techniques have a remarkable sensitivity, being able to detect probes in a concentration picomolar range.[7] Techniques based on light in the visible region of the spectra are usually limited to *in vitro* studies due to tissue absorption. Hence, the most used optical-based techniques for in vivo imaging are based on the use of NIR light (See section 1.2.1).[8] Due to their high sensitivity, NIR luminescence imaging is a valuable tool in molecular imaging. [8] In addition, its low cost and user-friendly handling make it a popular technique in many different fields. However, one of the main limitations of these methods is the scattering of photons by biological tissues, which results in a poor anatomical resolution, which is down to 1-2 mm in superficial regions since the penetration depth is less than 1 cm.[9] The principles and some examples of optical-based imaging technologies are fully discussed in section 1.2 of the introduction.

Other bioimaging techniques such as magnetic resonance imaging (MRI) or X-ray-based techniques do not have the penetration depth limitation seen for optical-based techniques.[6] MRI is a non-ionizing imaging technique broadly used in clinical diagnosis. The endogenous contrast is based on the measurement of relaxation times of protons in molecules (such as water, lipids, proteins, etc.) after applying a strong magnetic field followed by radio frequency pulse at a resonant frequency.[10] One of its most useful characteristic is the possibility to image soft tissues.[11] Other assets of this technique are high spatial resolution (down to 50 µm) and no limits in penetration depth.[6] However, high cost and the need of highly specialised staff might limit its use in research. In addition, due to its relatively low sensitivity (which is in the range of nmols to mmols) the use of exogenous contrasts is usually needed.[12] These contrast agents are classified according to the type of relaxation: positive or T1 contrasts agents such as Gadolinium(Gd)-based composites[13] and negative or T2 contrast agents such as iron oxide NPs[14].

X-Ray computed tomography (CT), known as well as CAT scan (computed axial tomography), is also a well-established imaging technique in the clinical diagnostic toolbox due to its high resolution and penetration depth.[6] It is based on the changes in absorption of X-Rays by different tissues; hence it is an ionizing method. However, its safety profile has significantly improved during the last decades. This was achieved thanks to the replacement of carcinogenic thorium NPs as X-Ray contrasts by safer hydrophilic iodinated molecules.[15] Since early 2000, CT-Scan has been coupled to positron emission tomography (PET), a nuclear medicine functional imaging system approved by the FDA.[16] PET is based on the detection of gamma rays emitted by a radioisotope without the need of any external excitation source. It is the most sensitive imaging method available, allowing the detection of a single abnormal cell.[17]In addition, it does not suffer from penetration depth limitations. Single photon emission computed tomography (SPECT), is also based in gamma ray detection. Although the sensitivity is one order of magnitude lower than PET imaging, it allows multiplexing, i.e. imaging different molecular targets simultaneously.[8] However, the poor spatial resolution (1-2 mm) is the main inherent drawback of the methods along with the high cost due to the production and storage of radioactive materials.[18] Ultrasound (US) is another broadly used technique in clinical diagnosis due to its innocuous and inexpensive nature. It is based on the detection of sound waves above 20 KHz (2-3 MHz in paediatrics and 5-12 MHz in adults).[6] Finally, photoacoustic imaging (PAI) is a novel technique that combines the high sensitivity of optical methods with the spatial resolution of ultrasounds.[19] This method will be further discussed in section 1.2.3.

Technique	Sensitivity	Resolution	Penetration depth	Cost
PAI	pmol	50 µm	< 5 cm	Low
X-Ray/CT scan	µmol	50 µm	No limit	High
US	nmol	50 µm	Several cm	Low
MRI	nmol	50 µm	No limit	High
PET/SPECT	fmol	1-2 mm	No limit	High
Optical	pmol	1-2 mm	< 1 cm	Low

Table 1.1: Table of features of different imaging techniques. Adapted from reference 6.[6]

1.2 Optical-based Bioimaging

1.2.1 Near Infrared (NIR) Window

In the body tissue, there are endogenous molecules that absorb in the UV-vis-NIR region of the electromagnetic spectrum. These molecules are mainly melanin, oxygenated and deoxygenated haemoglobin and water.[20] The absorbance and scattering of light by these molecules are minimal in the near infrared (NIR) region. This is the so called therapeutic or NIR window (figure 1.1 A).[21] For this reason, probes with a sharp or intense NIR absorption or emission such as GNRs (Figure 1.1 B) are often preferred as contrast agents for optical *in vivo* imaging.[5]

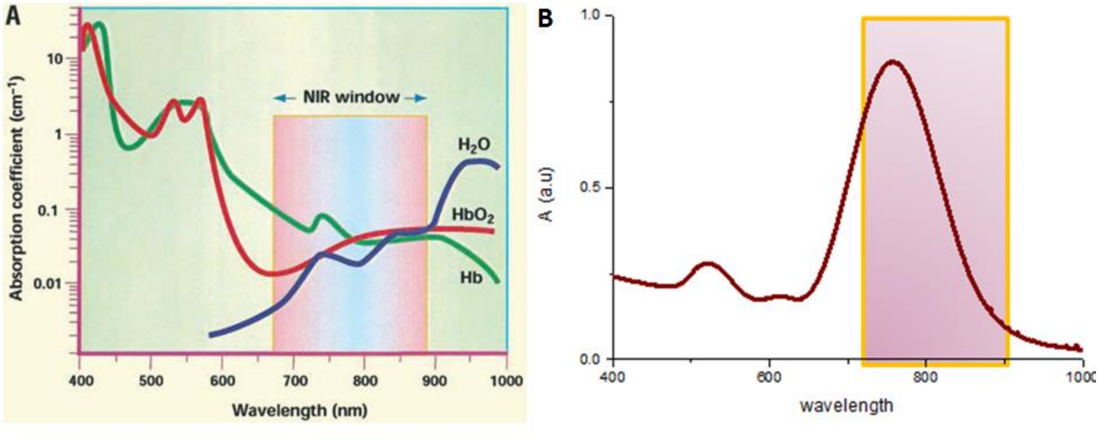

Figure 1.1: A) NIR window. Absorbance of water, oxygenated deoxygenated haemoglobin. From reference 21.[21]B) GNRs UV-VIS spectrum. NIR window range is shown in pink.

1.2.2 General Bases for Luminescence-based Optical Imaging

Luminescence is a process where a substance emits light other than as result of heat. It has been defined as "a spontaneous emission of radiation from an electronically excited species (or from a vibrationally excited species) not in thermal equilibrium with its environment".[22] Therefore, luminescence is a type of cold body radiation and thus it is distinguished from incandescence. Depending on the source of excitation, luminescence can be divided in different categories such as chemiluminescence (excitation source: chemical reaction), crystalloluminescence (crystallisation), mechanoluminescence (mechanical action on a solid), radioluminescence (ionizing radiation), photoluminescence (absorption of photons) or thermoluminescence (enhancement of emission by heat after excitation by other means, usually light) among others.

Fluorescence and phosphorescence are different categories of photoluminescence. For a long time the distinction between both was made based on the emission lifetimes which is usually in the range of nanoseconds for fluorescence and milliseconds to hours in the case of phosphorescence. However, this criterion is no longer accurate.[23] There is a difference in the electronic configuration of the excited state. Fluorescence is a result of the relaxation of an electron from the excited singlet state (S_1) to the ground state (S_0). On the other hand, phosphorescence is a result of the relaxation from an intermediate state, the triplet excited state (T_1). This is described in a simplified Perrin-Jablonski diagram in figure 1.2.

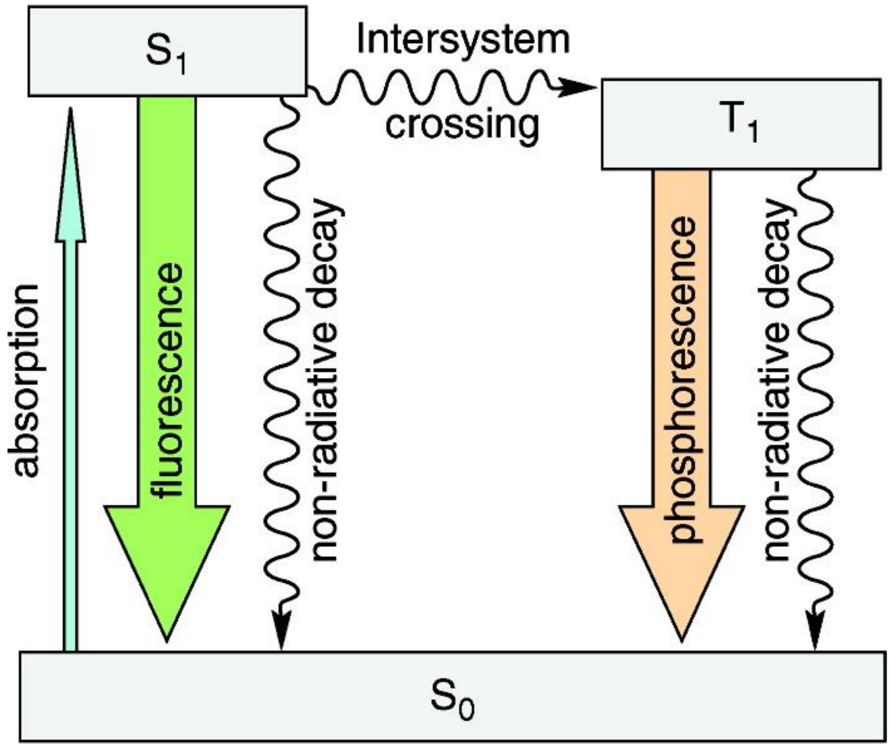

Figure 1.2: Schematic representation of Perrin-Jablonski diagram showing fluorescence and phosphorescence. From reference 24.[24]

Persistent luminescence (PL) is a phenomenon where inorganic phosphors, called long persistent phosphors (LPP), emit for long emission times from minutes to hours, similarly to phosphorescence.[25] Unlike the latter, PL does not rely in the triplet-to-singlet transitions. PL involves four steps, excitation, storage, release and recombination of charged carriers.[25] LPP can store the optical energy and release it progressively after excitation by UV, vis or NIR light.[26] This is another type of photoluminescence called photostimulated luminescence (PSL). For this reason, LPP are also called optical batteries. The charge carriers are captured in traps, which are electronic levels below the conduction band.[27] These traps are the result of defects that can be either intrinsic defects (defects in the crystal lattice) or extrinsic defects (impurities or dopants).[25] In addition, PL is a type of thermoluminescence that occurs at room temperature. Therefore, the driving force for de-trapping the electrons is heat. The state of the art of long persistent nanoparticles describing mechanism proposed for the chromium-doped zinc gallium oxide (ZGO:Cr) NPs in more detailed is described in section 1.3.1.

1.2.3 Photoacoustic Imaging (PAI): A novel hybrid method

Macroscopic optical imaging methods have arisen as an answer to the low penetration depth of traditional microscopy techniques. Although the latter techniques can achieve subcellular spatial resolution, they are limited to cell imaging in tissues and do not allow cell tracking studies in the entire organism.[5] Hybrid methods like PAI, also called optoacoustic imaging, were designed to overcome some of the limitations of purely optical-based techniques. The advantages of this technique are good spatial and temporal resolution as well as a high sensitivity. The high temporal resolution (real time acquisition)[28] enables functional analysis of pharmacokinetics and pharmacodynamics.[5] For instance, the clearance of indocyanine Green (ICG) was successfully studied *in vivo*.[29] The penetration depth is considerably improved compared to traditional optical imaging; it can achieve up to 5 cm with a resolution of < 1 mm (up to 50 µm in some systems).[30] This is thanks to the wave component of the technique since the scattering coefficient in biological tissue of USs is 2 or 3 magnitudes lower than photons.[31] This allows the use of this technique in the imaging of small animals in preclinical studies[32,33] or superficial organs imaging in the clinic such as breast lesions.[34]

PAI is based on the photoacoustic effect first described by Alexander Graham Bell in 1881. It describes the ability of a material to produce a sound wave after absorption of light: “Sonoreusness, under the influence of intermittent light, is a property common to all matter”. [35] Although this effect, inherent to different materials, has been known for over a century, its use in bioimaging has only been proposed in the last decades. It relies on the ability of a chromophore to absorb light and generate a subsequent sound wave that can be recorded and processed into images (figure 1.3). As a consequence of absorption of electromagnetic energy, a thermoelastic expansion is generated by local heat produced by electron relaxation. This ultimately generates a pressure wave that can be a recorded as an ultrasound signal.[36] Multispectral Optoacustic Tomography (MSOT) is a variant of PAI that uses a multi-wavelength approach. A monochromatic pulsed laser at an excitation wavelength of 520 nm and a 120 mJ pulse energy is used. An Optical Parametric Oscillator (OPO) tunes the wavelength in single nanometre steps.[29]

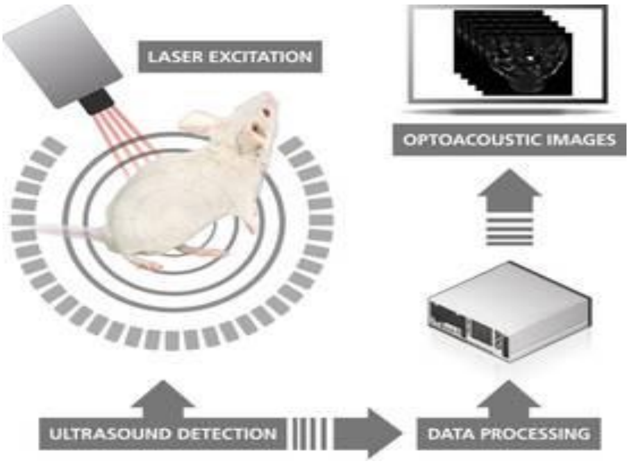

Figure 1.3: Diagram showing the different elements of MSOT technology. From Ithera website.

1.3 Nanoparticles as imaging agents

Nanoparticles have proved to be valuable tools in bioimaging due to the improvement in signal intensity and stability compared with traditional molecular contrasts. Quantum dots (QDs) are a good example of this. Their higher quantum yield, photo-stability broad excitation spectra and narrow emission spectra compared to organic dyes offer a good alternative for optical imaging.[37] In addition, NPs have potential for higher avidity (multiple ligands per NP) and improved targeting efficacy through surface modification (longer circulation times, multimeric binding…). NPs also offer the possibilities for multiplexing (i.e. imaging different targets simultaneously) due to the improved and defined optical properties. In the specific case of cell tracking, the use of reporter genes involves the genetic modification of cells, which could be a drawback, especially at the clinical stage. An alternative to this approach is the use of gold nanoparticles (GNP) as exogenous contrast agents. However, the main drawback of using NPs for cell tracking is the dilution of the signal after sequential cell divisions. Therefore, the use of NPs is restricted to relatively short-term cell tracking.

Nonetheless, several types of NPs have been adapted to imaging in humans. The Food and Drug Administration (FDA) has approved NP-based contrast agents for different imaging methods.[38] Colloids have been used in radionuclide imaging for years as carriers of radiolabelled isotopes. The most common radioisotope used in SPECT is ^{99m}Tc[39]. Sulphur colloid is the most widely used carrier for SPECT in USA, ^{99m}Tc-sulfur is indicated for breast cancer and melanoma imaging.[40,41] In Europe the most popular carrier is colloidal albumin that can be used for bone marrow imaging.[42] Iron oxide nanoparticles coated with different polymers such as dextran have also been approved by the FDA for human use (ferumoxtran, ferucarbotran and ferumoxytol). These NPs are the most important T2 contrast agents for MRI imaging. According to their size, they can be classified as magnetic iron oxide NPs (MIONs) when they are 50 µm, superparamagnetic iron oxide NPs (SPIONs) when size is bigger than 100 nm and ultra-small paramagnetic iron oxide NPs (USPIONs) when size is lower than 50 nm. SPIONs are indicated for the clinical use in the diagnosis of liver diseases.[43] USPIONs, on other hand, are used for lymph-node imaging, angiography, and blood-pool imaging.[44] Although SPIONs have a large potential for a host of clinical applications (such as stem cell tracking), some of the preparations previously used in humans have been held up due to worries related to their immunogenicity. Only ferumoxytol (Polyglucose sorbitol carboxymethylether-coated iron oxide) is currently being used due to its small size and longer circulation times. [45]

In addition, many nanoparticles that promise potential to improve current contrast used in the clinic are being subject to study. Composites based on iodinated organic molecules loaded into nano-structures have received a lot of attention as they can enhance the local contrast due to confinement of commonly used iodinated molecules and improvement of circulation times. Different strategies such as liposomes[46], lipoproteins[47], nano-milled insoluble compounds[48], and polymeric NPs[49] have been already successfully tested in animals. In addition, GNPs have also been proposed as X-Ray contrasts[50,51]. Interestingly, GNPs were shown to be comparable or even better than conventional X-Ray contrasts for mammography and trans-torso imaging[52].

However, there are some problems associated with the use of NPs as imaging probes. Minimizing batch to batch difference and improving characterisation methods is a requirement before NPs can become a reality in the clinic. It is also important to fully understand NPs behaviour in biological environments (i.e. NP-biomolecules interaction) in order to design more effective NP in a rational manner. NPs intended for the use as imaging probes need to fulfill a list of requirements. First, colloidal stability should be maintained in a variety of physiological environments (resistant to differences in pH, ionic strength or temperature). A good contrast quality needs to be provided. This is a high quantum yield (fluorescent probes), high signal-noise ratio or high extinction coefficient for PAI probes. In addition, for those NPs that will be injected systemically, non-specific binding needs to be minimized to reduce entrapment by the reticuloendothelial system (RES). This leads to longer retention in the blood and hence increasing imaging times. Similarly, if NPs are intended for cell tracking, cell uptake should be maximized to mitigate the signal dilution effect after cell division.

1.3.1 Persistent luminescent NPs (PLNP)

Advances in the synthetic routes of long persistent phosphors (LPP) have enabled the synthesis of these kinds of materials in the nanometre range. The most relevant synthetic approaches are described in chapter 3. Persistent luminescent nanoparticles (PLNP) are divided in two different components; the activators and the hosts. Activators or emitting centres are usually transition metals (such as Mn^{2+} or Cr^{3+})[53,54] or rare earth ions (such as Eu^{2+}, Ce^{3+}, Eu^{3+}, Pr^{3+} or Tm^{3+})[55,56,57,58] into the host. Activators are responsible for the emission wavelength while the host provides the defects needed for the traps. Therefore, luminescence duration and intensity are attributable to them. Cr^{3+} is an excellent dopant for in vivo imaging due to its $^3d_3$ electronic configuration that allows results in a narrow band emission at 700 nm (figure 1.5 A).[25]

$Ca_{0.2}Zn_{0.9}Mg_{0.9}Si_2O_6$ NPs, synthesized by Chermont *et al* were the first LPNPs used for *in vivo* imaging.[59] NPs had to be pre-activated by UV light before injection, limiting the imaging time[59] (Figure 1.4). In 2013, Liu and co-workers published a new LPP material; $LiGa_5O_8$:Cr discs which were synthesized by solid state chemistry and could glow for over 1000 hours after UV excitation. They described a new phenomenon. This material showed a renewable luminescence after being excited with a lower energy using a LED lamp. They named this optical property photo-stimulated persistent luminescence (PSPL). The discs could be recharged for more than 20 times, prolonging, the life of the phosphor to over 2000 hours.[60] They also synthesized different sizes of rechargeable $LiGa_5O_8$:Cr NPs using a sol-gel approach and were able to use them as *in vivo* contrasts for 10 days.[61] In 2014, Maldiney *et al* also described this behaviour for $ZnGa_2O_4$:Cr. This material possesses a main advantage over $LiGa_5O_8$:Cr NPs. They do not need to be pre-charged by UV light.[62]

Maldiney *et al* also proposed a mechanism for this unexpected optical behaviour (Figure 1.5).

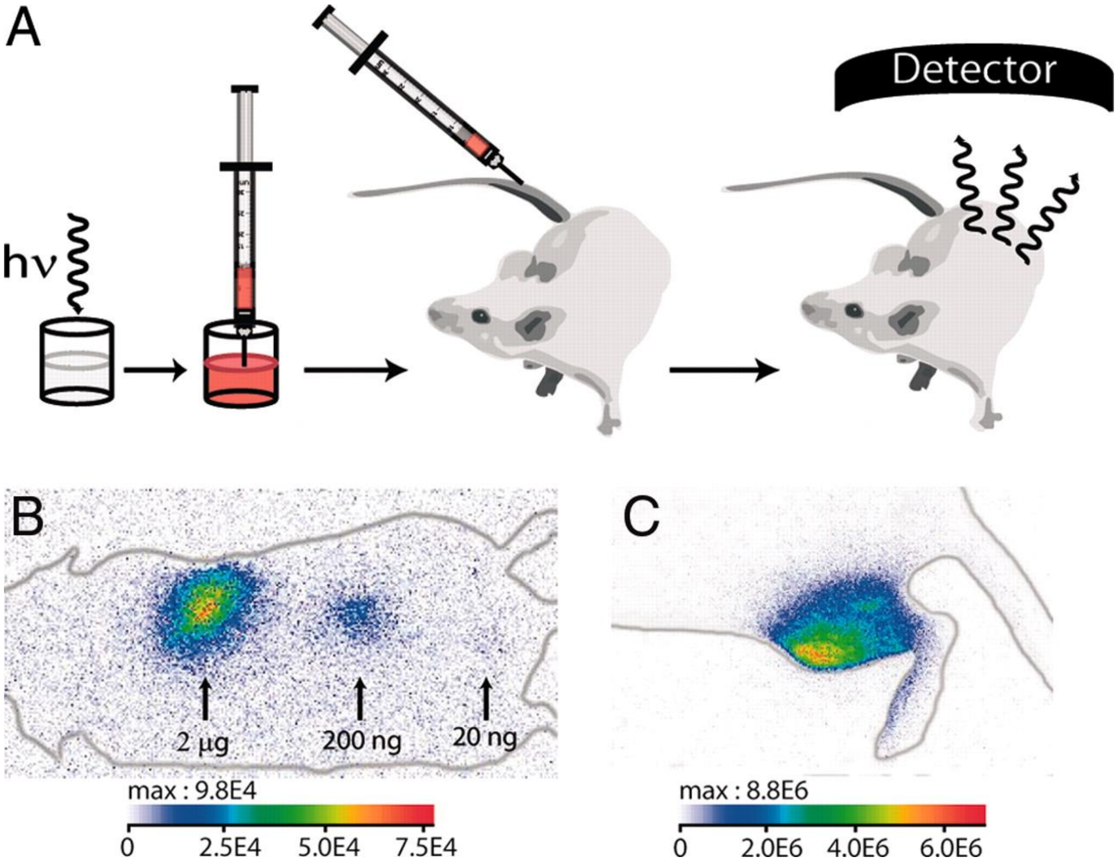

Figure 1.4: A) Activation and *in vivo* imaging of PLNPs. B) Image of subcutaneously injected PLNPs. C) Image of PLNPs after intramuscular injection. Intensity is expressed in photons per s·cm^2·steradians (sr). From reference 59.[59]

Most of the ZGO nano-crystal has a spinel structure except from around the 3%, which exhibit an inverse character.[63] In an inverse spinel structure, Gallium atoms occupy Zn position and *vice versa*, this is referred as antisite defects. A deeper discussion on crystal structure of ZGO can be found in chapter 3 (subsection 3.4.1). There are different types of Cr^{3+} ions in the ZGO:Cr crystal. The most relevant, from a mechanistic point of view are, $Cr_{R,}$ which are Cr^{3+} ions free of neighbouring defects, and Cr_{N2} which are ions close to an antisite positive defect ($Ga^{\bullet}_{Zn}$), i.e. when a gallium ion is occupying a Zn position. Bessière *et al.* proposed that the LPP triggered by visible light is mainly ascribed to Cr_{N2}.[64] This is based on the observation that after exciting the crystal at ~3.1 eV, electron-hole pair formation can be seen all over the material.[64] On the contrary, when the excitation is below ~3.1 eV, i.e. orange-red light, electron hole migration is restricted to the vicinities of $Cr_{N2.}$[65] Figure 1.5 B shows the energy level diagram of Cr_{N2} and the mechanism of LPP after visible light excitation proposed by Maldeney *et al.*[59] This mechanism is based on the observations made by Bessière *et al* and the change of thermally stimulated luminescence (TSL) spectrum when excitation is higher or lower than 3.1eV.[64] It shows that the excited state of the activation centre (Cr_{N2}) is located in the band gap, 0.6-1 eV below the conduction band. The LLP process proposed here is divided in four steps; first, Cr^{3+} ion is promoted to the excited state after light irradiation, when excitation source is visible light, it promotes to the $^4T_2$ state leading to a charge redistribution of positive and negative defects, $Ga^{\bullet}_{Zn}$ and Zn'_{Ga} respectively (step 2), the local charge created by the defects is the driving force to "hold" the electron-hole pair trap by interaction with the charged defects and forming a relatively stable and neutral state; Ga^{x}_{Zn} and Zn^{x}_{Ga}. The third step involves the detrapping of the electron-hole, it is triggered by thermal activation. LPP is one type of TSL which energy of trap depth is low, from 0.5 to 1 eV, allowing a continuous and prolonged emission at room temperature. Finally, the excited Cr^{3+}_{N2} formed by thermal activation leads to recombination of the charged carriers emission from the ^2E to $^4A_2$ energy levels (step 4).[62]

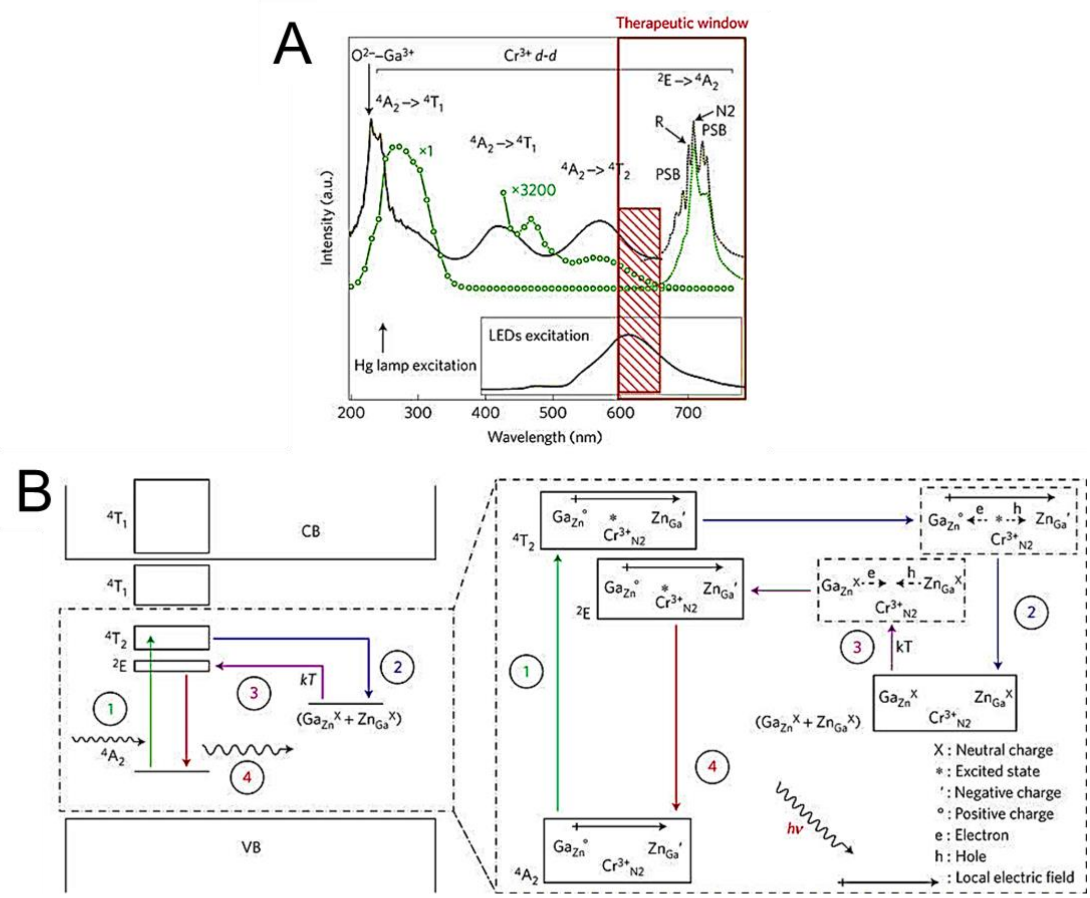

Figure 1.5: A) Optical properties of ZGO:Cr. PL excitation and emission spectra in black and TSL excitation and emission spectra in green. B) Proposed mechanism for the renewable persistent luminescence of ZGO:Cr. From reference 62.[62]

1.3.2 Plasmonic Nanoparticles: Surface Plasmon Resonance (SPR)

Silver and gold NPs have broadly been used for a wide range of biomedical applications such as anticancer research[66,67], molecular imaging[68,69] and bio-sensing[70,71] thanks to their optical properties. Moreover, the biocompatibility of GNPs has favoured its extensive use for biomedical aplications.[72]

In gold and silver nanoparticles, there is a characteristic extinction band in the vis/NIR region of the electromagnetic spectra. The origin of this is a collective oscillation of the free electrons in the conduction band of the metal triggered by incident light of the same frequency (Figure 1.6). For small nanoparticles the main component of the extinction band is due to absorbance, whilst scattering component is low. Interestingly, the frequency of resonance strongly depends on the size and shape of the nanoparticle, which enable a fine tuning of their optical properties.[73,74,75]

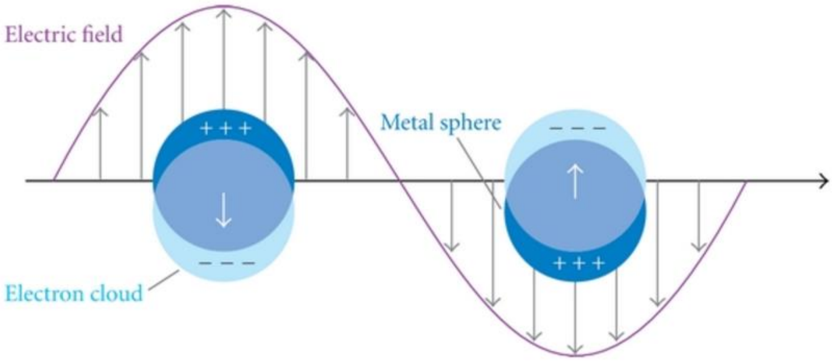

Figure 1.6: Surface Plasmon Resonance: Schematic representation of the interaction of metal NPs with the electric field of light76.[76]

1.3.2.1 Gold Nanorods as PAI Contrasts

Gold nanorods (GNRs) are a good example of tuning the position of the SPR band just mentioned before. Their singular optical properties stem from the anisotropy of these particles. Thus, two different oscillation of electrons with different energies are possible here, resulting in two extinction bands: the transverse surface plasmon resonance (TSPR) is due to the oscillation along the transverse direction, resulting in a weak absorption band around 520 nm; and the longitudinal surface plasmon resonance (LSPR) is due to oscillations along the longitudinal direction, resulting in a strong absorption band in the vis –NIR region (figure 1.7).[77] The position of this band strongly depends on the aspect ratio (length divided by width) and therefore is relatively easy to tune the position of the band to peak in a specific region of the vis-

NIR spectrum. Since light absorption triggers the photoacoustic response, contrast agents with a high molar extinction coefficient facilitate their distinction from endogenous chromophores. In this regard, GNRs are an attractive choice since the extinction coefficients are in the range of 4 – 5.5 x 10^9 $M^{-1}cm^{-1}$ for longitudinal surface plasmon between 728 and 845 nm[78], i.e. orders of magnitude higher than endogenous absorbers or other types of contrast agents (e.g. AlexaFluor750 and iRFP720 coefficients are 2.5 x 10^5 and 9.6 x 10^4 $M^{-1}cm^{-1}$, respectively).[79]

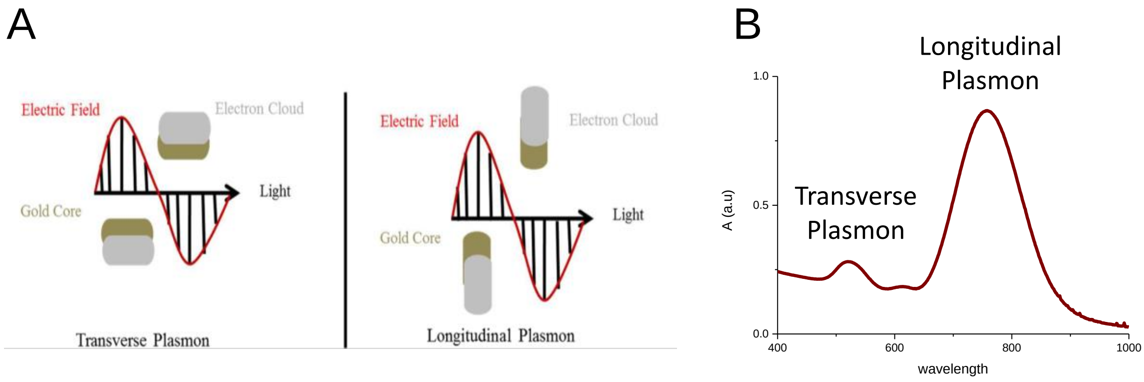

Figure 1.7: Optical properties of GNRs. A) Schematic representation of transverse and longitudinal Surface Plasmon Resonance of GNRs. From reference 77.[77]

1.4 Motivation: Stem Cell Tracking

1.4.1 Stem Cell tracking: Why?

Several regenerative medicine treatments (RMT) have entered in clinical trials for a broad range of indication: from acute myocardial infarction to type 1 diabetes mellitus (DM).[80] However, possible risks of using stem cells in medicine have been predicted [80]. The main risks include inflammation, systemic toxicity, immunogenicity, fibrosis, mal-differentiation and carcinogenesis. The main concerns are their tumorigenic potential and immunogenicity. The fear of a possible tumorigenic outcome stems from two elements: the renewal power of stem cells and their ability of differentiating to other type of cells. This might lead to the formation of teratomas or, if the cells are genetically altered teratocarcinomas. A teratocarcinoma is a teratoma with persisting undifferentiated stem cells[81]. Just like any foreign substance, stem cells administrated in an organism can trigger an immune reaction that can lead to immunotoxicity. These risks might pose a problem in the translation of RMTs into humans. Therefore, the success of this line of research will depend on the anticipation and resolution of its side effects.

Before any novel treatment or drug can become a reality, we need to assess the safety profile of the candidate. For this, it is necessary to assess the pharmacodynamics (what the drug does to the body) and pharmacokinetics (what the body does to the drug) of a determined molecule. The challenge here is the cell nature of RMT. Therefore, there is a need to develop novel quantitative real time imaging methods and appropriate probes for long-term tracking of stem cells *in vivo*.

1.4.2 Stem Cell tracking: How?

There are two main approaches to label cells: direct and indirect methods. Direct methods are based in the introduction of a contrast or labelling agent before *in vivo* transplantation. Indirect labelling involves the genetic alteration of cells and insertion of a reporter gene. Main drawback of direct methods is the dilution of the contrast agent over cell division.[82] On the other hand, the use of reporter genes could be held back in the clinic due to the inherent DNA manipulation. Frangioni and Hajjar described the characteristics of an ideal contrast agent and imaging method system.[83] First and most importantly, biocompatibility of the method need to be guaranteed. In addition, minimal transfer of contrasts to other neighbouring cells and avoiding dilution of contrast agents after cell division would help to avoid false positives and improve the long-term tracking. Limits to detection of current methods should be improved to achieve single cell detection. When contrast agents and imaging methods are intended for clinical trials, genetic modification of cells (i.e. indirect methods) should be avoided. In addition non-invasive methods that do not require additional injections are preferred for humans.[83]

Contrast agents usually used in direct labelling are organic dyes and NPs. 1,1'-Dioctadecyl-3,3,3',3'-tetramethylindotricarbocyanine iodide (DiR) is a fluorescent organic dye, provides a safety, stable and strong labelling. Embryonic stem cells were labelled with a DiR and successfully tracked *in vivo*.[84] QDs are arising as a promising alternative to organic dyes thanks to their photo-stability. Unlike traditional organic fluorochromes, QDs do not suffer from photo bleaching. The potential of QDs as stem cells trackers was shown by Lei *et al* who could track QD-labelled MSCs *in vivo*.[85] Other NPs such as GNRs have been shown not to interfere with MSC differentiation *in vivo* and a powerful potential tool in cell tracking.[86] Similarly, SPIONs have also been used track cells *in vivo* in small animals.[87,88] More interestingly, SPIONs have also been used in clinical trials.[89,90] More specifically, SPIONs labelled MSCs were injected in multiple sclerosis and amyotrophic lateral sclerosis patients successfully tracking stem cells. [89] One of the limitations of direct methods is the impossibility to track cell viability. This problem can be addressed by combining the use of direct contrasts with indirect methods.[91]

Indirect methods consist in the genetically manipulation of the studied cells to introduce a reporter gene. These reporter genes can then be translated into a receptor, enzyme or luminescent protein.[92] The reporter genes are conserved in the subsequent generation after cell division.[93] Thus, the problem of contrast dilution posed by direct methods is overcome. In addition, the presence of the reporter gene is obviously inherent to cell survival, allowing studying cell viability. Green fluorescent protein (GFP) and other fluorescent proteins derived from GFP has been extensively used for years.[94,95] However, as mentioned before problems with tissue auto fluorescence can reduce the signal-to-noise ratio of fluorescent approaches.[92] Bioluminescence is a type of chemiluminescence where the excitation is achieved through a biochemical reaction. This way, in bioluminescence imaging (BLI), an external source of excitation is avoided, improving signal-noise ratio.[96] BLI relies in the emission of photons during the oxidation of a substrate, D-luciferine, by a luciferase enzyme (extracted from firefly or renilla). Luciferase has extensively been used for tracking different stem cells such as embryonic[97], MSCs[98], and neural stem cells[99]. Reporter genes are essential tools for in vitro and preclinical imaging to understand cellular and physiological processes before any therapy can be applied, but their potential use as indirect labelling agents in the clinics is unrealistic. Therefore new strategies that enable cell tracking with exogenous biocompatible labels will be required to monitor those processes.

1.5 Bibliography

1. Payton, K. Silica-based multimodal / multifunctional nanoparticles for bioimaging and biosensing applications. **3,** 579–592 (2008).
2. Kalimuthu, S., Jeong, J. H., Oh, J. M. & Ahn, B.-C. Drug Discovery by Molecular Imaging and Monitoring Therapy Response in Lymphoma. *International Journal of Molecular Sciences* **18,** 1639 (2017).
3. Rudin, M. & Weissleder, R. Molecular imaging in drug discovery and development. *Nature Reviews Drug Discovery* **2,** 123 (2003).

4. Achilefu, S. Lighting up Tumors with Receptor-Specific Optical Molecular Probes. *Technology in Cancer Research & Treatment* **3,** 393–409 (2004).
5. Ntziachristos, V. & Razansky, D. Molecular Imaging by Means of Multispectral Optoacoustic Tomography (MSOT). *Chemical Reviews* **110,** 2783–2794 (2010).
6. Hahn, M. A., Singh, A. K., Sharma, P., Brown, S. C. & Moudgil, B. M. Nanoparticles as contrast agents for in-vivo bioimaging: current status and future perspectives. *Analytical and Bioanalytical Chemistry* **399,** 3–27 (2011).
7. Herranz, M. & Ruibal, A. Optical Imaging in Breast Cancer Diagnosis: The Next Evolution. *Journal of Oncology* **2012,** 863747 (2012).
8. Massoud, T. F., Massoud, T. F., Gambhir, S. S. & Gambhir, S. S. Molecular imaging in living subjects: seeing fundamental biological processes in a new light. *Genes & Development* **17,** 545–580 (2003).
9. Zhang, H. *et al.* Penetration depth of photons in biological tissues from hyperspectral imaging in shortwave infrared in transmission and reflection geometries. *Journal of Biomedical Optics* **21,** 126006 (2016).
10. Estelrich, J., Sánchez-Martín, M. J. & Busquets, M. A. Nanoparticles in magnetic resonance imaging: From simple to dual contrast agents. *International Journal of Nanomedicine* **10,** 1727–1741 (2015).
11. Lam, T., Pouliot, P., Avti, P. K., Lesage, F. & Kakkar, A. K. Superparamagnetic iron oxide based nanoprobes for imaging and theranostics. *Advances in Colloid and Interface Science* **199–200,** 95–113 (2013).
12. Hahn, M. A., Singh, A. K., Sharma, P., Brown, S. C. & Moudgil, B. M. Nanoparticles as contrast agents for in-vivo bioimaging: current status and future perspectives. *Analytical and Bioanalytical Chemistry* **399,** 3–27 (2011).
13. Caravan, P., Ellison, J. J., McMurry, T. J. & Lauffer, R. B. Gadolinium(III) Chelates as MRI Contrast Agents: Structure, Dynamics, and Applications. *Chemical Reviews* **99,** 2293–2352 (1999).
14. Senpan, A. *et al.* Conquering the Dark Side: Colloidal Iron Oxide

Nanoparticles. *ACS Nano* **3,** 3917–3926 (2009).

15. Becker, N., Liebermann, D., Wesch, H. & Van Kaick, G. Mortality among Thorotrast-exposed patients and an unexposed comparison group in the German Thorotrast study. *European journal of cancer (Oxford, England : 1990)* **44,** 1259—1268 (2008).

16. Townsend, D. W. Combined Positron Emission Tomography–Computed Tomography: The Historical Perspective. *Seminars in Ultrasound, CT and MRI* **29,** 232–235 (2008).

17. Debbage, P. & Jaschke, W. Molecular imaging with nanoparticles: giant roles for dwarf actors. *Histochemistry and Cell Biology* **130,** 845–875 (2008).

18. Debbage, P. & Jaschke, W. Molecular imaging with nanoparticles: giant roles for dwarf actors. *Histochemistry and Cell Biology* **130,** 845–875 (2008).

19. Wang, S., Lin, J., Wang, T., Chen, X. & Huang, P. Recent Advances in Photoacoustic Imaging for Deep-Tissue Biomedical Applications. *Theranostics* **6,** 2394–2413 (2016).

20. Mérian, J., Gravier, J., Navarro, F. & Texier, I. *Fluorescent Nanoprobes Dedicated to in Vivo Imaging: From Preclinical Validations to Clinical Translation*. *Molecules (Basel, Switzerland)* **17,** (2012).

21. Weissleder, R. A clearer vision for in vivo imaging. *Nat Biotech* **19,** 316–317 (2001).

22. Braslavsky, S. E. Glossary of terms used in photochemistry, 3rd edition (IUPAC Recommendations 2006). *Pure and Applied Chemistry* **79,** 293–465 (2007).

23. Valeur, B. & Berberan-Santos, M. N. A Brief History of Fluorescence and Phosphorescence before the Emergence of Quantum Theory. *Journal of Chemical Education* **88,** 731–738 (2011).

24. Valeur, B. & Berberan-Santos, M. N. A Brief History of Fluorescence and Phosphorescence before the Emergence of Quantum Theory. *Journal of Chemical Education* **88,** 731–738 (2011).

25. Li, Y., Gecevicius, M. & Qiu, J. Long persistent phosphors—from fundamentals to applications. *Chem. Soc. Rev.* (2016). doi:10.1039/C5CS00582E

26. Viana, B. *Persistent Luminescence of ZnGa2O4:Cr3+ Transparent Glass Ceramics: Effects of Excitation Wavelength and Excitation Power*. *European Journal of Inorganic Chemistry* **2017,** (2017).

27. Jain, A., Kumar, A., Dhoble, S. J. & Peshwe, D. R. Persistent luminescence: An insight. *Renewable and Sustainable Energy Reviews* **65,** 135–153 (2016).

28. Taruttis, A., Herzog, E., Razansky, D. & Ntziachristos, V. Real-time imaging of cardiovascular dynamics and circulating gold nanorods with multispectral optoacoustic tomography. *Opt. Express* **18,** 19592–19602 (2010).

29. Taruttis, A., Morscher, S., Burton, N. C., Razansky, D. & Ntziachristos, V. Fast multispectral optoacoustic tomography (MSOT) for dynamic imaging of pharmacokinetics and biodistribution in multiple organs. *PloS one* **7,** e30491 (2012).

30. Ermilov, S. A. *et al.* Laser optoacoustic imaging system for detection of breast cancer. **14,** 24007–24014 (2009).

31. Wang, L. V & Hu, S. Photoacoustic Tomography: In Vivo Imaging from Organelles to Organs. *Science (New York, N.y.)* **335,** 1458–1462 (2012).

32. Esenaliev, R. O., Karabutov, A. A. & Oraevsky, A. A. Sensitivity of laser opto-acoustic imaging in detection of small deeply embedded tumors. *IEEE Journal of Selected Topics in Quantum Electronics* **5,** 981–988 (1999).

33. G M Kolkman, R., Steenbergen, W. & van Leeuwen, T. *In vivo photoacoustic imaging of blood vessels with a pulsed laser diode*. *Lasers in medical science* **21,** (2006).

34. Ermilov, S. A. *et al.* Laser optoacoustic imaging system for detection of breast cancer. **14,** 24007–24014 (2009).

35. Bell, A. G. THE PRODUCTION OF SOUND BY RADIANT ENERGY. *Science* **os-2,** 242–253 (1881).

36. Emelianov, S. Y., Li, P.-C. & O'Donnell, M. Photoacoustics for molecular imaging and therapy. *Physics today* **62,** 34–39 (2009).

37. Voura, E. B., Jaiswal, J. K., Mattoussi, H. & Simon, S. M. Tracking metastatic tumor cell extravasation with quantum dot nanocrystals and fluorescence emission-scanning microscopy. *Nature Medicine* **10,** 993 (2004).

38. Thakor, A. S. *et al.* Clinically Approved Nanoparticle Imaging Agents. *Journal of Nuclear Medicine* **57,** 1833–1837 (2016).

39. Banerjee, S., Ambikalmajan Pillai, M. R. & Ramamoorthy, N. Evolution of Tc-99m in diagnostic radiopharmaceuticals. *Seminars in Nuclear Medicine* **31,** 260–277 (2001).

40. Newman, E. A. & Newman, L. A. Lymphatic Mapping Techniques and Sentinel Lymph Node Biopsy in Breast Cancer. *Surgical Clinics of North America* **87,** 353–364 (2007).

41. Dengel, L. T. *et al.* Intraoperative Imaging Guidance for Sentinel Node Biopsy in Melanoma Using a Mobile Gamma Camera. *Annals of surgery* **253,** 774–778 (2011).

42. Elgazzar, A. H., Yeung, H. W. & Webner, P. J. Indium-111-Leukocyte and Technetium-99m-Sulfur Colloid Uptake in Paget's Disease. *Journal of Nuclear Medicine* **37,** 858–861 (1996).

43. Semelka, R. C. & Helmberger, T. K. G. Contrast Agents for MR Imaging of the Liver. *Radiology* **218,** 27–38 (2001).

44. Corot, C., Robert, P., Idée, J. M. & Port, M. Recent advances in iron oxide nanocrystal technology for medical imaging. *Advanced Drug Delivery Reviews* **58,** 1471–1504 (2006).

45. Thakor, A. S. *et al.* Clinically Approved Nanoparticle Imaging Agents. *Journal of Nuclear Medicine* **57,** 1833–1837 (2016).

46. Elrod, D. B., Partha, R., Danila, D., Casscells, S. W. & Conyers, J. L. An iodinated liposomal computed tomographic contrast agent prepared from a diiodophosphatidylcholine lipid. *Nanomedicine: Nanotechnology, Biology and*

Medicine **5,** 42–45 (2009).

47. Skajaa, T. *et al.* High density lipoprotein-based contrast agents for multimodal imaging of atherosclerosis. *Arteriosclerosis, thrombosis, and vascular biology* **30,** 169–176 (2010).

48. McIntire, G. L. *et al.* Pulmonary Delivery of Nanoparticles of Insoluble, Iodinated CT x-ray coNtrast Agents to Lung Draining Lymph Nodes in Dogs. *Journal of Pharmaceutical Sciences* **87,** 1466–1470 (1998).

49. Lu, Y.-C., Yang, C.-X. & Yan, X.-P. Radiopaque tantalum oxide coated persistent luminescent nanoparticles as multimodal probes for in vivo near-infrared luminescence and computed tomography bioimaging. *Nanoscale* **7,** 17929–17937 (2015).

50. Kim, D., Park, S., Lee, J. H., Jeong, Y. Y. & Jon, S. Antibiofouling Polymer-Coated Gold Nanoparticles as a Contrast Agent for in Vivo X-ray Computed Tomography Imaging. *Journal of the American Chemical Society* **129,** 7661–7665 (2007).

51. Aydogan, B. *et al.* AuNP-DG: Deoxyglucose-Labeled Gold Nanoparticles as X-ray Computed Tomography Contrast Agents for Cancer Imaging. *Molecular Imaging and Biology* **12,** 463–467 (2010).

52. Jackson, P. A., Rahman, W. N. W. A., Wong, C. J., Ackerly, T. & Geso, M. Potential dependent superiority of gold nanoparticles in comparison to iodinated contrast agents. *European Journal of Radiology* **75,** 104–109 (2010).

53. Gu, Z. *et al.* Red, green, and blue luminescence from ZnGa2O4 nanowire arrays. *Journal of Physical Chemistry Letters* **1,** 354–357 (2010).

54. Bessière, A. *et al.* Storage of visible light for long-lasting phosphorescence in chromium-doped zinc gallate. *Chemistry of Materials* **26,** 1365–1373 (2014).

55. Van den Eeckhout, K., Smet, P. F. & Poelman, D. Persistent Luminescence in Eu(2+)-Doped Compounds: A Review. *Materials* **3,** 2536–2566 (2010).

56. Yamaga, M., Ohsumi, Y., Nakayama, T. & Han, T. P. J. Persistent phosphorescence in Ce-doped Lu2SiO5. *Optical Materials Express* **2,** 413–

419 (2012).

57. Som, S., Choubey, A. & Sharma, S. K. Spectral and trapping parameters of Eu3+ in Gd2O2S nanophosphor. *Journal of Experimental Nanoscience* **10,** 350–370 (2015).

58. Wang, B. *et al.* Design, Preparation, and Characterization of a Novel Red Long-Persistent Perovskite Phosphor: Ca3Ti2O7:Pr3+. *Inorganic Chemistry* **54,** 11299–11306 (2015).

59. le Masne de Chermont, Q. *et al.* Nanoprobes with near-infrared persistent luminescence for in vivo imaging. *Proceedings of the National Academy of Sciences of the United States of America* **104,** 9266–9271 (2007).

60. Liu, F. *et al.* Photostimulated near-infrared persistent luminescence as a new optical read-out from Cr^{3+}-doped $LiGa_5O_8$. *Scientific reports* **3,** 1554 (2013).

61. Fu, X. *et al.* Long persistent near infrared luminescence nanoprobes LiGa 5 O 8 : Cr 3 + -PEG-OCH 3 for in vivo imaging. *Optical Materials* **36,** 1792–1797 (2014).

62. Maldiney, T. *et al.* The in vivo activation of persistent nanophosphors for optical imaging of vascularization, tumours and grafted cells. *Nature Materials* **13,** 418–426 (2014).

63. Allix, M. *et al.* Considerable improvement of long-persistent luminescence in germanium and tin substituted ZnGa2O4. *Chemistry of Materials* **25,** 1600–1606 (2013).

64. Bessière, A. *et al.* ZnGa 2 O 4 : Cr 3 + : a new red long-lasting phosphor with high brightness. **19,** 10131–10137 (2011).

65. Viana, B. *et al.* Storage of Visible Light for Long-Lasting Phosphorescence in Chromium-Doped Zinc Gallate. (2014). doi:10.1021/cm403050q

66. Dreaden, E. C., Mackey, M. A., Huang, X., Kang, B. & El-Sayed, M. A. Beating cancer in multiple ways using nanogold. *Chem. Soc. Rev.* **40,** 3391–3404 (2011).

67. Wang, S. *et al.* Photothermal Effects of Supramolecularly Assembled Gold Nanoparticles for the Targeted Treatment of Cancer Cells. *Angewandte Chemie International Edition* **49,** 3777–3781 (2010).

68. Sokolov, K. *et al.* Advances in Brief Real-Time Vital Optical Imaging of Precancer Using Anti-Epidermal Growth Factor Receptor Antibodies Conjugated to Gold Nanoparticles 1. 1999–2004 (2004).

69. El-Sayed, I. H., Huang, X. & El-Sayed, M. A. Surface Plasmon Resonance Scattering and Absorption of anti-EGFR Antibody Conjugated Gold Nanoparticles in Cancer Diagnostics: Applications in Oral Cancer. *Nano Letters* **5,** 829–834 (2005).

70. Qian, X. *et al.* In vivo tumor targeting and spectroscopic detection with surface-enhanced Raman nanoparticle tags. *Nat Biotech* **26,** 83–90 (2008).

71. Grubisha, D. S., Lipert, R. J., Park, H.-Y., Driskell, J. & Porter, M. D. Femtomolar Detection of Prostate-Specific Antigen: An Immunoassay Based on Surface-Enhanced Raman Scattering and Immunogold Labels. *Analytical Chemistry* **75,** 5936–5943 (2003).

72. Das, M., Shim, K. H., An, S. S. a. & Yi, D. K. Review on gold nanoparticles and their applications. *Toxicology and Environmental Health Sciences* **3,** 193–205 (2012).

73. Kelly, K. L., Coronado, E., Zhao, L. L. & Schatz, G. C. The Optical Properties of Metal Nanoparticles: The Influence of Size, Shape, and Dielectric Environment. *The Journal of Physical Chemistry B* **107,** 668–677 (2003).

74. Liz-Marzán, L. M. Tailoring Surface Plasmons through the Morphology and Assembly of Metal Nanoparticles. *Langmuir* **22,** 32–41 (2006).

75. Link, S. & El-Sayed, M. A. Size and Temperature Dependence of the Plasmon Absorption of Colloidal Gold Nanoparticles. *The Journal of Physical Chemistry B* **103,** 4212 (1999).

76. Willets, K. A. & Van Duyne, R. P. Localized Surface Plasmon Resonance Spectroscopy and Sensing. *Annual Review of Physical Chemistry* **58,** 267–297

(2007).

77. Lohse, S. E. & Murphy, C. J. The Quest for Shape Control: A History of Gold Nanorod Synthesis. *Chemistry of Materials* **25,** 1250–1261 (2013).

78. Orendorff, C. J. & Murphy, C. J. Gold Nanorod Quantitation of metal content in the silver-assisted growth of gold nanorods. *The journal of physical chemistry. B* **110,** 3990–4 (2006).

79. Shcherbakova, D. M. & Verkhusha, V. V. Near-infrared fluorescent proteins for multicolor in vivo imaging. *Nature Methods* **10,** 751 (2013).

80. Goldring, C. E. P. *et al.* Assessing the safety of stem cell therapeutics. *Cell stem cell* **8,** 618–28 (2011).

81. Ben-David, U. & Benvenisty, N. The tumorigenicity of human embryonic and induced pluripotent stem cells. *Nat Rev Cancer* **11,** 268–277 (2011).

82. von der Haar, K., Lavrentieva, A., Stahl, F., Scheper, T. & Blume, C. Lost signature: progress and failures in in vivo tracking of implanted stem cells. *Applied Microbiology and Biotechnology* **99,** 9907–9922 (2015).

83. Frangioni, J. V & Hajjar, R. J. In vivo tracking of stem cells for clinical trials in cardiovascular disease. *Circulation* **110,** 3378–83 (2004).

84. Ruan, J. *et al.* Dir-labeled embryonic stem cells for targeted imaging of in vivo gastric cancer cells. *Theranostics* **2,** 618–628 (2012).

85. Lei, Y. *et al.* Applications of Mesenchymal Stem Cells Labeled with Tat Peptide Conjugated Quantum Dots to Cell Tracking in Mouse Body. *Bioconjugate Chemistry* **19,** 421–427 (2008).

86. Comenge, J. *et al.* Preventing Plasmon Coupling between Gold Nanorods Improves the Sensitivity of Photoacoustic Detection of Labeled Stem Cells in Vivo. *ACS Nano* **10,** 7106–7116 (2016).

87. Bulte, J. W. M. *et al.* Magnetodendrimers allow endosomal magnetic labeling and in vivo tracking of stem cells. *Nature Biotechnology* **19,** 1141 (2001).

88. Dunning, M. D. *et al.* Superparamagnetic Iron Oxide-Labeled Schwann Cells

and Olfactory Ensheathing Cells Can Be Traced In Vivo by Magnetic Resonance Imaging and Retain Functional Properties after Transplantation into the CNS. *The Journal of Neuroscience* **24,** 9799 LP-9810 (2004).

89. Karussis, D. *et al.* Safety and Immunological Effects of Mesenchymal Stem Cell Transplantation in Patients With Multiple Sclerosis and Amyotrophic Lateral Sclerosis. *Archives of neurology* **67,** 1187–1194 (2010).

90. Richards, J. M. J. *et al.* In Vivo Mononuclear Cell Tracking Using Superparamagnetic Particles of Iron Oxide / Clinical Perspective. *Circulation: Cardiovascular Imaging* **5,** 509–517 (2012).

91. A., G. A., T., W. P., M., van Z. P. C. & M., B. J. W. Developing MR reporter genes: promises and pitfalls. *NMR in Biomedicine* **20,** 275–290 (2007).

92. Srivastava, A. K. & Bulte, J. W. M. Seeing Stem Cells at Work In Vivo. *Stem Cell Reviews and Reports* **10,** 127–144 (2014).

93. Akins, E. J. & Dubey, P. Noninvasive Imaging of Cell-Mediated Therapy for Treatment of Cancer. *Journal of nuclear medicine : official publication, Society of Nuclear Medicine* **49,** 180S–195S (2008).

94. Kremers, G.-J., Gilbert, S. G., Cranfill, P. J., Davidson, M. W. & Piston, D. W. Fluorescent proteins at a glance. *Journal of Cell Science* **124,** 157 LP-160 (2011).

95. Shaner, N. C. *et al.* Improved monomeric red, orange and yellow fluorescent proteins derived from Discosoma sp. red fluorescent protein. *Nature Biotechnology* **22,** 1567 (2004).

96. Sadikot, R. T. & Blackwell, T. S. Bioluminescence Imaging. *Proceedings of the American Thoracic Society* **2,** 537–540 (2005).

97. Priddle, H. *et al.* Bioluminescence Imaging of Human Embryonic Stem Cells Transplanted In Vivo in Murine and Chick Models. *Cloning and Stem Cells* **11,** 259–267 (2009).

98. Love, Z. *et al.* Imaging of mesenchymal stem cell transplant by

bioluminescence and PET. *Journal of nuclear medicine : official publication, Society of Nuclear Medicine* **48,** 2011–20 (2007).

99. Tang, Y. *et al.* In Vivo Tracking of Neural Progenitor Cell Migration to Glioblastomas. *Human Gene Therapy* **14,** 1247–1254 (2003).

CHAPTER 2

Synthesis and Surface Modification of Gold Nanorods

2.1 Introduction

Due to their biocompatibility, versatility of surface functionalization and especially their interesting optical properties gold nanoparticles (GNPs) have arisen as promising tools for biotechnology and biomedicine.[1] Their physico-chemical properties, and more specifically their optical properties, greatly depend on size and shape.[2,3] For this reason, great efforts have been made to control size and anisotropic growth of nanoparticles. Consequently, many preparative routes have been described for a variety of shapes such as spheres, stars, triangles, nanoboxes and nanorods.[4] This has ultimately opened the way for a host of new applications such as bioimaging or phothermal therapy.[5,6] In the case of GNRs, there is a direct relation between optical properties and their aspect ratio (AR).[7] The AR can be tuned by varying the conditions of the synthesis, and it is possible to control the position of the longitudinal plasmon band (LSPR) across a wide range, well into the NIR.[8] In this manner, LSPR can be adjusted to overlap perfectly with the optical window[9] of many biological samples (See chapter 1).

Cetyltrimethylammonium bromide (CTAB) is a cationic surfactant normally used in the preparation of GNRs due to its ability to behave as shape and size controller. However, CTAB is cytotoxic at concentrations much lower than the used in the synthesis of GNRs, (IC_{50}<1µM).[10] This cytotoxicity poses a problem in the use of GNRs for biomedical applications. Therefore, their surface needs to be modified before GNRs can be used as candidates for biomedical research. Different chemical strategies can be used for the modification of GNRs which can lead to improvement of biocompatibility and colloidal stability. For instance, polymer coating has been broadly used for this purposes.[11] A good example of this is the multilayer formation of the electrostatic polymers PAA and PAH developed by Murphy, Wyatt and co-workers.[12] Silica coating is another widely used approach in the surface modification of NPs. Effective protocols to control the thickness of the silica shell on the surface of GNRs can be found in the literature.[13] In addition, ligand exchange is often based on the replacement of CTAB by other molecules that have a greater affinity for the gold surface. While a wide range of chemical groups have been used for ligand exchange including phosphates, amines or carboxylic acids, thiols remain by far the most broadly exploited functionality. This is due to their high binding energy leading to a remarkable stable chemical bond.[14,15] Therefore more stable systems are achieved, even under testing conditions such as physiological medium. This high affinity is the base for the fabrication of robust self-assembled monolayers (SAMs) of different organic molecules.[16] Following this approach, molecules such as 11-mercaptoundecanoic acid (MUA)[17] or polyethylene glycol (PEG)[18] have been bound to GNRs. Relevant biomolecules such as DNA[19], lipids[20], peptides[21] and proteins[22] have also been conjugated to GNRs. The construction of hybrids from GNPs and biomolecules can lead to new tools for diagnostics and drug delivery.[23]

2.2 Methods

Reagents

The following chemicals were purchased from Sigma-Aldrich and used as received. $HAuCl_4 \cdot 3H_2O$ (>99.0%), $NaBH_4$ (>99.99%), $AgNO_3$(99.0%), hexadecyltrimethylammonium bromide (CTAB, >99%), O-[2-(3-mercaptopropionylamino)ethyl]-O′-methylpolyethylene glycol (mPEG-SH, MW = 5000 Da) *N*-Hydroxysuccinimide (NHS, 98%), *N*-(3-Dimethylaminopropyl)-*N*′-ethylcarbodiimide hydrochloride (EDAC, >98%) and Bovine serum albumin (BSA,). Monocarboxy(1-mercaptoundec-11- yl)hexaethylene glycol (PEG-COOH, MW= 526.73 Da) was obtained from Prochimia and TAT peptide (97%) from Life Tein.

GNRs Preparation

The preparation of GNRs was adapted from El-Sayed *et al* [24] and is based on a seeding growth approach. Briefly, seeds were made by adding 5 mL of an aqueous 0.5 mM $HAuCl_4$ solution to 5 mL of a 0.1 M CTAB solution under gentle agitation (make sure the CTAB remains fully dissolved at all times, if needed by careful heating). Then, 500 µL of an ice-cold 0.01 M $NaBH_4$ solution was added under vigorous stirring. The mixture was then stirred gently for 2 hours. To prepare the growth solutions, different volumes of $AgNO_3$ (4 mM) ranging from 0.1 to 0.2 mL, depending on the desired aspect ratio, were added to 5 mL of CTAB (0.2M). For a typical synthesis, volume of $AgNO_3$ was set to 0.2mL (sample f in figure 2.1). Then, 5 mL of $HAuCl_4$ (1 mM) was added followed by addition of 80 µL of ascorbic acid (0.1 M). Finally, 20 µL of the seed solution were added under vigorous stirring and left in a water bath at 28 °C overnight. The method was also scaled up to 100 mL.

Surface Modification:

PEG 5000 g/mol: 100 mL GNRs were purified by centrifugation at 15000 g for 20 minutes; the supernatant was removed and the pellet was resuspended in mQ water. A second centrifugation step was carried out and the pellet was resuspended in 100 mL solution of 0.1 mM PEG (≈10^5 PEG molecules per GNR) in mQ water. The mixture was left stirring overnight. A second ligand exchange was done in the same conditions, and left stirring for 2 hours. The particles were further purified by 2 subsequent centrifugation steps.

PEG-COOH: PEG-COOH (MW = 526.7 Da) were used. 100 mL of GNRs were purified as explained above and added dropwise in a solution of 100 mL PEG-COOH (0.1 mM) in acetic acid (10 mM). The solution was kept under vigorous stirring overnight to cause reversible GNR coagulation. Then, supernatant was removed, and GNRs were resuspended in a solution of PEG-COOH (0.1 mM) in NaOH (10 mM) and kept under vigorous stirring overnight. Finally, the functionalized GNRs were purified by centrifugation three times and resuspended in HEPES buffer (10 mM, pH 7.4) for storage.

BSA conjugation: For the activation of carboxylic acid, 12 mg of EDAC and 24 mg of NHS were dissolved in 2 mL of MES buffer (0.5 M MES, free acid, pH 6.3). Different volumes of the previous mixture (0, 2, 4, 6, 8, 10, 14 and 6 µL) were added to 1 mL of GNRs solution in MES buffer (0.1M, pH 6.3) at atomic Au concentration (as measured by the absorbance at 400 nm) of 0.6 mM. The suspensions were incubated under continuous mixing for 1 hour at room temperature, followed by a subsequent centrifugation. 100 µL of BSA solution in PBS (0.05 mM) was added to 1 mL of activated GNRs. The suspension was again incubated under vigorous mixing for 3 hours at room temperature. Finally, samples were purified by a centrifugation step.

Peptide conjugation: Activation of carboxylic acids was performed as explained above. 20 µL of TAT peptide (5 mM) were incubated with 1 mL of activated GNRs for 3 hours at room temperature followed by a subsequent purification step.

Characterisation of GNRs

Vis-NIR spectroscopy was conducted in a Thermo scientific Genesys 10S UV-VIS. A Malvern Zetasizer nanoZS was used for dynamic light scattering and zeta potential measurements. For DLS, 3 measurements were carried out for 20 runs each measurement per sample, at 25°C. For zeta potential: in 20µM NaCl solution. Three measurements per sample were done in clear disposable zeta cell for 20 runs each measurement, at 25°C (by Hückel). FT-IR measurements were conducted in a Bruker Lumus. 10 µL of previously purified samples were drop cast into a CaF_2 window and left to dry overnight. Measurements were taken in transmission mode (1000 scans at resolution of 4 cm^{-1}). Samples were imaged using a Tecnai G3 spirit TEM at 120 keV. 10 µL were deposited on a 3.05 mm copper grid (purchased from TAAB).

2.3 Synthesis of GNRs and tuning of optical properties

GNRs synthesis protocol is based on the seed-mediated growth method developed by El-Sayed and co-workers. [24] This method is a two steps process where nucleation and growth steps are separated. The conditions required for a homogenous nucleation are different than the ones required for an effective anisotropic growth of NPs.[25] Reductants selection is crucial for the synthesis since the oxidation state of gold in each step has a big impact. Nucleation step is based on a strong reduction of Au (III) to Au (0) by sodium borohydride ($NaBH_4$) resulting in small NPs termed “seeds”. The diameter of these seeds is around 4 nm. As a consequence, they do not exhibit the characteristic plasmon band around 520 nm of NPs > 10 nm. Since avoiding a second nucleation in the next step is essential, a weak reducer is used in the growth step. Ascorbic acid reduces Au (III) to Au (I) and only when the seeds are added, gold salt is completely reduced. Therefore, the role of seeds in the growth solution is similar to a catalyst agent. Surfactants also play an important role in the synthesis. CTAB is a quaternary ammonium cationic surfactant made of a polar head (a tertiary amine), and a non-polar tail and its use is critical in the synthesis of GNRs. It acts as a shape control and stabilizing agent. The shape control is achieved through a soft template or micelle formation. [7] CTAB molecules are absorbed in the gold forming a bilayer with the positive trimethylammonium groups facing the gold and the solvent. A mixture of surfactants made of CTAB and benzyldimethylhexadecylammoniumchloride (BDAC) can also been used in the seed-mediated growth synthesis leading to bigger ARs[24].

As mentioned before, the aspect ratio of the GNRs can be easily tuned from the synthesis. There are different parameters that can be changed such as volume of seeds added to the growth solution, volume of silver nitrate or final gold concentration. Here, the synthesis protocol has been adapted by systematically increasing the concentrations of $AgNO_3$ in the growth solution. Figure 2.1 shows the tuning of GNRs with different aspect ratios and their respective optical properties as final concentration of $AgNO_3$ is increased (Figure 2.1B). There is a direct relation between A.R and optical properties, longitudinal Plasmon resonance is shifted to the infrared region as aspect ratio of GNRs is increased, in agreement with the literature.

[26] When we push the $AgNO_3$ condition, a decrease of the AR is observed as previously reported in the literature. There is a critical concentration of $AgNO_3$ that when exceeded, the aspect ratio stops increasing and even starts decreasing.[24]

Although the mechanism has not yet been completely elucidated, two theories have been described to explain the role of silver ions. One of them involves the formation of complex with the polar heads of CTAB decreasing the charge density and therefore the repulsion. This has an impact on the size of template that leads to the growth of GNRs formed by the CTAB [24]. The second one is based on the decrease of Gold adsorption due to the presence of silver ions in the template[7].

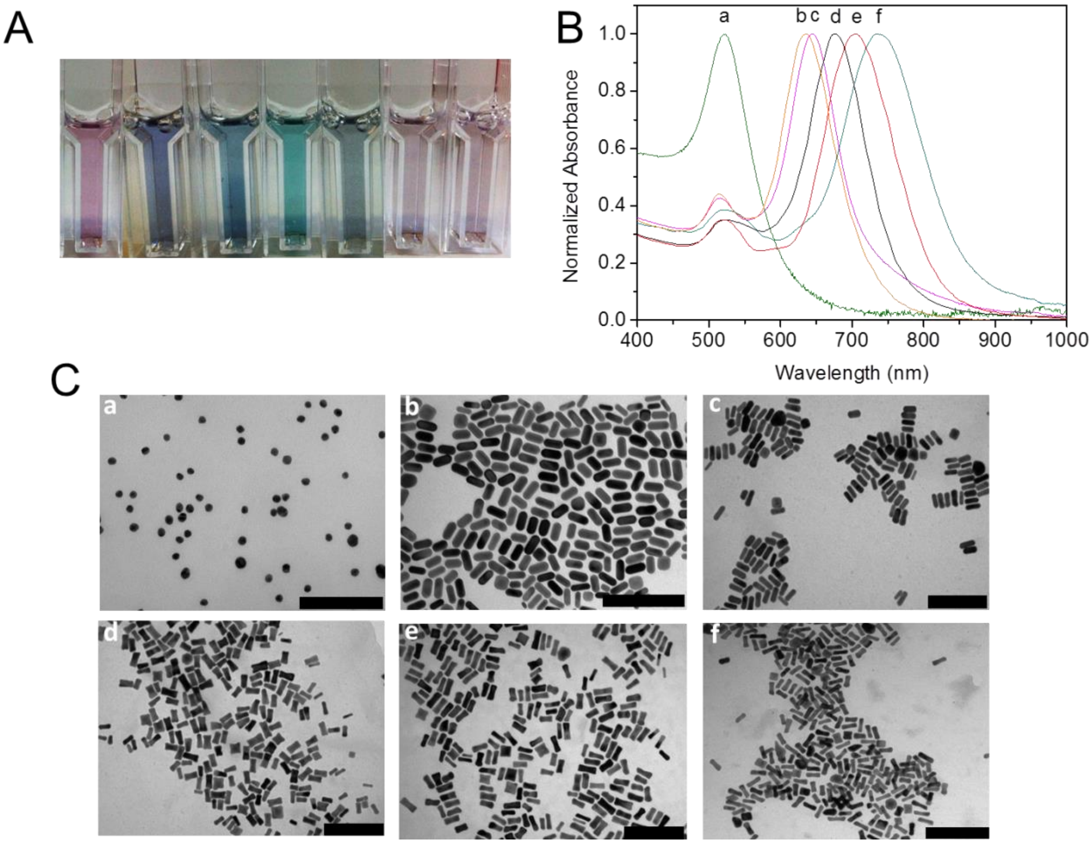

Figure 2.1: Gold Nanorods synthesis using the seed-mediated growth method. A) Pictures of different synthesis of GNRs in solution. B) Absorbance spectra of GNP and GNRs showing Longitudinal Surface Plasmon Resonance shift as concentration of AgNO3 is increased. C) TEM pictures of GNPs and GNR shown in B (scales = 200 nm). AR sample a=1, AR sample b=2.3, AR sample c=2.4, AR sampled d=2.7, AR sample e=2.9, AR sample f= 3.2

The final application of GNRs in this report is the *in vivo* photoacoustic imaging of GNRs. Therefore, the position in of the LSPR needs to be situated within the optical window. More specifically, between 700 and 800 nm or AR between 3 and 4 (sample f) where MSOT is more efficient to resolve between endogenous signal and signal coming from the probes.[6,27] Conditions used in synthesis f were selected as the most suitable for our purposes due to this reason.

More recently new protocols based on the pre-reduction of gold by aromatic compounds, such as 5-bromosalycilic acid, have been described.[28,29] These modifications led to highly monodisperse GNRs, and better control of the tuning of their optical properties. GNRs with a LSPR up to 1200 nm can be prepared. We did not have the chance to test these new protocols. However, it should be noted that the volume of our GNRs is higher than the ones with similar absorbance peak obtained by the new protocol, and therefore absorbance per GNR is higher. Note also that as reported by Scarabelli et al. GNRs synthesised with the salicylic acid approach could be grown in further steps to increase their volume, which resulted also in an increased absorbance per GNR.[30]

2.4 Surface modification of GNRs for biological applications

A good strategy to obtain particles for biological applications, and more specifically for cell labeling, not only needs to ensure biocompatibility but also colloidal stability under physiological conditions. Uptake should be straightforward with minimal interference with cellular function. For example, when working with stem cells it is important that the NPs do not interfere with cell fate or cell differentiation.

As mentioned before, CTAB was used in the preparation of GNRs due to its ability to behave as shape and size controller. However, it needs to be replaced due to issues related to cytotoxicity. Cytotoxicity of CTAB was tested in MSCs; the results are discussed in chapter 4. CTAB acts as a stabilizing agent and excess of CTAB needs to be present in the solution to ensure colloidal stability. The latter can pose a challenge in the ligand exchange process due to the affinity of CTAB molecules to gold surface, which can interfere with the reactivity of the desired ligand. In order to overcome this problem and achieve a higher ligand packing density, we propose a two-step ligand exchange process. This allows maximising CTAB excess removal while maintaining colloidal stability.

GNRs surface modification with two different ligands via ligand exchange will be discussed in this section; Poly(ethylene glycol) methyl ether thiol (5000 Da), referred as SH-PEG 5000 in this document, and Monocarboxy(1-mercaptoundec-11-yl) hexaethylene glycol (526.73 Da) or SH-PEG-COOH. Both of them are thiol-modified Polyethylene Glycol (PEG) derivatives. From a composition point of view, both ligands are very similar. However, colloidal stability is provided by different mechanisms. SH-PEG 5000 is bulky enough to stabilize the particles by a steric effect while SH-PEG-COOH is smaller and particles are only stable when the carboxylic acid is deprotonated creating an electrostatic repulsion. Both molecules bind to the particle through gold-sulphur binding. As discussed in section 2.1, the use of thiols has been the most successful strategy for ligand exchange until now due to its great affinity toward gold. In addition, PEG is a molecule vastly used in the biomedical field due to its safety and biocompatibility.[18] PEGylated GNRs have also been broadly used in biological applications and it has previously been shown that their toxicological profile is lower than CTAB coated and polystyrene sulfonate (PSS) coated GNRs.[31]

2.4.1 Functionalisation of GNRs with SH-PEG 5000

Figure 2.2 B shows UV-vis spectra of GNRs before and after surface functionalisation, a small red shift inherent to the PEGylation process was observed. Dynamic light scattering (DLS) and zeta potential were used as additional characterisation of the process (Figure 2.2 C and D). Obtaining two peaks in the DLS is a very distinctive feature of GNRs because it is a sign of anisotropy. This effect is caused by two components of Brownian motion due to the anisotropy of GNRs: translational (corresponding to the smaller hydrodynamic diameter peak) and rotational relaxation rate (corresponding to the bigger hydrodynamic diameter peak)[32,33]. However, none of them fits with the actual size. Therefore, DLS is not a good technique to determine GNRs size but a shift of the peak can indicate increase of size, hence GNRs modification. A shift was observed in both peaks when PEG-GNRs are compared with CTAB-GNRs suggesting that conjugations were successful.

As synthesized GNRs have a positive zeta potential due to the orientation of the trimethylammonium head groups in the CTAB bilayer of GNRs. On the other hand, functionalisation with SH-PEG 5000 resulted in a neutral zeta potential. This decrease in surface charge is indicative that CTAB was successfully replaced by PEG molecules.

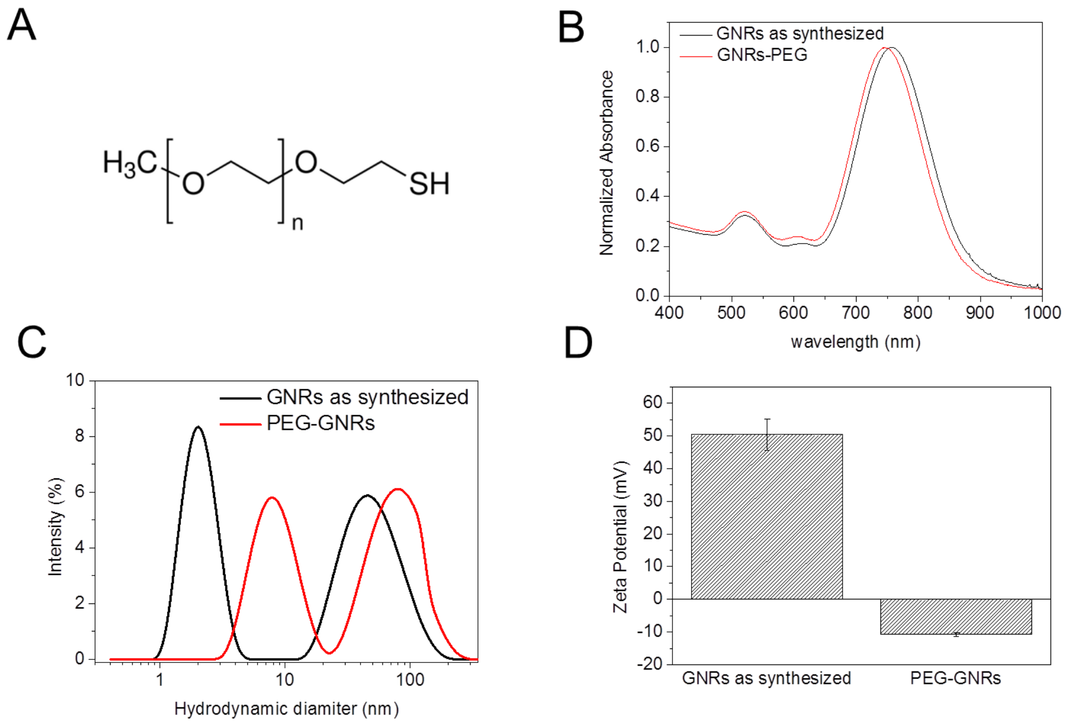

Figure 2.2: Ligand exchange with SH-PEG 5000. A) General chemical formula of SH-PEG 5000 (n≈110) B) UV-vis-NIR spectra of as synthesized and SHPEG 5000-GNRs C) Hydrodynamic diameter measured by DLS of as synthesized and SHPEG 5000-GNRs D) zeta potential measured before and after surface modification.

2.4.2 Functionalization of GNRs with SH-PEG-COOH

Functionalisation with SH-PEG-COOH poses a very different scenario. In contrast to SH-PEG 5000, this ligand is not bulky enough to stabilize GNRs through a sterically effect. Chemical structure of this molecule is shown in figure 2.3 A, SH-PEG-COOH has also been modified with a thiol group, responsible for the binding to gold surface. Thiol group is followed by an 11 carbons alkane chain used as spacer. The use of these kind of spacers have been found to lead to higher ligand density nanoparticles improving the reproducibility of ligand exchange and the colloidal stability when compared to pure PEG molecules [34]. This is especially useful for the PEGylation of GNRs since the presence of free and bound CTAB can challenge the ligand exchange. Carboxylic acid terminus is the key here for colloidal stability.

When the carboxylic acid is deprotonated, the repulsion forces of the negative charges of neighbouring GNRs are strong enough to stabilize the colloid. Although the pka of this carboxylic acid in solution is~ 3.50, SH-PEG-COOH conjugated GNRs are only stable under pH conditions and above 7. This unexpected behaviour of the acids attached to a surface is explained by the proximity of negative charges to each other resulting in higher pka than the same acid in solution where the charges can move more freely[35]. This is the reason that encouraged us to work with basic pH (pH 10) to ensure the completely deprotonation of the carboxylic acid.

Despite conjugating GNRs under basic pH, we encountered irreproducibility problems with the stability of particles. Aggregation was systematically observed in GNRs exhibiting neutral surface charge; most likely caused by a mixture of positive CTAB and negatively charged ligand on the nanoparticle surface. Small differences in free CTAB amount present in the sample after purification can significantly alter the ligand exchange process due to the affinity of the surfactant for gold surface. When the process was slowed down due to the presence of surfactant, PEG molecules slowly attached to the surface until neutral charge was reached and therefore aggregation occurred. This prevented other molecules to be attached to the surface. It is noteworthy that at this point aggregation was irreversible. El-Sayed and co-workers also noticed this problem when working with SH-PEG-COOH and resolve it using a two steps process: first stabilizing particles with a Poly(ethylene glycol) methyl ether thiol and then replacing some of the ligands by SH-PEG-COOH[36]. Phase transfer has also been used as strategy to effectively pegylate GNRs.[37]

We propose here a simple two-steps process in aqueous solution where high reproducibility is accomplished through pH shifting. First addition of SH-PEG-

COOH is done under acidic conditions. Consequently, carboxylic acids on the ligand adopt the protonated form resulting in an intentional GNRs coagulation. Ligand attachment is enhanced like this due to two reasons; first, a higher number of PEG molecules are required to bind to gold surface before the total charge reaches a neutral value and colloidal stability is compromised. In addition, protonated forms are less bulky than the charged acids reducing steric and electric repulsion problems during conjugation, also leading to improving of the method efficiency. The second step involves the recovery of GNRs stability by shifting the pH to basic while adding a second set of PEG ligands. Figure 2.3 C summarizes this method. The strength of this approach is the maximization of the final number of ligands attached to GNRs during the first step of the process at the same time that reproducibility problems with colloidal stability are solved.

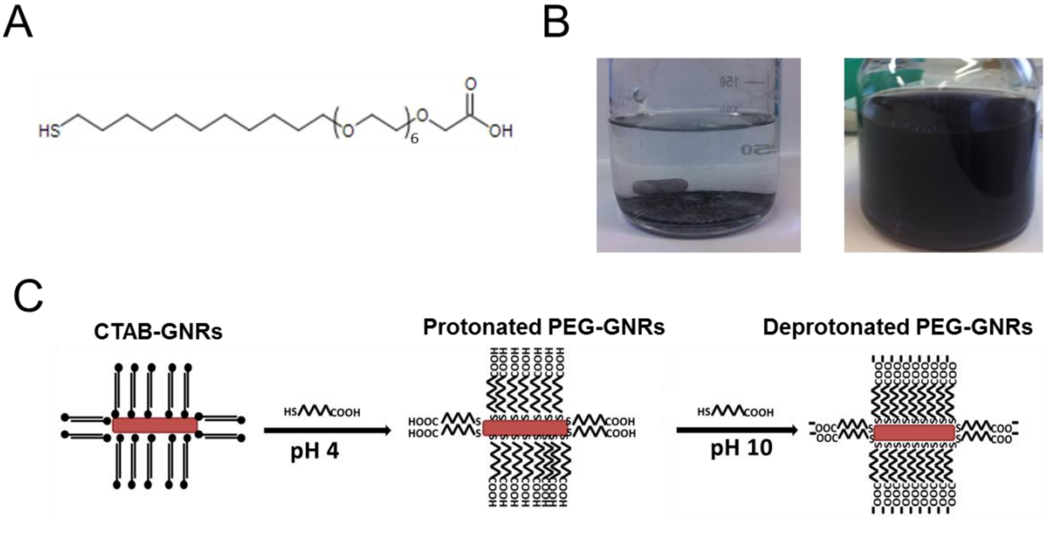

Figure 2.3: Surface modification of GNRs with SH-PEG-COOH. A) Chemical formula of PEG-COOH. B) Pictures of PEG GNR is acidic and in basic pH C) Diagram representing ligand exchange. I) CTAB coated GNRs II) intentionally non stable PEG modified GNRs, carboxylic acid is protonated due to an acidic pH III) Stable GNRs with deprotonated PEG in the surface due to a basic pH

The different steps of the method were characterized by means of zeta potential, DLS and UV-vis-NIR spectroscopy. The measured zeta potential data (Figure 2.4 C) is in agreement with the diagram showing the different steps of the surface (Figure 2.3 C). Shifts observed in the measured zeta potential can be correlated to the presence of protonated and deprotonated carboxylic groups. The product obtained in the first conjugation step under acidic condition led to a significant drop in the measured zeta potential reaching nearly the neutral charge (-8 mV) when compared to the highly positive CTAB coated GNRs (+50 mV). The surface charge of the intermediate specie was not enough to preserve the electrostatic repulsion, resulting in a controlled aggregation of GNRs. This was observed with naked eye (figure 2.3 B). The second step consisted on a second injection of ligands under basic pH, which triggered the recovery of colloidal stability. This was a fast process; it took seconds to completely reverse flocculation of GNRs. This suggests that the colloidal properties were restored through the deprotonation of carboxylic groups already attached to the particle surface due to shift in the system's pH conditions, rather than because of the attachment of new ligands. This observation was also validated by values obtained by zeta potential; there was a significant drop in surface charge when the intermediate and final products were compared. The latter reached a negative measured zeta potential of -32.2 mV. The repulsive potential energy created by this surface charge was strong enough to stabilize the dispersion. Figure 2.3 B shows the picture of the final dispersed SH-PEG-COO$^-$ coated GNRs. Stability was also assessed by UV-vis-NIR spectroscopy (Figure 2.4 A). PEG conjugation led to a small NIR shift in the spectrum. Nonetheless, signs of aggregation were not observed in the spectrum tested after conjugation under basic pH. PEGylated GNRs were also shown to be stable under physiological pH conditions of 7.4. Colloidal stability under physiological conditions is a premise for biotechnological applications. Finally, effectivity of PEG grafting was assessed by DLS measurements. An increase in the hydrodynamic diameter was observed when the coated GNRs were measured and compared to the diameter of as synthesized particles. This increase is attributable to PEG molecules attaching to gold surface. GNRs modified with SH-PEG 5000 also showed similar results. However, the hydrodynamic diameter obtained with SH-PEG-COOH is significantly smaller as it is expected from a less bulky ligand.

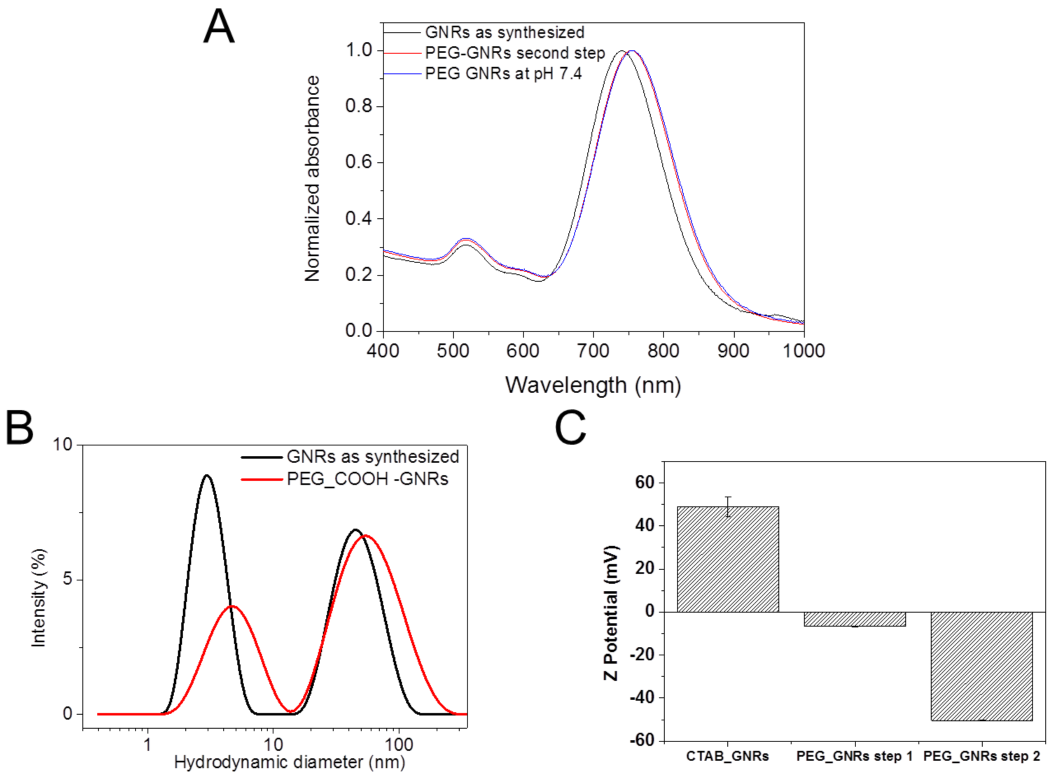

Figure 2.4 Characterisation of ligand exchange: A) UV-vis spectra of CTAB coated GNRs and SH-PEG-COOH modified GNRs B) DLS of CTAB coated GNRs and SH-PEG-COOH modified GNRs C) zeta potential of : I) CTAB coated GNRs (49.7±46.5 mV). II) Non stable PEG modified GNRs (-8.40±4.3 mV). III) Stabilized PEG modified GNRs (-32.2 ±15.3).

The chemical composition of SH-PEG-COOH modified GNRs was characterized by Fourier-transform infrared (FT-IR) spectroscopy. The spectrum obtained from modified GNRs was compared with the one of CTAB coated GNRs (figure 2.5 A and B respectively), as well as with the raw ligand's spectrum (Figure 2.5 C and D). The spectra of SH-PEG-COOH in solution and modified NPs showed similar peaks, indicating that the ligand forms part of the NPs composition (Figure 2.5 C). Specifically, IR spectrum obtained with PEG-COOH raw material showed a characteristic peak at 1111 cm^{-1} attributable to C-O-C stretching, the same peak was observed in the PEG modified GNRs at 1107 cm^{-1}. From the data acquired here, it is impossible to determine if CTAB molecules were still present in the sample or not after surface modification steps, since CTAB coated GNRs spectrum only showed two bands at 2848 cm^{-1} and 2918 cm^{-1}, these are distinctive of C-H stretching. PEG molecules are also composed by hydrocarbons and therefore it is impossible to determine if these bands, which were also present in the final product, correspond either to CTAB or SH-PEG-COOH. Some information about how the ligand binds to the gold surface could be extracted from the FTIR data. There is a weak peak at 2551 cm^{-1} that appears in the PEG raw material spectrum but it is absent in the modified GNRs (Figure 2.5). This peak is attributable to S-H stretch (s) binding and usually appears from 2560 cm^{-1} to 2510 cm^{-1} as a weak and narrow peak. The absence of this peak in the final spectrum might indicate that S-H bound is lost, confirming that the ligand binds to the gold in a quasi-covalent manner, dismissing the electrostatic binding.

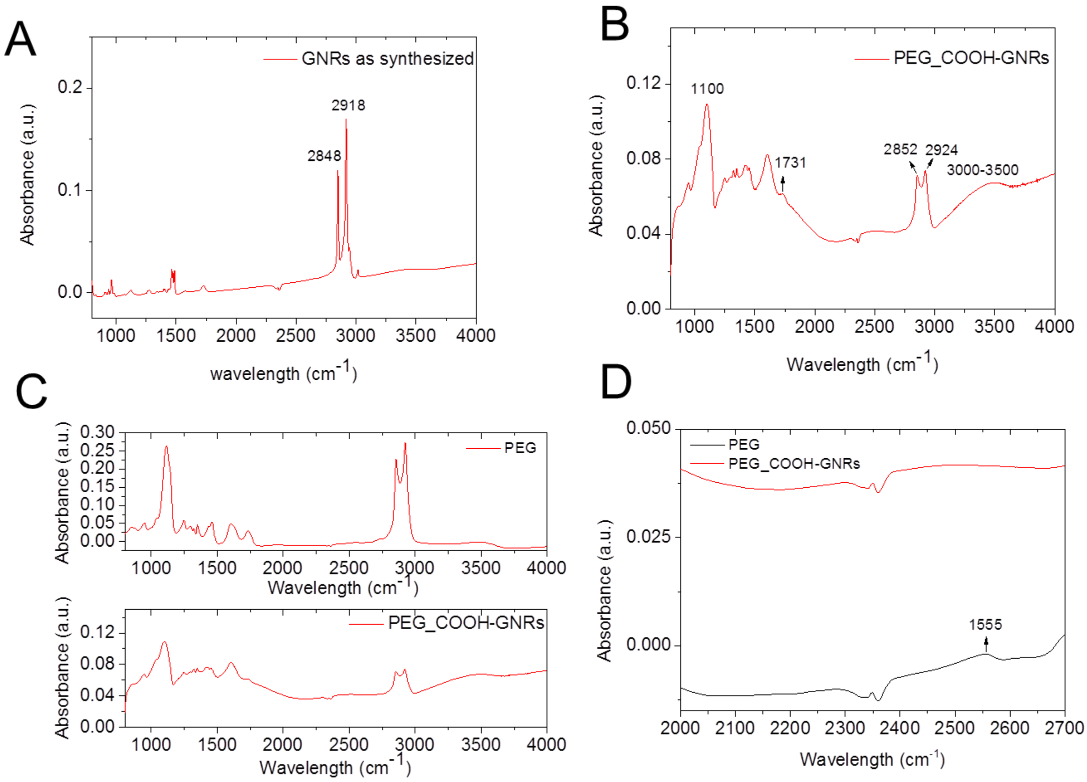

Figure 2.5: Composition characterisation of PEG-COOH GNRs by FT-IR. Readings are given in transmittance and were done at 1000 scans in transmission mode. A) FT-IR spectrum of CTAB coated GNRs B) FT-IR spectrum of PEG-COOH modified GNRs. C) and D) Spectra of raw PEG-COOH in black and PEG-COOH modified GNRs in red.

2.5 PEGylated Gold Nanorods as scaffolds for biomolecules

Functionalizing GNRs with SH-PEG-COOH has a main advantage comparing to SH-PEG 5000. Bifunctional ligands can be used for a broad range of applications since they can bind to the gold surface and to other structures simultaneously. Carboxylic groups on the surface of nanoparticles are available making possible a further modification. In this way, we have used PEGylated GNRs as scaffolds to build hybrid structures using NHS/EDAC chemistry. In this section, covalent binding of biomolecules to GNRs will be discussed. Following the same binding approach, a hybrid bimodal contrast obtained by the attachment of zinc gallium oxide nanoparticles (ZGO) to GNRs will be shown in the third chapter of this thesis.

Designing appropriate surfaces is not only important for colloidal stability but ligands on NPs surface can also trigger a biological response such as a cellular signalling.[38] From here stems the interest of conjugating biomolecules to nanoparticles. These hybrid materials allow the interactions of inorganic materials with biological systems resulting in a broad range of applications. Bio-sensing, targeting, cell uptake enhancement and drug delivery are examples of the potential of these hybrid structures.[39,40] The chemical strategy used to conjugate biomolecules to GNP is also crucial for the final result and the choice will depend on the condition particles are exposed to. Physiological environments pose an aggressive scenario for nanoparticles due to its high ionic strength. The presence of serum proteins in high concentrations also can affect NPs surface composition since proteins can form a dynamic layer on nanoparticles surfaces and even replace some of the ligands bound to the surface. These protein-nanoparticle interactions are known as protein corona[41] and they will be further discussed on subsection 2.5.2. Therefore, more stable binding that can endure over time under aggressive conditions are preferred for biological applications. Here, we will describe the covalent binding of biomolecules; specifically, a protein (section 2.5.2) and a peptide (section 2.5.3) to the GNRs using a carbodiimide crosslinker.

2.5.1 Activation of carboxylic acids: NHS/EDAC chemistry

Among the crosslinkers that can react with carboxylic acids, carbodiimide compounds are one of the most prevalent options for activating carboxylic acids.[42]

The versatility of this approach is one of the reasons for this since they can form a stable amide binding with a primary amine that acts as a nucleophile. This is especially interesting because it allows the binding of biomolecules rich in amines such as proteins and peptides. 1-Ethyl-3-(3-dimethylaminopropyl)carbodiimide (EDC) is a water soluble carbodiimide derivate broadly used for amide condensation.[43] Figure 2.6 summerizes the method.

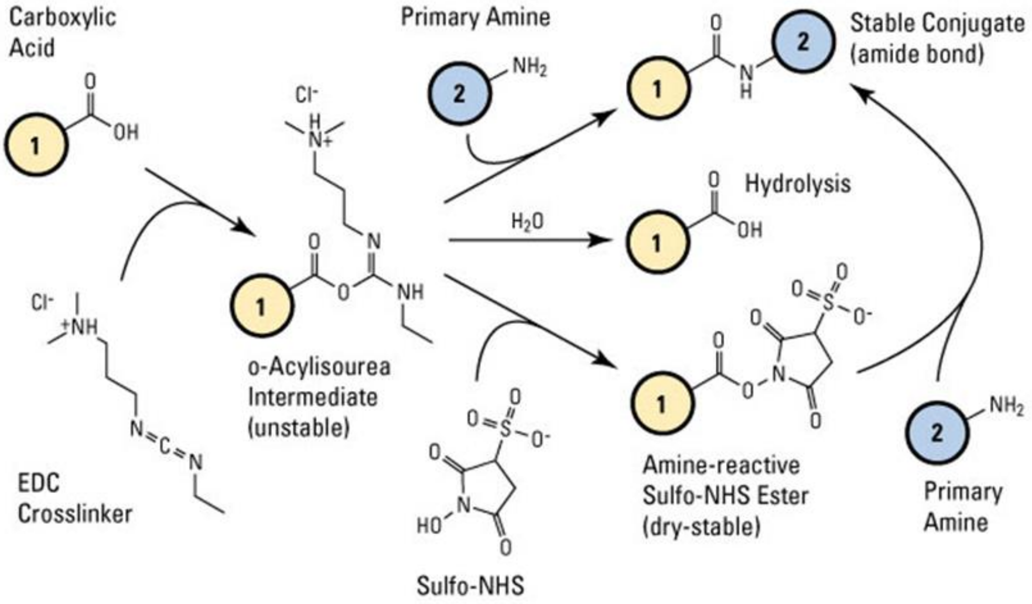

Figure 2.6: Activation of carboxylic acids by NHS/EDC crosslinker diagram. From thermofisher.com

The reaction intermediate is an stable but highly reactive ester. As it can be expected from an ester, the net surface charge was close to neutral. Figure 2.7 shows how the net charge of PEG-COOH-GNRs became less negative as the concentration of activator (a mixture of NHS/EDC) was increased confirming the success of the ester formation. As mentioned in section 2.4.2, PEG-COOH-GNRs are only stable when the carboxylic acid is deprotonated and a negative net charge is sufficient to electrostatically stabilized GNRs. The intermidate has a neutral charge and therefore colloidal stability can be affected. The solution is finding a compromise between the number of activated carboxylic acids and coloidal stability. Figure 2.7 shows that 2 µL of NHS/EDAC in 0.25 mL of GNRs ([Au]=0.625 mM, Absorbance at 400 nm was 1.5)[44] is enough to significally change zeta potential but still have a negative net charge required for stabilizing GNRs.

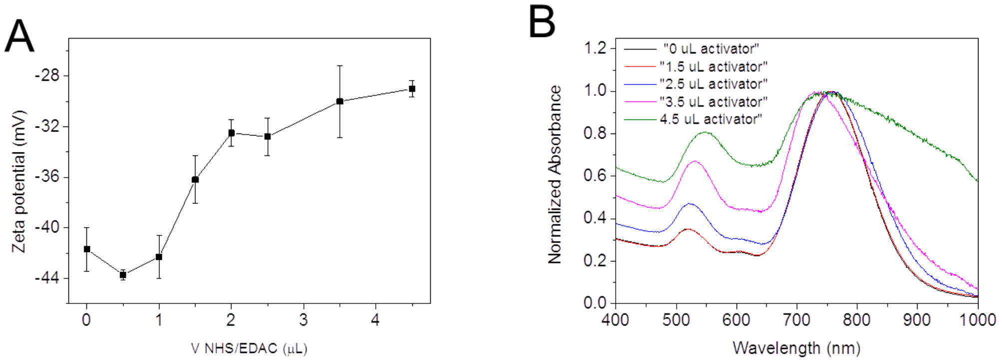

Figure 2.7: Activation of carboxylic acid by NHS/EDAC chemistry. A) Zeta potential of PEG-COOH-GNRs when volume of NHS/EDAC was increased. B) UV-Vis spectra of PEG-COOH-GNRs at different activation levels.

2.5.2 Conjugation with a protein: Bovine Serum Albumin (BSA)

The adsorption of plasma proteins on inorganic surfaces was first described by Leo Vroman in the 60's and this process was named after him as the Vroman effect[45]. In the same manner, when certain nanoparticles are in contact with physiological environments, proteins also cover the surface of nanoparticles[46]; this is known as protein corona. Protein corona is a spontaneous and dynamic process dominated by electrostatic or non-specific interactions. Interestingly, it has been proposed that protein corona can dictate NP fate in biological environments *via* receptor interactions.[46,47,48,49] Factors such as size, surface charge and stealth capacity of the ligands amongst others dictate the protein composition and dynamics of the corona. Many proteins have been described to interact with nanoparticles[50]; however we chose only the most abundant protein in serum, bovine serum albumin (BSA), to simplify our system. Albumin represents approximately the half of the total protein content in serum.

The main aims of this section are binding BSA covalently and compare the dynamics of covalent and electrostatic protein corona in physiologic conditions. Figure 2.8 summarizes the two strategies followed to conjugate BSA to GNRs. Both the corona formation and the covalent conjugation have been studied by DLS (figure 9).

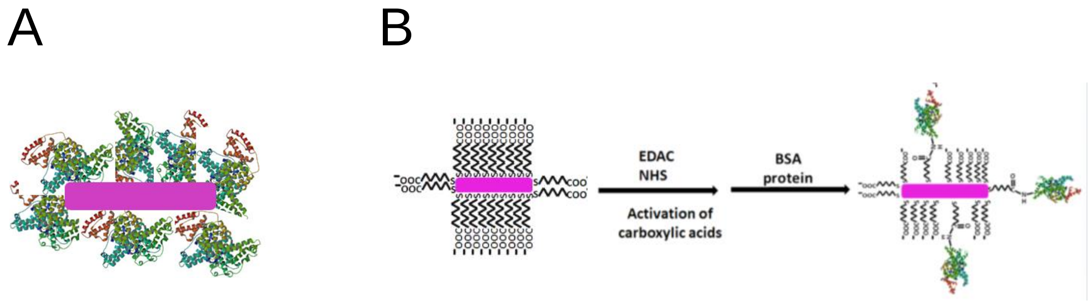

Figure 2.8: Scheme of the two strategies used to conjugate BSA to GNRs. A) Electrostatic protein-GNRs interaction B) Covalent binding of BSA to GNRs.

Carboxylic acids on the surface of GNRs were first activated with different concentrations of NHS/EDAC resulting in different zeta potential indicating that the level of activation can be controlled (see 2.5.2). Activated and non-activated GNRs were incubated with an excess of BSA for three hours at room temperature until the condensation reaction was completed. Then both BSA conjugates were purified twice in PBS. High ionic strength condition were chosen to promote desorption of unspecific bound proteins, at the same time the excess of proteins is reduced. DLS was measured and compared before and after purification. Casals *et al* studied the PC over time and described it as a two components process; a temporary or soft corona and a persistent or hard corona[51]. While the hard corona takes longer to be formed (48 hours at least); the soft corona is formed by a rapid equilibrium between bound and unbound protein. It was shown that the formation of soft corona intrinsically depends on the concentration of free protein. Therefore, when free protein concentration is decreased by purification of the conjugates, soft corona is reversible.[51] Following this approach, we characterized the efficiency of the covalent binding of BSA to GNRs since a lower desorption was only expected when BSA was covalently attached.

The protein-GNRs electrostatic interactions, i.e. before carboxylic activation, were first investigated (Figure 2.9 A). Negative charge of the carboxylic acid and relatively small molecular weight of SH-PEG-COOH quenches the inherent stealth nature of seen for larger PEG[18], facilitating the electrostatic interactions required for the protein adsorption. This has been confirmed by a shift to larger hydrodynamic diameter measured by DLS after incubation of GNRs with BSA (figure 2.9 A in red). The absence of big aggregates is a symptom that conformation of BSA was retained in our system. The retaining of the native conformation might be important for biological applications. Rotello and co-worker previously showed that the terminal carboxylic acid in a similar PEG molecule was needed for protein binding.[52] In addition, they also showed that ethylene groups prevented protein denaturalization in contrast to MUA ligands.[52] Therefore, our data are in good agreement with their findings.

Before washing with PBS, there was a significant increase of the hydrodynamic diameter in all the cases studied, non-activated and activated with different amounts of activator (Figure 2.7). This shift was observed in both components of the Brownian motion measured by DLS: translational and rotational relaxation rate (refer to section 2.4.1). This indicates that in all the particles tested, BSA is bound to NPs without any signs of denaturalisation.

After BSA treatment, the increase in the measured hydrodynamic diameter was bigger when carboxylic acids in the ligand were pre-activated with NHS/EDC. The difference between the non-activated and the highest concentration of activator was almost 12 nm in the rotational motion peak. In addition, a trend was observed in the hydrodynamic diameter measured by DLS when concentration of activator was increased (Figure 2.9 C black bars). This could mean that the covalent approach was more effective to recruit proteins from the solvent and less excess was needed to cover GNRs resulting in an increase of the hydrodynamic diameter. It could also be an indication that BSA is more or less buried in the ligand layer depending on the binding approach used. Pelaz *et al* found that the increase of the thickness of polymer modified FePt NPs was reduced by 50% when PEG was covalently bound to the polymer. Their fluorescence and quenching studies suggested that HSA could be buried between the PEG chains. They also correlated this finding to a decrease of cellular uptake when 10 KDa PEG was linked to the surface of the NP[53]. Alternatively, this increase in the hydrodynamic diameter could be due to a small change in protein conformation triggered by the amide bond formation. Our results are not conclusive to determine the cause of the difference observed between both approaches. Nonetheless, a direct relationship between activation and hydrodynamic diameter is clear, indicating that proteins interact with the ligand in a different manner depending on the chemical methodology used. In addition, there was a decrease in the diameter after purification in all the samples tested. Remarkably, there was a decrease in the hydrodynamic diameter regardless the activation of carboxylic acid (Figure 2.9 A and B in blue). This points to the formation of a soft protein corona on the surface of all the samples tested, even in the samples where carboxylic acids were previously activated. This was likely due to the fact that total activation of GNRs is not feasible as some charge need to remain to provide with colloidal stability. Non activated ligands can lead to the formation of a partial electrostatic corona on the surface. Nonetheless, while the diameter in the non-activated rods (figure 2.9 A) reaches virtually the same size as the PEG-COOH-GNRs before protein incubation, there is a significant difference between the control and the activated NP (figure 2.9 B and C). This can only indicate that the BSA protein is efficiently binding in a covalent manner to GNRs.

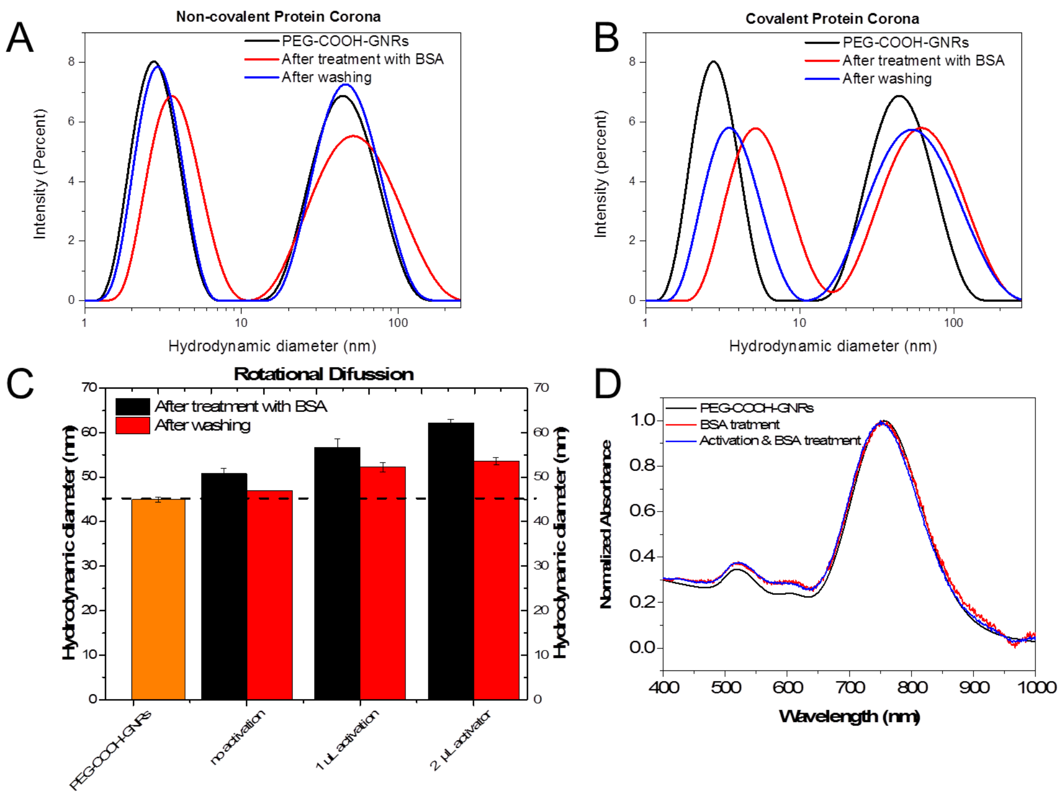

Figure 2.9: Characterisation of electrostatic and covalent BSA conjugation to GNRs. A) Hydrodynamic diameter measured by DLS of non-covalent BSA-GNRs interaction approach; PEG-COOH-GNRs before conjugation (black), after conjugation (red) and after washing (blue). C) Hydrodynamic diameter measured by DLS of covalent BSA-GNRs binding approach; PEG-COOH-GNRs before conjugation (black), after conjugation (red) and after washing (blue). C) Hydrodynamic diameter of the rotational Brownian motion component of GNRS before protein conjugation (orange), after conjugation (black) and after washing (red). D) vis-NIR spectra of GNRs after washing PEG-COOH-GNRs in black, after BSA treatment in red and previously activated GNRs in blue.

2.5.3 Conjugation with a cell penetrating peptide (CPP): Transactivator of transcription (TAT)

Cell penetrating peptides (CPP) are a group of relevant aminoacids sequences derived from proteins known for crossing biological membranes.[54] Proteins such as HIV transactivator of transcription (TAT)[55,56], *antennaepedia homeodomain*[57,58], Herpes Simplex Virus (HSV) VP22 [59]. Signal sequences[60] have also been studied as cell penetrating peptides. Interest in CPP mainly stems from the need to find a tool to enhance cell uptake of different cargos, especially biologically active molecules. CPP have been shown to cross not only cell membranes but also other biological membranes including the blood brain barrier (BBB)[61] expanding the potential biological uses of these peptides. The first discovered CPP was the transactivator of transcription (TAT) with sequence GRKKRRQRRRPQ. It was isolated from human immunodeficiency virus 1 (HIV-1), critical for viral DNA transduction into animal cells. TAT peptide can be reduced down to a linear sequence of 9 amino acids; including 6 arginine and 2 lysine aminoacids. The ability to cross cell membranes of TAT was first described independently by Green *et al* [62] and Frankel *et al* [63] in 1998. Later, Farwell and co-workers delivered different large proteins inside the cells after covalent linkage of a sequence of 36 aminoacids delivered from TAT protein[64].

Similarly to the data presented in the previous section, TAT peptide was covalently bound to PEGylated GNRs using the same crosslinker and results obtained from electrostatic and covalent binding were also compared here. The difference with BSA is that, as mentioned before, TAT is a peptide rich in positive amino acids resulting in an average positive surface charge. Results shown in figure 2.10 correspond to purified conjugates. As it is expected from a positive ligand, after addition of TAT measured zeta potential shifted from a negative surface charge to a positive one, independently on the binding approach. After purification of the particles, zeta potential measures did not drop as it could be expected from an electrostatic interaction. This was likely because in this case electrostatic interactions between negatively charged GNRs and positively charged TAT were stronger than in the case of BSA. In addition, as vis-NIR spectrum shows in Figure 2.10 A, no aggregation was observed through the two different processes. Hydrodynamic diameter of the different conjugates was also measured by means of DLS. Data obtained from both conjugation strategies were significantly different here. While the shift observed after employing an electrostatic binding was not notable, when NPs have been previously activated there was a significant increase in the measured hydrodynamic diameter. TAT is a peptide and therefore a much smaller biomolecule than BSA. Possibly, a less bulky molecule can intercalate easier within the PEG chains leading to a much smaller hydrodynamic diameter. Or a conformational change of the peptide due to the covalent binding could be the reason for this increase in the hydrodynamic diameter. Nonetheless, it would be necessary to confirm these observations with a different technique. For instance, quantification of TAT peptide on nanoparticles can be performed by Ellman's test.

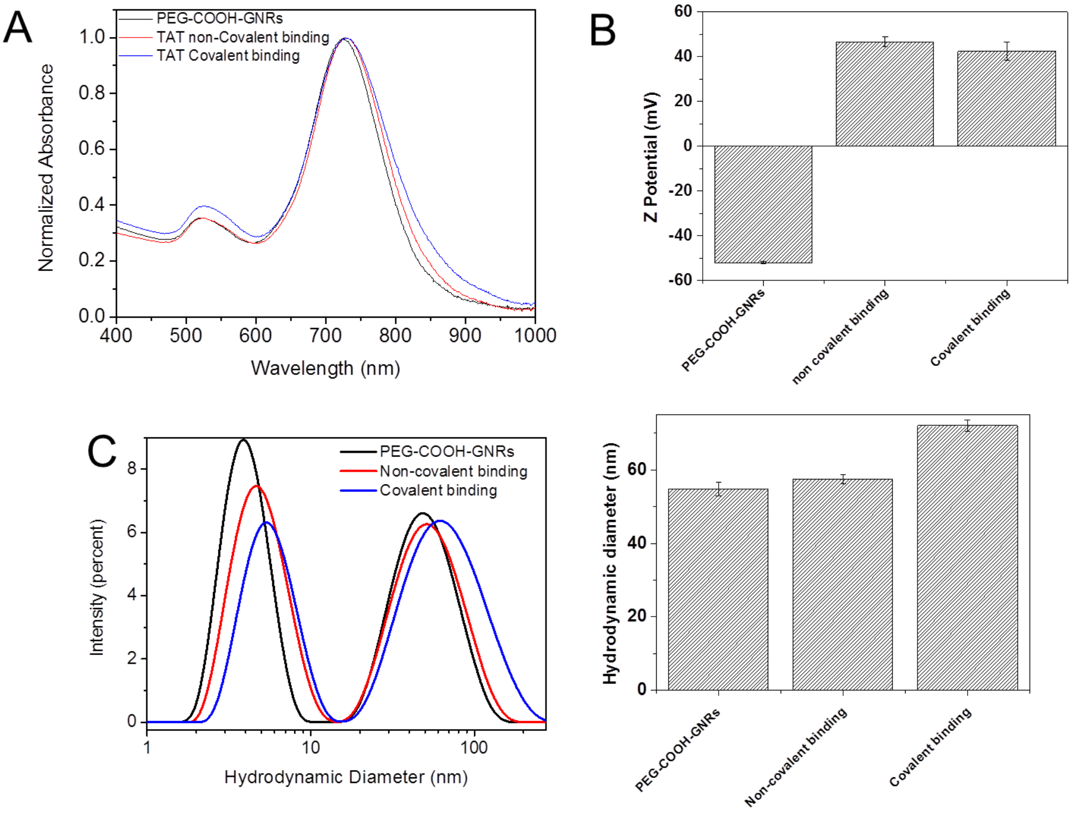

Figure 2.10: Characterisation of electrostatic and covalent TAT peptide conjugation to GNRs. A) UV-Vis-NIR spectra of PEG-COOH-GNRs (black), non-covalent TAT peptide-GNRs interaction (red) and covalent TAT-GNRs conjugate (blue) B) zeta potential of the different GNRs conjugated. C) Hydrodynamic diameter measured by DLS of PEG-COOH-GNRs (black), non-covalent TAT peptide-GNRs interaction (red) and covalent TAT-GNRs conjugate (blue). D) Hydrodynamic diameter of the rotational Brownian motion component of the different surface modifications.

2.6 Conclusions

GNRs with an A.R. ≈3 were synthesized by the seed-mediated growth method. Synthesis conditions were adapted to tune the LSPR peak position to around 750 nm, overlapping with the NIR window. Cytotoxic CTAB was replaced with PEG in order to obtain biocompatible GNRs, resulting in an improvement of colloidal stability even under physiological conditions. For this, the surface of GNRs was functionalised with a short chain SH-PEG-COOH following a two-step and pH-controlled protocol. It involved a controlled agglomeration of GNRs in acidic pH, followed by a second step under basic conditions to recover stability. This method allowed the surface replacement of the positive charged CTAB with a negative ligand, avoiding the irreversible aggregation caused by a mixture of CTAB and PEG molecules on the surface of GNRs. Irreproducibility problems due to small differences in the purification of CTAB were solved this way at the same time that ligand loading was improved. Another advantage that this method offers is that the carboxylic acids available on the surface of nanoparticles can be used as scaffolds for covalent binding of biomolecules or other structures. Here, BSA and TAT peptide were conjugated to PEG-GNRs via EDAC/NHS coupling chemistry. Versatility is the main advantage of this approach. Composites can be built with any structure containing amines, including other contrast agents to form a multi-modal probe (See section 3.6).

2.7 Bibliography

1. Dreaden, E. C., Alkilany, A. M., Huang, X., Murphy, C. J. & El-Sayed, M. a. The golden age: gold nanoparticles for biomedicine. *Chem. Soc. Rev.* **41,** 2740–79 (2012).
2. Liz-Marzán, L. M. Tailoring Surface Plasmons through the Morphology and Assembly of Metal Nanoparticles. *Langmuir* **22,** 32–41 (2006).
3. Link, S. & El-Sayed, M. A. Size and Temperature Dependence of the Plasmon Absorption of Colloidal Gold Nanoparticles. *J. Phys. Chem. B* **103,** 4212 (1999).
4. Grzelczak, M., Perez-Juste, J., Mulvaney, P. & Liz-Marzan, L. M. Shape control in gold nanoparticle synthesis. *Chem. Soc. Rev.* **37,** 1783–1791 (2008).

5. Huang, X., El-Sayed, I. H. & El-Sayed, M. A. Applications of gold nanorods for cancer imaging and photothermal therapy. *Methods Mol. Biol.* **624,** 343–357 (2010).

6. Huang, X., El-Sayed, I. H., Qian, W. & El-Sayed, M. A. Cancer cell imaging and photothermal therapy in the near-infrared region by using gold nanorods. *J. Am. Chem. Soc.* **128,** 2115–2120 (2006).

7. Lohse, S. E. & Murphy, C. J. The Quest for Shape Control: A History of Gold Nanorod Synthesis. *Chem. Mater.* **25,** 1250–1261 (2013).

8. Murphy, C. J. *et al.* Anisotropic Metal Nanoparticles: Synthesis, Assembly, and Optical Applications. *J. Phys. Chem. B* **109,** 13857–13870 (2005).

9. Weissleder, R. A clearer vision for in vivo imaging Progress continues in the development of smaller , more penetrable probes for biological imaging . Toward the phosphoproteome. *Nat. Biotechnol.* **19,** 316–317 (2001).

10. Tong, L., Wei, Q., Wei, A. & Cheng, J.-X. Gold Nanorods as Contrast Agents for Biological Imaging: Optical Properties, Surface Conjugation and Photothermal Effects. *Photochem. Photobiol.* **85,** 21–32 (2009).

11. Gole, A. & Murphy, C. J. Polyelectrolyte-Coated Gold Nanorods: Synthesis, Characterization and Immobilization. *Chem. Mater.* **17,** 1325–1330 (2005).

12. Alkilany, A. M. *et al.* Cellular uptake and cytotoxicity of gold nanorods: Molecular origin of cytotoxicity and surface effects. *Small* **5,** 701–708 (2009).

13. Fernández-López, C. *et al.* Highly Controlled Silica Coating of PEG-Capped Metal Nanoparticles and Preparation of SERS-Encoded Particles. *Langmuir* **25,** 13894–13899 (2009).

14. Ansar, S. M. *et al.* Determination of the Binding Affinity, Packing, and Conformation of Thiolate and Thione Ligands on Gold Nanoparticles. *J. Phys. Chem. C* **115,** 653–660 (2011).

15. Xue, Y., Li, X., Li, H. & Zhang, W. Quantifying thiol–gold interactions towards the efficient strength control. *Nat. Commun.* **5,** 4348 (2014).

16. Häkkinen, H. The gold–sulfur interface at the nanoscale. *Nat. Chem.* **4,** 443 (2012).

17. Thierry, B., Ng, J., Krieg, T. & Griesser, H. J. A robust procedure for the functionalization of gold nanorods and noble metal nanoparticles. *Chem. Commun. (Camb).* **1,** 1724–6 (2009).

18. Niidome, T. *et al.* PEG-modified gold nanorods with a stealth character for in vivo applications. *J. Control. Release* **114,** 343–347 (2006).

19. Chen, C.-C. *et al.* DNA−Gold Nanorod Conjugates for Remote Control of Localized Gene Expression by near Infrared Irradiation. *J. Am. Chem. Soc.* **128,** 3709–3715 (2006).

20. Castellana, E. T., Gamez, R. C. & Russell, D. H. Label-Free Biosensing with Lipid-Functionalized Gold Nanorods. *J. Am. Chem. Soc.* **133,** 4182–4185 (2011).

21. Oyelere, A. K., Chen, P. C., Huang, X., El-Sayed, I. H. & El-Sayed, M. A. Peptide-Conjugated Gold Nanorods for Nuclear Targeting. *Bioconjug. Chem.* **18,** 1490–1497 (2007).

22. Gole, A. & Murphy, C. J. Azide-Derivatized Gold Nanorods : Functional Materials for ‘ Click ’ Chemistry. *Langmuir* **24,** 266–272 (2008)

23. Alkilany, A. M., Thompson, L. B., Boulos, S. P., Sisco, P. N. & Murphy, C. J. Gold nanorods: their potential for photothermal therapeutics and drug delivery, tempered by the complexity of their biological interactions. *Adv. Drug Deliv. Rev.* **64,** 190–9 (2012).

24. Nikoobakht, B. & El-Sayed, M. A. Preparation and Growth Mechanism of Gold Nanorods (NRs) Using Seed-Mediated Growth Method. *Chem. Mater.* **15,** 1957–1962 (2003).

25. Scarabelli, L., Sánchez-Iglesias, A., Pérez-Juste, J. & Liz-Marzán, L. M. A ‘Tips and Tricks’ Practical Guide to the Synthesis of Gold Nanorods. *J. Phys. Chem. Lett.* **6,** 4270–4279 (2015).

26. Perezjuste, J., Pastorizasantos, I., Lizmarzan, L. & Mulvaney, P. Gold

nanorods: Synthesis, characterization and applications. *Coord. Chem. Rev.* **249,** 1870–1901 (2005).

27. Jokerst, J. V, Cole, A. J., Van de Sompel, D. & Gambhir, S. S. Gold Nanorods for Ovarian Cancer Detection with Photoacoustic Imaging and Resection Guidance via Raman Imaging in Living Mice. *ACS Nano* **6,** 10366–10377 (2012).

28. Scarabelli, L., Grzelczak, M. & Liz-Marzán, L. M. Tuning Gold Nanorod Synthesis through Prereduction with Salicylic Acid. *Chem. Mater.* **25,** 4232–4238 (2013).

29. Ye, X. *et al.* Improved Size-Tunable Synthesis of Monodisperse Gold Nanorods through the Use of Aromatic Additives. *ACS Nano* **6,** 2804–2817 (2012).

30. Scarabelli, L., Grzelczak, M. & Liz-Marzán, L. M. Tuning Gold Nanorod Synthesis through Prereduction with Salicylic Acid. *Chem. Mater.* **25,** 4232–4238 (2013).

31. Rayavarapu, R. G., Petersen, W. & Hartsuiker, L. In vitro toxicity studies of polymer-coated gold nanorods. *Nanotechnology* **21,** 145101 (2010).

32. Khlebtsov, B. N. & Khlebtsov, N. G. On the Measurement of Gold Nanoparticle Sizes by the Dynamic Light Scattering Method. *Colloid Journal* **73,** 118–127 (2011).

33. Glidden, M. & Muschol, M. Characterizing Gold Nanorods in Solution Using Depolarized Dynamic Light Scattering. *Journal of Physical Chemistry C* **116,** 8128–8137 (2012).

34. Schulz, F. *et al.* Effective PEGylation of gold nanorods. *Nanoscale* **8,** 7296–7308 (2016).

35. Wang, D. *et al.* How and why nanoparticle’s curvature regulates the apparent pKa of the coating ligands. *J. Am. Chem. Soc.* **133,** 2192–7 (2011).

36. Huang, X. *et al.* A reexamination of active and passive tumor targeting by using rod-shaped gold nanocrystals and covalently conjugated peptide ligands.

ACS Nano **4,** 5887–5896 (2010).

37. Wijaya, A. & Hamad-schifferli, K. Ligand Customization and DNA Functionalization of Gold Nanorods via Round-Trip Phase Transfer Ligand Exchange. *Langmuir* **24,** 9966–9969 (2008).

38. Liu, X.-Q. & Tang, R.-Z. Biological responses to nanomaterials: understanding nano-bio effects on cell behaviors. *Drug Deliv.* **24,** 1–15 (2017).

39. Nguyen, K. T. & Zhao, Y. Engineered Hybrid Nanoparticles for On-Demand Diagnostics and Therapeutics. *Acc. Chem. Res.* **48,** 3016–3025 (2015).

40. Eugenii, K. & Itamar, W. Integrated Nanoparticle–Biomolecule Hybrid Systems: Synthesis, Properties, and Applications. *Angew. Chemie Int. Ed.* **43,** 6042–6108 (2004).

41. Dobrovolskaia, M. a. *et al.* Interaction of colloidal gold nanoparticles with human blood: effects on particle size and analysis of plasma protein binding profiles. *Nanomedicine Nanotechnology, Biol. Med.* **5,** 106–117 (2009).

42. Al-Warhi, T. I., Al-Hazimi, H. M. A. & El-Faham, A. Recent development in peptide coupling reagents. *J. Saudi Chem. Soc.* **16,** 97–116 (2012).

43. Sperling, R. A. & Parak, W. J. Surface modification, functionalization and bioconjugation of colloidal inorganic nanoparticles. *Philos. Trans. R. Soc. A Math. Phys. Eng. Sci.* **368,** 1333 LP-1383 (2010).

44. Pastoriza-Santos, I. & Liz-Marzán, L. M. Reliable Methods for Silica Coating of Au Nanoparticles BT - Nanomaterial Interfaces in Biology: Methods and Protocols. in (eds. Bergese, P. & Hamad-Schifferli, K.) 75–93 (Humana Press, 2013). doi:10.1007/978-1-62703-462-3_6

45. Vroman, L. Effect of adsorbed proteins on the wettability of hydrophilic and hydrophobic solids. *Nature* **196,** 476–477 (1962).

46. Lynch, I. & Dawson, K. A. Protein-nanoparticle interactions. *Nano Today* **3,** 40–47 (2008).

47. Lynch, I., Dawson, K. A. & Linse, S. Detecting Cryptic Epitopes Created by Nanoparticles. *Sci. STKE* **2006,** pe14 LP-pe14 (2006).

48. Gray, J. J. The interaction of proteins with solid surfaces. *Curr. Opin. Struct. Biol.* **14,** 110–115 (2004).

49. Lesniak, A. *et al.* Effects of the presence or absence of a protein corona on silica nanoparticle uptake and impact on cells. *ACS Nano* **6,** 5845–5857 (2012).

50. Lundqvist, M. *et al.* Nanoparticle size and surface properties determine the protein corona with possible implications for biological impacts. *Proc. Natl. Acad. Sci. U. S. A.* **105,** 14265–70 (2008).

51. Casals, E., Pfaller, T., Duschl, A., Oostingh, G. J. & Puntes, V. Time Evolution of the Nanoparticle Protein Corona. **4,** 3623–3632 (2010).

52. Hong, R. *et al.* Control of Protein Structure and Function through Surface Recognition by Tailored Nanoparticle Scaffolds. *J. Am. Chem. Soc.* **126,** 739–743 (2004).

53. Pelaz, B. *et al.* Surface Functionalization of Nanoparticles with Polyethylene Glycol : E ff ects on Protein Adsorption and Cellular Uptake. *ACS Nano* **9,** 6996–7008 (2015). *ACS Nano* **9,** 6996–7008 (2015).

54. Biological evaluation of penetration domain and killing domain peptides. 908–917 (2005). *Journal of Gene Medicine* **7,** 908–917 (2005).

55. Frankel, A. D. & Pabo, C. O. Cellular uptake of the tat protein from human immunodeficiency virus. *Cell* **55,** 1189–1193 (2018).

56. Chen, L. L. *et al.* Increased Cellular Uptake of the Human Immunodeficiency Virus-1 Tat Protein after Modification with Biotin. *Anal. Biochem.* **227,** 168–175 (1995).

57. Astriab-Fisher, A., Sergueev, D., Fisher, M., Shaw, B. R. & Juliano, R. L. Conjugates of Antisense Oligonucleotides with the Tat and Antennapedia Cell-Penetrating Peptides: Effects on Cellular Uptake, Binding to Target Sequences, and Biologic Actions. *Pharm. Res.* **19,** 744–754 (2002).

58. Prochiantz, A. Messenger proteins: homeoproteins, TAT and others. *Curr. Opin. Cell Biol.* **12,** 400–406 (2000).

59. Phelan, A., Elliott, G. & O'Hare, P. Intercellular delivery of functional p53 by the herpesvirus protein VP22. *Nat. Biotechnol.* **16,** 440 (1998).

60. Hawiger, J. Cellular import of functional peptides to block intracellular signaling. *Curr. Opin. Immunol.* **9,** 189–194 (1997).

61. Banks, W. A., Robinson, S. M. & Nath, A. Permeability of the blood – brain barrier to HIV-1 Tat. *Experimental Neurology* **193,** 218–227 (2005).

62. Green, M. & Loewenstein, P. M. Autonomous Functional Domains of Chemically Synthesized Human lmmunodeficiency Virus Tat Trans-Activator Protein. *Cell* **55,** 1179–1188 (1988)

63. Frankel, A. D. & Pabo, C. O. Cellular uptake of the tat protein from human immunodeficiency virus. *Cell* **55,** 1189–1193 (1988).

64. Fawell, S. *et al.* Tat-mediated delivery of heterologous proteins into cells. *Proceedings of the National Academy of Sciences* **91,** 664–668 (1994).

Chapter 3

Synthesis and Surface Modification of Chromium-doped Zinc Gallium Oxide Nanoparticles

3.1 Introduction

The interesting optical properties of persistent luminescent (PL) phosphors; or alternatively called long persistent phosphors (LPP), have been used since the ancient China for decorative proposes. Currently, LPPs such as strontium aluminate ($SrAl_2O_4$) are broadly being used for safety signalling, decoration and military uses. Recently, PL materials have attracted a lot of attention due to their great potential in biomedical applications. Moreover, PL materials have risen as promising optical probes for bio-imaging due to the possibility of synthesizing these materials in the nanometre range and shifting both emission and excitation to the NIR/optical window.[1] In 2014 the number of publications was doubled over 2013[2], illustrating that persistent luminescent nanoparticles (PLNPs) is an emerging field. This increase in attention stems from the advances in the field done thanks to the development of new materials and synthetic routes. Here we summarize the most relevant preparative methods for these materials.

3.1.1 Synthesis of Persistent Luminescent Nanoparticles

Traditionally, solid-state reaction has been the most widely used method to synthesize LPP. Easiness of the method and possibility to scale up to mass production are the main reason for this popularity. The high temperature required to react solids normally reaches 1000-1500ºC and leads to crystals with extraordinary long emission times. The use of high temperatures creates more and deeper defects in the crystal surface, which are responsible for the long lifetimes shown by these materials. However, at the same time that temperature improves optical properties, it also leads to bigger and more poly-dispersed particles in the sample. The size usually obtained by this route of synthesis is in the order of microns. This situation is far from ideal for the use of LPP in biology and new synthetic routes have been described lately in the literature trying to give an answer for this problem. Still not a perfect approach that ticks all the boxes has been defined but advances in wet-chemistry and physical routes have been done in the past years[3]. The synthetic method influences optical properties, morphology, size and monodispersity. Therefore, reviewing the most common methods available before selecting the most convenient for the final goal is crucial.

Different approaches to synthesise luminescent nanoparticles can be found in the literature. The synthetic approaches based on liquid-phase synthesis are the most popular ones due to their easiness, lower cost, higher yields and versatility. Among them, sol-gel and hydrothermal synthesis are the most predominant strategies. Other approaches include physical methods such as laser ablation/deposition[4], and electron beam bombardment[5]. Here we will only focus on the ones based on liquid-phase synthesis due to their relevancy for our work.

Sol-gel method is one of the most common bottom-up methods for inorganic NPs synthesis. This method has also been broadly used for the synthesis of metal oxides, particularly silicon and titanium. Shortly, this method involves a two-step process; first a hydrolysis of the precursor, typically metal alkoxides or chlorides, followed by a condensation. The latter process leads to the formation of an integrated network or gel. The gel obtained needs then to be dried in order to remove the solvent. For the formation of LPP, a final calcination treatment is needed in order to achieve a further polycondensation state and mechanical properties improvement. This final thermal treatment notably enhances the optical properties achieving very long emission times (even hours). Starting bulk material used by Chermont *et al* was synthesized by solid state which resulted in the range of µm size particles. In order to synthesized smaller $Ca_{0.2}Zn_{0.9}Si_2O_6:Eu^{3+},Dy^{3+},Mn^{2+}$ particles they developed a sol-gel method followed by calcination, grinding and selective sedimentation. The final product was reported as 50-100 nm NPs with a narrow size distribution detectable for more than 24 hours.[1] In 2013 Liu and co-workers developed a new bulk material; trivalent chromium doped lithium gallate ($LiGa_5O_8:Cr^{3+}$) with superior optical properties[6], since emission lifetime after excitation with UV light was 1000 hours longer than any LPP known up to date. Similarly to Chermont *et al*, they used a sol-gel approach to synthesize this material in the range of nanometres. They reported a size range of 50-150 nm. However, due to the method procedure the emission times were shorter, up to 4 hours after UV excitation. Fu *et al* showed that the size of these material NPs could be easily tuned from 50 nm to 150 nm by controlling calcination temperature[7].

Hydrothermal synthesis is a crystallisation procedure where single crystals are formed under high pressures and temperatures higher than RT in aqueous solutions. The synthesis has to be carried out in a Teflon autoclave, a sealed steel cylinder which allows working under high pressures. Crystals of substances that are unstable under the melting point temperature can be obtained by this method. In addition, good quality single crystals are obtained at the same time that composition control is achieved. Indeed, hydrothermal synthesis has been broadly used for the synthesis of commercial single crystals such as synthetic quartz and gems. Maldeney *et al* published one of the most successful approaches to synthesize PL nanomaterials in 2014[8]. Chromium-doped zinc gallium oxide (ZGO:Cr) nanoparticles, with a chemical formula $Zn\ Ga_{1.995}Cr_{0.005}O_4$, were synthesized by hydrothermal method followed by a low temperature sintering (750ºC). The reported size of NP obtained by this approach was in the range between 20 and 60 nm, after selection by centrifugation. PL emission decay curve was taken for more than 80 minutes after UV excitation. Luminescent NPs were then used for successfully tracking macrophages in vivo. Hydrothermal method followed by sintering has been a prevalent method to slightly modify the composition of ZGO:Cr NPs. The host can be modified by introducing germanium molecules in the formulas and also co-dopants can be integrated in the crystals such as europium[9]. By this method, crystals are synthesized under relatively mild conditions which lead to homogeneous NPs, the methodology mentioned so far require a sintering process to activate the LPP also leading to bigger and poly-dispersed NPs. In 2015 Li and co-workers reported a hydrothermal methodology that does not involve high temperature treatments achieving like this, as small as sub 10 nm NPs and improving homogenicity[10].

Others: Template method is another well-developed method. LPP layer can be deposited on the surface of mesoporous silica nanospheres (MSNs) to form the MSNs@LPPs composite which can also be used for drug delivery.[11] NPs have also been prepared by other liquid phase methods including co-precipitation[12] and combustion[13].

Some conclusions can be drawn from the synthesis methods described. First, there are many approaches in the production of these crystals and all of them have different advantages and drawbacks. Physical methods are complex and expensive, while liquid-phase synthesis approaches are easier and cheaper, but have other drawbacks that need to take into account. For example in sol-gel methods, composition is highly controllable, and long lifetimes are achievable due to calcination step. However, they typically lead to a broad size distribution of bigger particles. Therefore, a physical post-treatment is usually needed to reduce their size. Hydrothermal method poses similar problems after the sintering process and template methods lead to lower yields and smaller particles are difficult to synthesize. Unfortunately, the high temperatures required for the activation of a longer and stronger PL is also responsible for the broad size distribution. Therefore, there is a need to develop new synthetic routes for LPP and optimize the morphology and size of NPs while improving optical properties. Some authors have tried to tackle this problem; Zou *et al* reported that NPs synthesized by hydrothermal synthesis could be protected by a silica shell during calcination. This silica could be removed by alkali etching afterwards. They reported an average size of 15 nm and a 3-fold signal enhancement compared to NPs before undergoing the calcination process[14].

3.2 Experimental

Reagents

The chemicals were purchased from Sigma-Aldrich and used as received. $Ga(NO_3)_3{\cdot}xH_2O$ (99.9%), $Zn(NO_3)_2{\cdot}6H_2O$ (≥99%), $Cr(NO_3)_3{\cdot}9H_2O$ (99.99%), ammonium hydroxide (28%), HCl (37%), Poly(allylamine hydrochloride) **(**PAH, MW 15 KDa) and Polyvinylpyrrolidone (PVP, MW 10 KDa), (3-Aminopropyl)triethoxysilane (APTES, 99%) Dimethyl sulfoxide (DMSO, ≥99.9%), *meso*-2,3-Dimercaptosuccinic acid (DMSA, 98%), *N*-Hydroxysuccinimide (NHS, 98%), *N*-(3-Dimethylaminopropyl)-*N′*-ethylcarbodiimide hydrochloride (EDAC, >98%). TAT peptide (97%) was purchased from Life Tein.

Preparation of ZGO

$ZnGa_2O_4$:Cr NPs were synthesized *via* hydrothermal synthesis adapted from a previous reported method.[10] Briefly, 2 mL of $Zn(NO_3)_2$ (1M), 1 mL of $Ga(NO_3)_3$ (2M) and 1 mL $Cr(NO_3)_3$ (4 mM) were pre-mixed under vigorous stirring and volume was adjusted to 15 mL with milli-Q water. 1 mL of ammonium hydroxide was added to the mixture to achieve a pH of 9-9.5 and left under gentle stirring for 30 minutes. The mixture was sealed into a Teflon-lined autoclave and transferred to an oven at 220° C for 10 hours. Once the hydrothermal reaction was finished, the autoclave was left to cool down at room temperature. The mixture obtained was centrifuged at 1000 g for 10 mins and the pellet was re-suspended in HCl (0.01M) to remove excess of Zn. HCl was finally washed off by centrifugation at 29000 g for 20 mins. Particles were further purified by 24 hours dialysis.

Surface modification

Polymers: 1 mL of $ZnGa_2O_4$:Cr NPs (at 0.3 mg/mL) was sonicated for 15 mins before adding drop-wise a solution of 100 µL PAH or PVP (20 mg/mL) under vigorous stirring. The mixture was left stirring overnight and the excess of polymers was washed off by centrifugation.

APTES: ZGO:Cr NPs were coated according to an existing method[1] with slight modifications. Briefly, 0.5 mL of $ZnGa_2O_4$:Cr NPs (2.5 mg/mL) in DMSO was sonicated for 15 mins before 20 µL of APTES (previously diluted x 100 times) were added drop-wise under vigorous stirring. The mixture was further sonicated for three minutes and left stirring overnight. Excess of APTES was washed off by centrifugation. The pellet was re-suspended in 1 mL of DMSO followed by 2 subsequent purification steps in milli-Q water.

DMSA: Modification with DMSA was adapted from a previously described method for iron oxide NPs.[15] 100 mL of ZGO:Cr nanocrystals (previously sonicated) were added to 100 mL of an aqueous solution of DMSA (0.1 mg/mL) under vigorous stirring and left to react overnight. Particles were purified and concentrated by centrifugation.

TAT: For the activation of DMSA-ZGO, 12 mg of EDAC and 24 mg of NHS were dissolved in 2 mL of 0.5 M MES buffer. 200 µL of the mixture were added to 200 mL of DMSA-ZGO (0.05 mg/mL). The suspension was incubated under continuous mixing for 1 hour at room temperature, followed by a subsequent centrifugation. 600 µL of TAT peptide (5 mM) were added to the activated DMSA-ZGO:Cr. The suspension was again incubated under vigorous stirring for 3 hours at room temperature. Finally, samples were purified by a centrifugation step.

Binding with GNRs: PEG_COOH-GNRs were activated as shown in chapter 2. 1 mL of GNRs was added drop-wise to 500 µL of APTES- ZGO (1.25 mg/mL). The mixture was left overnight under stirring. Particles were centrifuged at 6000 rpm and re-suspended in milli-Q grade water.

Characterisation

Vis-NIR spectroscopy was conducted in a Thermo scientific Genesys 10S UV-VIS. A Malvern Zetasizer nanoZS was used for dynamic light scattering and zeta potential measurements. For DLS, 3 measurements were carried out for 20 runs each measurement per sample, at 25°C (0.03 mg/mL of ZGO). For Zeta potential: Three measurements per sample were done in clear disposable zeta cell for 20 runs each measurement, at 25°C (0.03 mg/mL in 20µM NaCl solution, by Hückel). FT-IR measurements were conducted in a Bruker Lumus. 10 µL of previously purified samples were drop cast into a CaF_2 window and left to dry overnight. Measurements were taken in transmission mode (1000 scans at resolution of 4 cm^{-1}). Samples were imaged using a Tecnai G3 spirit TEM at 120 keV and HR-TEM and EDX was carried out on a JEOL JEM 2100FCs equipped with a spherical aberration corrector (CEOS GmbH), operating at an accelerating voltage of 200 kV. 10 µL of particles were deposited on a 3.05 mm copper grid (purchased from TAAB). Excitation and emission spectra were measured in a Horiba Fluoromax-4 (3mg/mL ZGO).

3.3 Synthesis of Chromium-Doped Zinc Gallium Oxide (ZGO) Nanoparticles

Zinc gallate nanoparticles have been synthesized following a single step hydrothermal method adapted from the methodology reported by Li *et al*[10]. Shortly, precursors were premixed and pH set to 9 before carrying the hydrothermal synthesis at 220°C for 10 hours. We chose this method because it produces good quality sub-10 nm and mono-dispersed single crystals. These crystals are ready functionalised and forming a stable colloid in aqueous solvent. Contrary to other approaches, no solid state annealing or sintering steps are needed. Consequently, no post-treatments such as ball milling are either required.

The final products are nanocrystals with a chemical formula as follows; $ZnGa_2O_4Cr_{0.004}$. Size of particles is tuneable by adjusting ratio of precursors. However, as conditions are changed to get bigger particles, the colloid become more polydispersed.[10] As it can be observed in Figure 3.1, under optimized conditions, the size distribution obtained is relatively narrow when compared with similar PL materials. The average size obtained is 6.3±1.16, figure 3.1 B shows the size distribution of NPs obtained after purification without performing any physical treatment or size selection. The ratio between Ga^{3+} and Zn^{2+} ions has big implications on the size and mono-dispersity of the sample. Optimal Zn/Ga molar ratio used here is 2:2. The excess of Zn that did not react to form crystals is thought to form either complexes with ammonium or ZnO as impurities that can be easily removed by washes with hydrochloric acid[10].

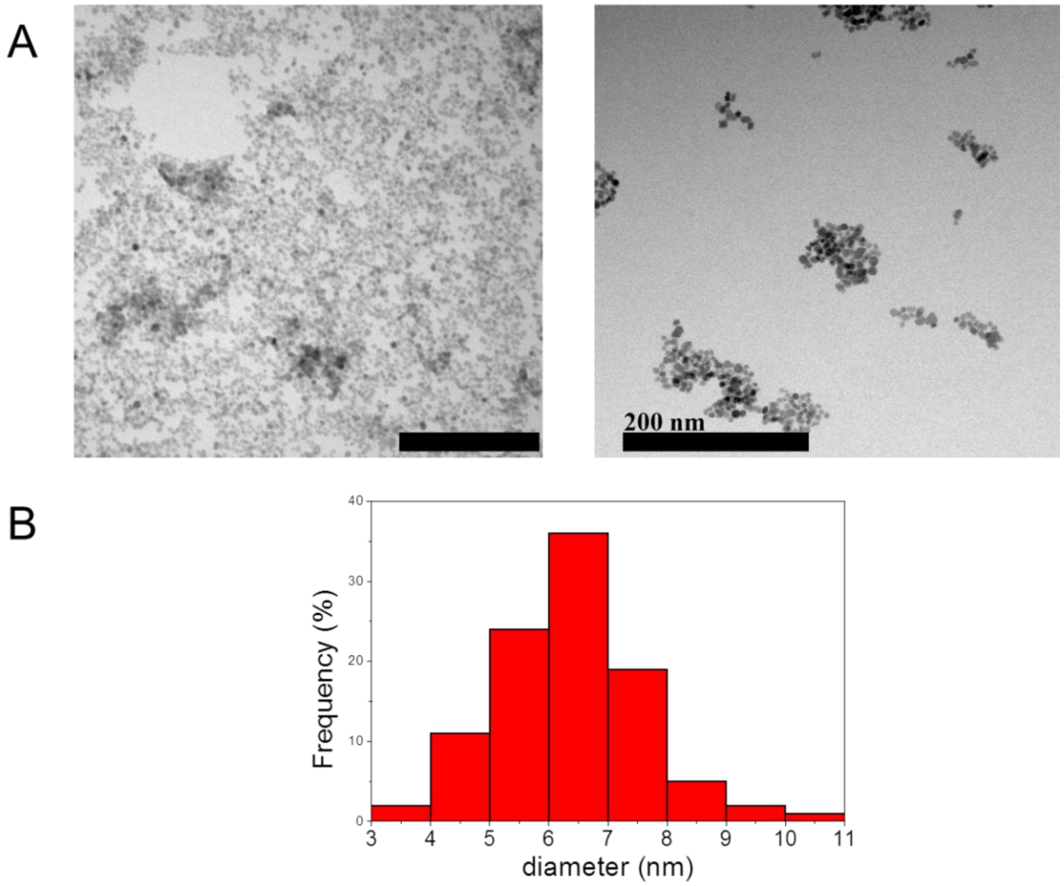

Figure 3.1: Synthesis of ZGO:Cr NPs A) TEM picture showing ZGO:Cr NPs as synthesised (Scales 200 nm). B) Size distribution.

3.4 Characterisation

3.4.1 Crystal structure and Elemental characterisation

Figure 3.2 shows HRTEM image of the ZGO:Cr NP and its highly ordered structure in atomic resolution, confirming the formation of a single crystal. With a interplanar distance of approximately 2.86 Å, which is in agreement with the interplanar (311) distance in the original work.[10]

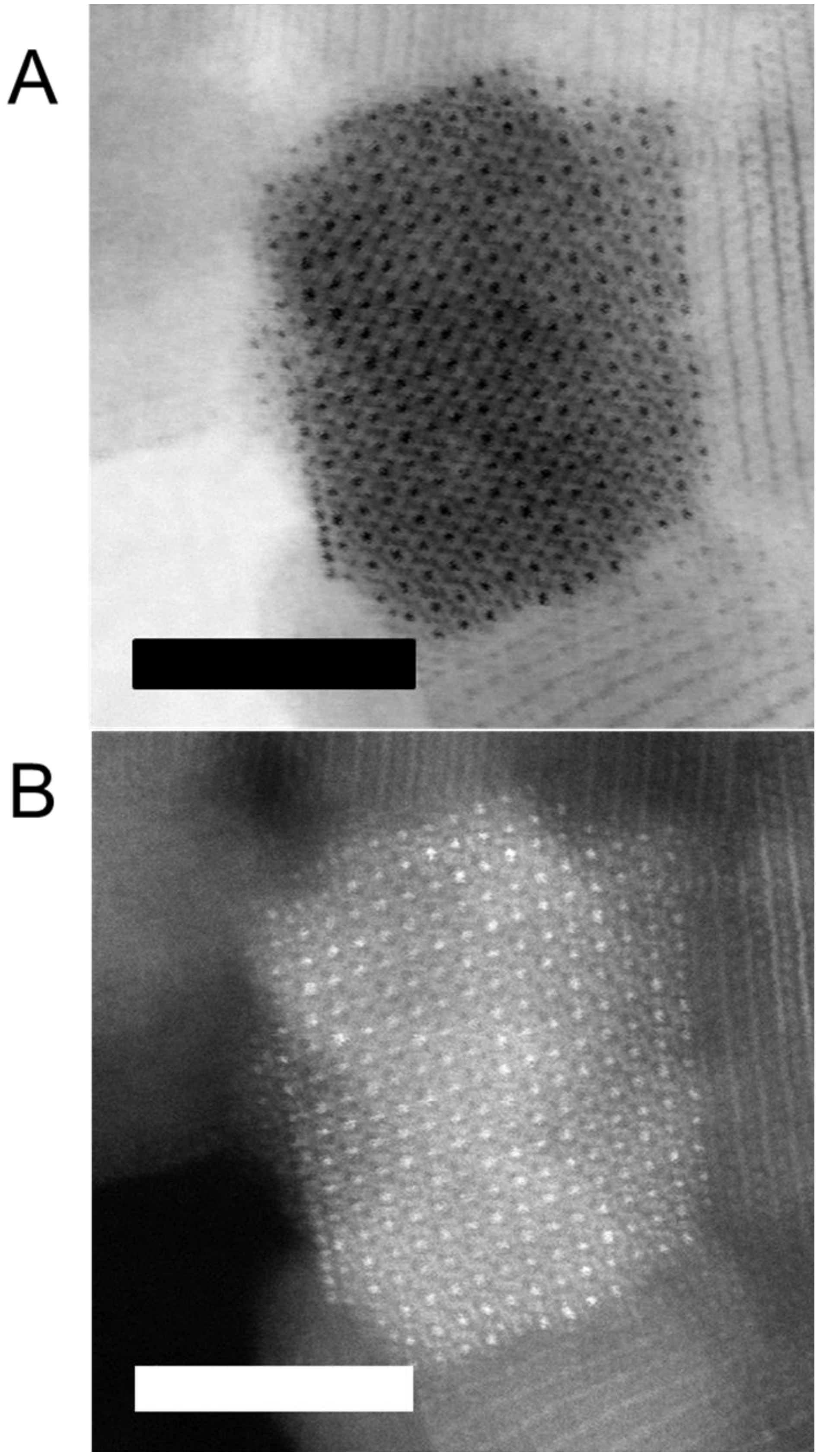

Figure 3.2: High resolution (HR) TEM of a single crystal. A) Bright field HR TEM image B) High angle annular dark field HR TEM. (Scale bars are 5 nm).

Crystal structure was studied by TEM electron diffraction. The pattern obtained by this technique is the same as the X-Ray diffraction (XRD) pattern in the reference paper[10] (figure 3.3 A). This confirms the formation of a pure cubic spinel crystal structure (JCDPS card no. 01-082-0466). Cr^{3+} ions can be easily brought together into the Gallium lattice forming a very stable structure due to the similar size and valence of both atoms.[7] ZGO followed a pure spinel structure (JCDPS card no. 01-082-0466) where the Zn^{2+} occupies the tetrahedral sites and Ga^{3+} the octahedral sites (Figure 3.3 B). Spinel crystals usually have the same general chemical formula: $A^{2+}B_2^{3+}O_4^{2-}$, composed by cubic close-packed oxides coordinated with four octahedral and two tetrahedral sites per formula. Usually, A^{2+} ions occupy 1/8 of the tetrahedral and B^{3+} 1/2 of the octahedral sites. However, it has been shown that around the 3% of the ZGO crystal is actually an inversed spinel, where 3% of Zn occupies Ga sites and *vice versa*, these sites are termed as antisite defects.[16,17,18] Following Kröguer-Vink notation, this defects are referred as $Ga^{\bullet}_{Zn}$ when a gallium ion is in a Zn site resulting in a positively charged defect; and Zn'_{Ga}, in this case Zn fills Ga forming a negative defect. These local charges in the crystal when they are close to the activator, in this case the doped Cr are believed to be the driving force for the trapping of the electron-hole.[8,17,18] Therefore, it is not surprising that modification of the ZGO structure has been a common strategy to improve the optical properties of this class of material. Bessière *et al.* showed that a deficiency of Zn leads to a longer and more intense luminescent signal[19]. Pan *et al* synthesised a LPP ceramic discs, with a decay time of more than 360 hours measured by a night vision system. They introduced Germanium (Ge) and formed a gallogerminate ($Zn_3Ga_2Ge_2O_{10}:Cr^{3+}$) to achieve those properties.[20] M. Allix and co-workers went one step further by replacing Ga atoms by germanium and tin in the ZGO matrix with a chemical formula $Zn_{1-x}Ga_{2-2x}(Ge,Sn)_xO_4:Cr^{3+}$ where $0 \leq x \leq 0.5$. Superior optical properties were obtained when x=0.1; they also showed that the mechanism behind this improvement was not related to the inverse spinel character like in ZGO, but to the distortion of the octahedral site close to the Ge and Sn positive defects forming new traps.[17]

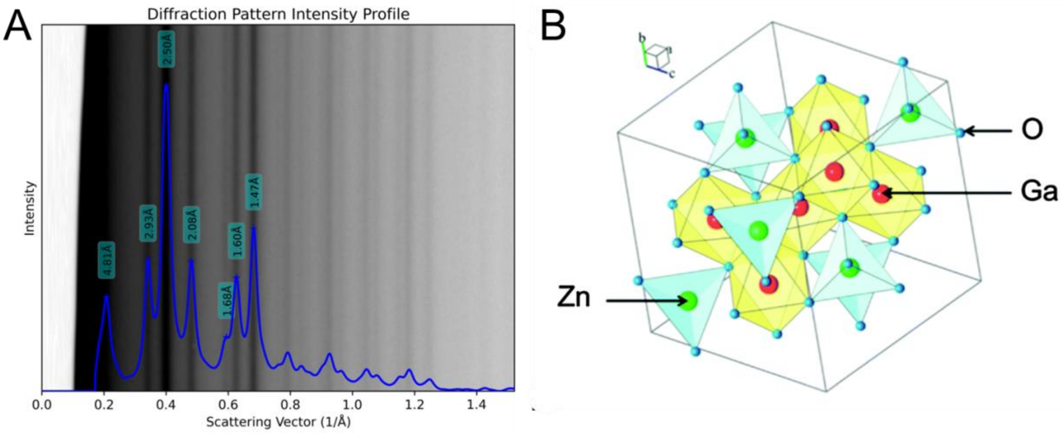

Figure 3.3: Crystal structure of ZGO. A) TEM electron diffraction of as synthesized ZGO:Cr crystals B) Crystal structure of ZGO. From reference 18.[18]

The composition of ZGO:Cr nanoparticles were studied by Energy-dispersive X-Ray spectroscopy (EDX). Data obtained by EDX shows that they are very close to the theoretical atomic percentage; 0.12% of Zn and 0.24% of Ga, (i.e. 1:2 Zn/Ga ratio). This also indicates that the excess of Zn formed impurities that were efficiently washed out afterwards.

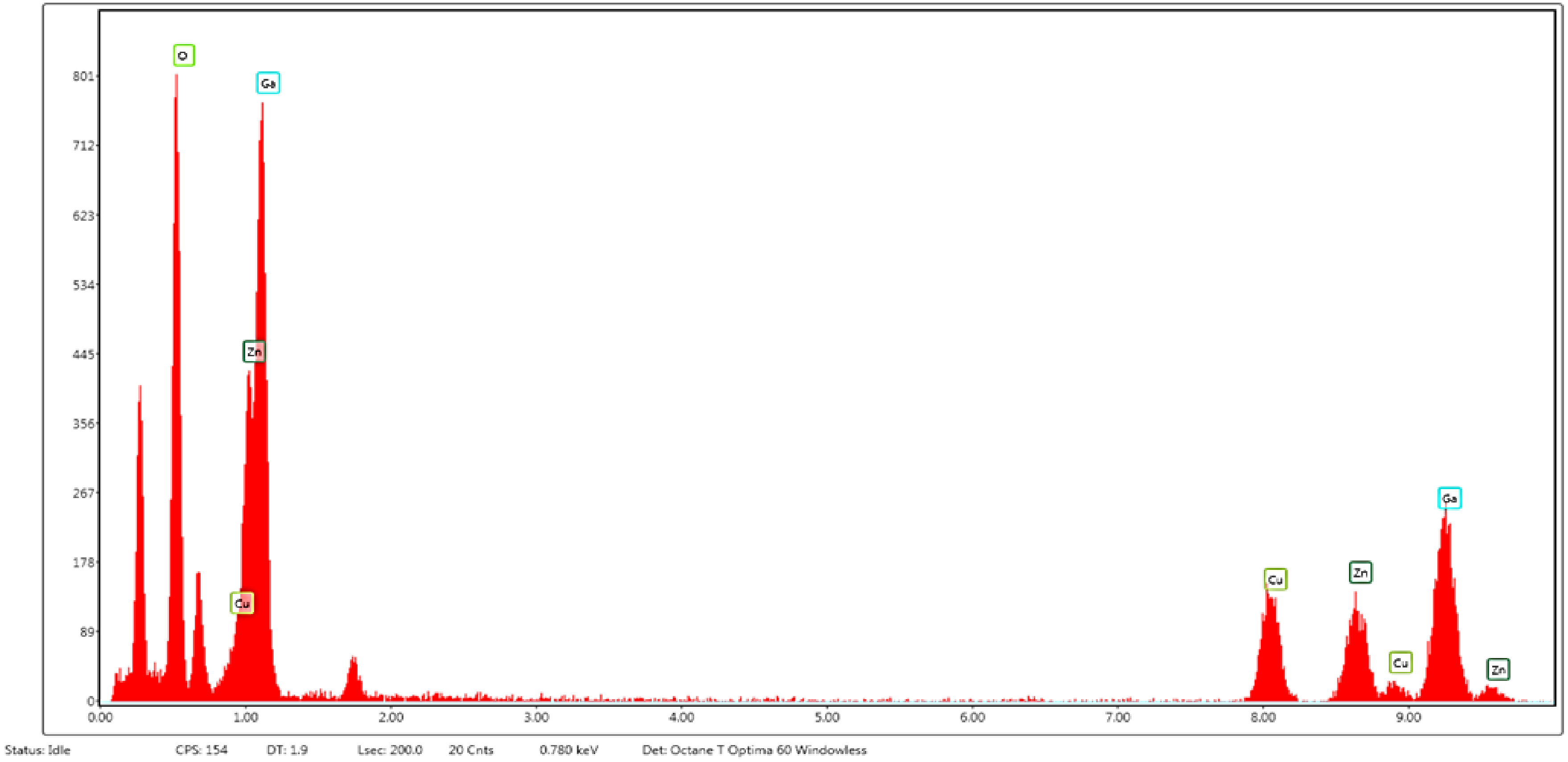

Figure 3.4: **Energy-dispersive X-Ray spectroscopy (EDX) of ZGO:Cr crystals.**

3.4.2 Optical properties characterisation

ZGO:Cr nanoparticles are part of a second generation PL NPs. The classification attends to the optical properties; this second generation of LP NPs has a special characteristic; excitation bands are within the NIR window, and more importantly, they can be re-activated by exposure to light, feature that is commonly referred as optical batteries. This represents a step forward in the use of LPP for long-term *in vivo* imaging. Understanding the role played by Cr as a dopant in our system is fundamental to explain its special optical properties. Interestingly, ZGO:Cr does not need to be pre-charged with UV-light, as it is the case of other materials such as $LiGa_5O_8$:Cr discs mentioned in chapter 1.

Excitation and emission spectra of ZGO:Cr nanoparticles synthesised by hydrothermal method following Li *et al* protocol[10] were measured (Figure 3.5 A). As expected from Cr^{3+} doped materials, we recorded a sharp emission band in the NIR region at 696 nm. This sharp emission spectrum in the NIR window make of Cr^{3+}-doped ZGO nanoparticles ideal candidates for *in vivo* imaging. Similarly to the excitation spectrum obtained by Maldiney and co-workers[8] (who synthesized ZGO:Cr by hydrothermal synthesis followed by sintering), our measurement shows a strong absorption band in the UV region of the spectrum. Bessière *et al* proposed that it corresponds to an excitation with a higher energy than the band gap.[19] There is a similar small excitation band in the range of 500 to 650 nm corresponding to lower energy than the band gap, matching the Cr^{3+} d-d transition[18]. This absorption band is especially relevant for *in vivo* experiments since is located close to the NIR window. This absorption band is responsible for the possibility to reactivate the particles once they are injected to the animal. Decay time is affected by changes in the depth of crystal defects. Afterglow time is directly proportional to the number and the depth of defects. Figure 3.5 B shows the room temperature intensity decay curve obtained with ZGO:Cr colloid before and right after exciting it by the fluorometer xenon lamp at 570 nm for 5 minutes. The curve intensity was recorded for~500 seconds, which is shorter than the reported for the same material obtained after sintering.

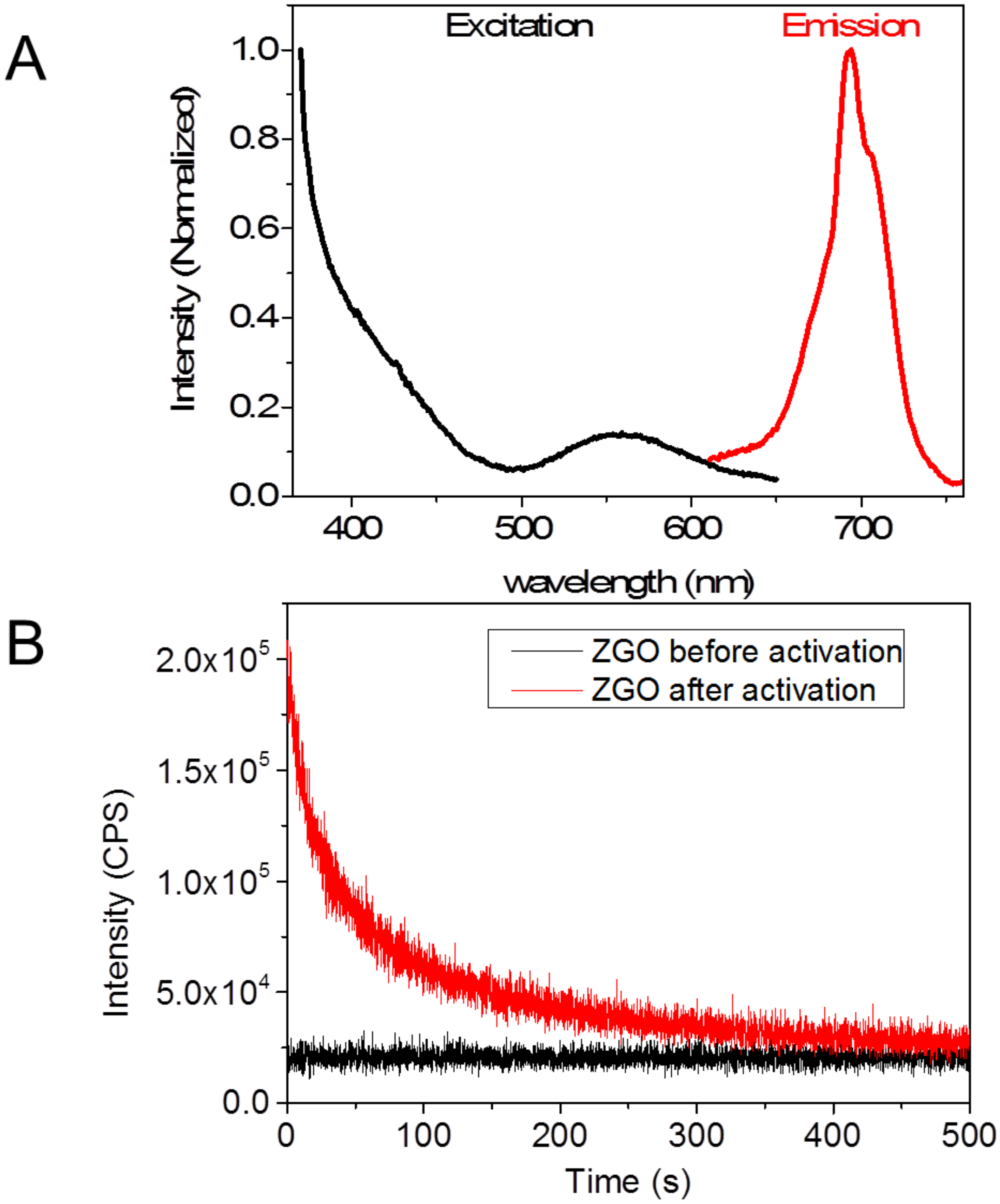

Figure 3.5: Optical properties of Cr:ZGO nanoparticles synthesized by hydrothermal method. Concentration of 3mg/mL of ZGO was used for the measurements. A) Excitation (in black) and emission (in red) spectra B) Intensity decay curve before and after excitation, in black and red respectively measured for 500 seconds at room temperature.

3.4.3 Colloidal stability characterisation

The final sintering step used by Maldiney *et al* seems to improve the optical properties of this material. However, as explained in the introduction of this chapter, sintering or generally high temperature treatments induce the formation of bigger NPs and broader size distributions. High temperatures also causes desorption of any molecules on the NP surface previously adsorbed during the liquid phase synthesis. This lack of surface molecules leads to very poor colloidal stability; therefore many authors opt for a hydroxylation by wet grinding of the powder obtained after the heat tratment[8,21,22,14,7,23,9]. The biggest advantage of the method used here is that mild conditions are used through all the synthesis process and therefore stable, small and monodispersed NPs are obtained. What is more, to the authors' and our knowledge, this is the only published method in which active LP nanoparticles are directly synthesised in aqueous-phase as a colloid.

DLS measurements of purified NPs in mQ water (Figure 3.6 B) confirmed the sharp size distribution calculated by TEM data (Figure 3.1 B). Typical zeta potential measurement of the particles as synthesised showed a consistent positive global surface charge (41.9±1.11 mV for this particular batch in neutral pH). Colloidal stability can be certainly attributed to the electrostatic repulsion created by the charge of nanoparticles in solution. Colloidal stability is a requirement for bio-medical application but it also influences the surface modification approach. In contrast to NPs synthesized by sol-gel method, no hydroxylation step is needed here and a direct functionalisation can be applied (see next section). We have tried colloidal stability in different media, as it can be expected from highly charged particles; stability is directly proportional to polarity of the solvent (Figure 3.6 A). As an attempt to study the surface chemical composition, FT-IR spectrum was studied after a thorough purification (Figure 3.6 C). FT-IR peaks at 3443, 1627 and 1411 nm could be attributable to the N-H stretching of primary amines. The only source of amines added during the synthesis was ammonia solution used to raise the pH of the solution. Therefore, according to this data, ammonia might be the molecule responsible for the colloidal stability of the as synthesized nanoparticles. In addition, the peak at 891 nm is also attributable to ammonia, confirming the presence of this molecule.

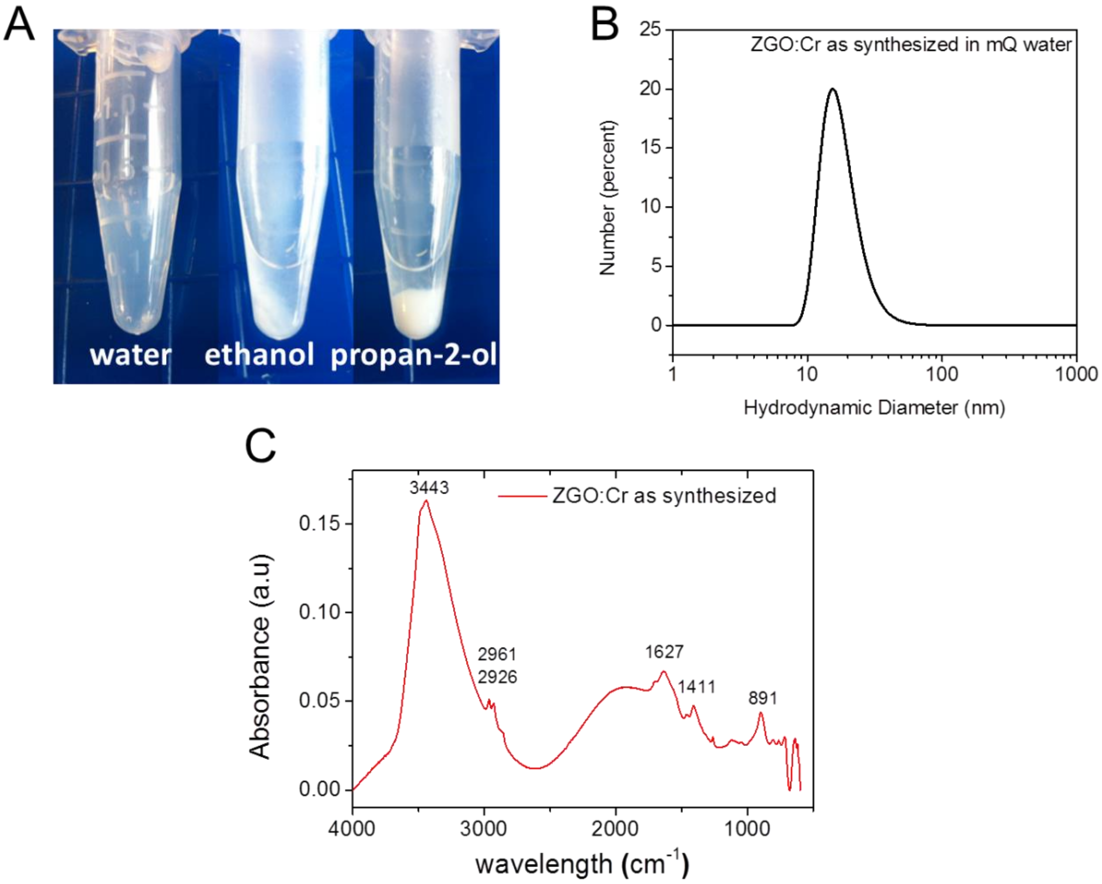

Figure 3.6: Colloidal properties of ZGO:Cr as synthesised. A) ZGO:Cr in different solvents. B) Hydrodynamic diameter measured by DLS of ZGO:Cr C) FT-IR spectra of as synthesized ZGO:Cr.

3.5 Surface Modification

Colloidal stability in complex environments such as physiological medium as well as control over the interaction with cells greatly relies in selecting a proper surface functionalization approach. Several factors need to be taken into account before selecting the most appropriate functionalization strategy. Mainly, which is the medium the nanoparticles are suspended and which surfactant/s are exposed. Exposure to high temperatures during the synthesis causes evaporation or desorption of molecules on the NPs' surface, ultimately leading to poor or complete loss of colloidal stability. For this reason, an intermediate hydroxylation of the surface is needed to recover colloidal stability before the final functionalisation can be achieved. On the other hand, when LPP NPs are synthesized readily dispersed in the solvent, this intermediate step is not needed broadening the election of appropriate ligands. In this section, four different surface modification approaches applied to ZGO:Cr NPs synthesized by hydrothermal approach are shown as well as characterization by means of DLS, Z-potential, TEM and FT-IR spectroscopy. First, polymers coating was used following an electrostatic approach. Silanization of ZGO was achieved through covalent binding of (3-Aminopropyl)triethoxysilane (APTES). DMSA was also proved to coordinate with ZGO:Cr surface and finally data obtained with bioconjugation of a CPP are shown here. All these functionalization strategies provided us with a library of candidates to be tested for cell labelling. Use of ZGO for cell labelling is an emerging field in which the *a priori* knowledge is limited and it needs to be tested. An ideal candidate should accomplish different parameters such as colloidal stability, abundant cell uptake, luminescence not affected, cell viability not compromised, which will be discussed in chapter 4 for the relevant candidates.

2.5.1 Electrostatic binding: Polymers

The use of polymer for modifying inorganic NPs is frequent due to its simplicity, efficiency and reproducibility. Li *et al* modified ZGO:Cr NPs with Poly(ethyleneimine) (PEI), a positively charged polymer[10]. Here we used two different polymers: Poly(allylamine hydrochloride) (15 KDa PAH) and Poly(vinylpolypyrrolidone) (10 KDa, PVP). 100 µl of polymer (20 mg/mL) were mixed with 1 mL of ZGO (0.3 mg/mL) overnight. Binding of polymers on the surface of the nanoparticles resulted in a significant increase of their hydrodynamic diameter as measured by DLS (Figure 3.7 A and B). Interestingly a bigger shift is observed when NPs are mixed with PVP, this is not attributable to a bigger size of the polymer, but probably to a different folding on the NP surface (note that in both cases, NPs surface were saturated since no further increase on size was observer after adding more polymer).

Surface charge of the resulting particles was also measured confirming the positive charge expected from this surface (Figure 3.7 B). As expected, PAH-ZGO showed a strong positive charge, whilst PVP-ZGO tend to a more neutral charge. Since, ZGO before functionalization exhibited a positive charge; we think DLS is more appropriate here to track the binding to these specific polymers.

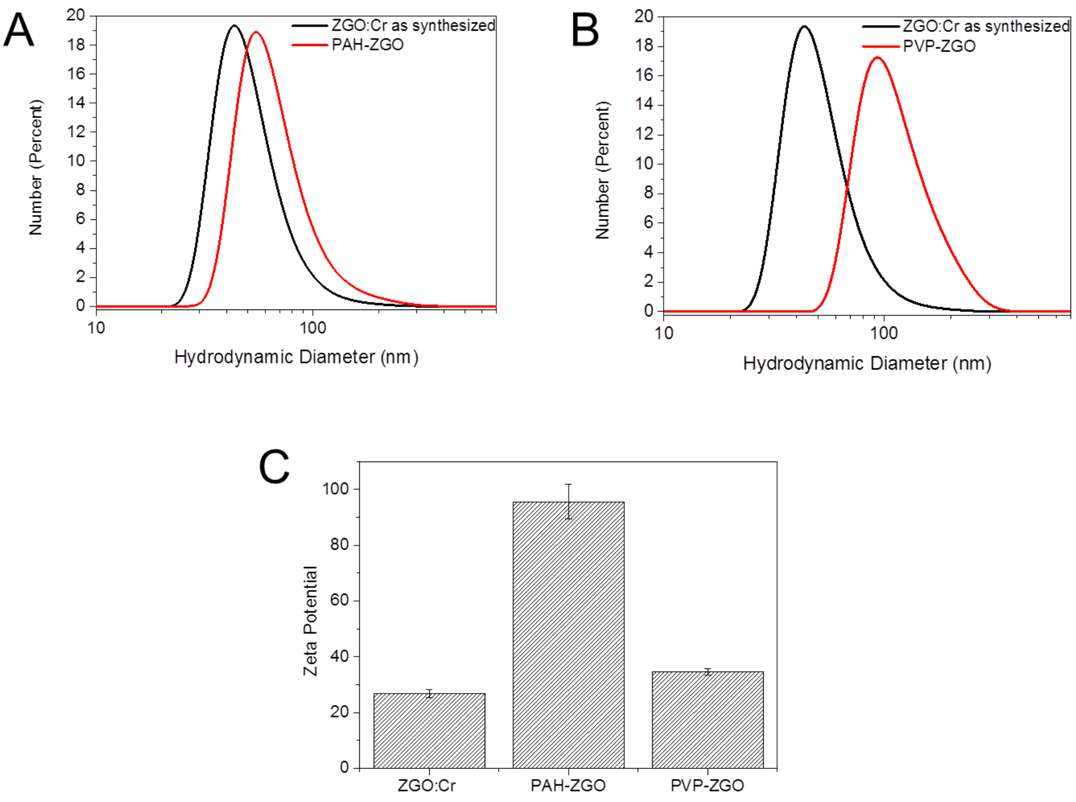

Figure 3.7: Characterization of ZGO:Cr polymer coating with PAH and PVP A) Hydrodynamic diameter measured by DLS of as synthesized ZGO:Cr (in black) and PAH coated ZGO:Cr (in red) B) as synthesized ZGO:Cr (in black) and PVP coated ZGO:Cr (in red). C) ζ potential of PAH and PVP coated ZGOs.

2.5.2 Covalent binding: APTES

Silanization is a common surface modification approach for metal oxide nanoparticles. In general, silica coated oxide NPs have previously been reported[24] as well as specifically coated LPNPs[25,14]. Silane derivatives such as bifunctional APTES has been broadly used to modified ZGO NPs since the silane binds to NPs surface while amine functionalisation allows further surface modification with a different ligands. Following this approach, PEG,[8,21]peptides[9,23,26] and cancer targeting ligands[27,22] have been conjugated to ZGO NPs.

APTES modified NPs were characterized by FT-IR spectroscopy (Figure 3.8 A). Two bands present at 1119 and 1035 cm^{-1} are only present in the modified NPs.

These bands are attributable to the Si-O-Si stretching, indicating that silane is part of the analysed sample. In addition, colloidal stability of APTES-ZGO:Cr was assessed by means of DLS (Figure 3.8 B). While the increase in hydrodynamic diameter indicates that the surface was modified, the decrease in intensity might indicate the presence of bigger structures. This is probably due to the need to carry APTES functionalization in organic solvents. As seen in section 3.4.3 synthesized ZGO:Cr are stable in mQ water but the stability of the colloid decreases with the increase of the hydrophobicity of the solvent. Some aggregation might be the consequence of working with other solvent than mQ water. Alternatively, a lack in the control of hydrolysis and condensation of APTES could be the problem. Data obtained by TEM (Figure 3.8 C) seems consistent with what was observed by DLS showing big agglomeration of NPs in some regions of the grid.

We could have introduced an intermediate functionalization step, which would have enabled the transfer of ZGO to organic solvent without losing colloidal stability in order to solve this problem. However, we were having good results with the functionalization with DMSA and we focus our efforts to this strategy instead (see next sections).

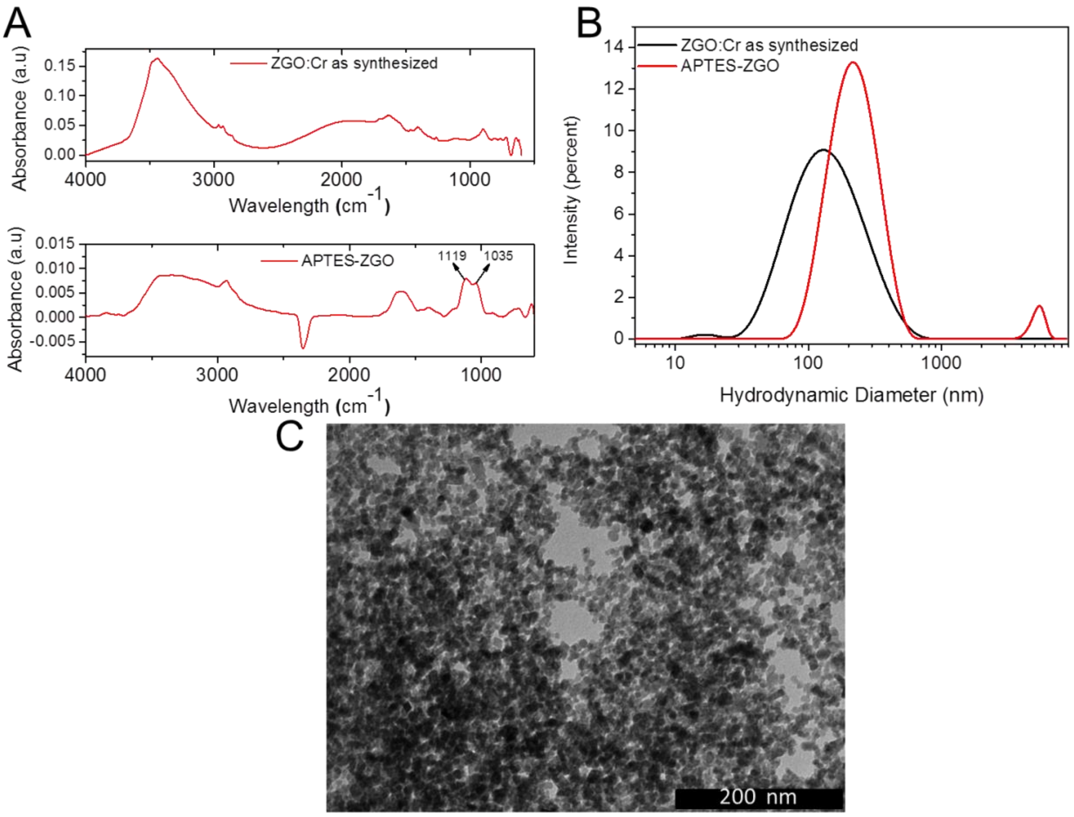

Figure 3.8: Characterization of APTES functionalization. A) FTIR spectra of as synthesized and APTES modified ZGO:Cr NPs. B) Hydrodynamic diameter measured by DLS of as synthesized ZGO:Cr (in black) and APTES-ZGO:Cr (in red) C)TEM picture of APTES modified ZGO:Cr (scale bar: 200nm).

2.5.3 Coordination binding: DMSA

Dimercaptosuccinic acid (DMSA) is a water-soluble and potent chelating agent and a drug used in the treatment of heavy metals poisoning approved by the FDA. It has previously been used for the functionalisation of gold nanoparticles[28,29], silver nanoparticles, iron oxide[29,15], zinc oxide nanorod arrays[30] and preparation of CdS quantum dots[31]. However, to the best of our knowledge, DMSA has not previously been used to functionalize LPNPs.

The formation of the NP-DMSA coordination complex formation was assessed here by changes of zeta potential from very positive (+49.7) of as synthesised ZGO NPs to very negative (-45.5 mV) after conjugation to DMSA. In addition, an increase in their hydrodynamic diameter was also observed confirming the success of the surface modification with DMSA. Although the binding mechanism of DMSA to Zn is not clear, it forms an efficient and strong complex with Zn atoms which improves colloidal stability of LPNPs.

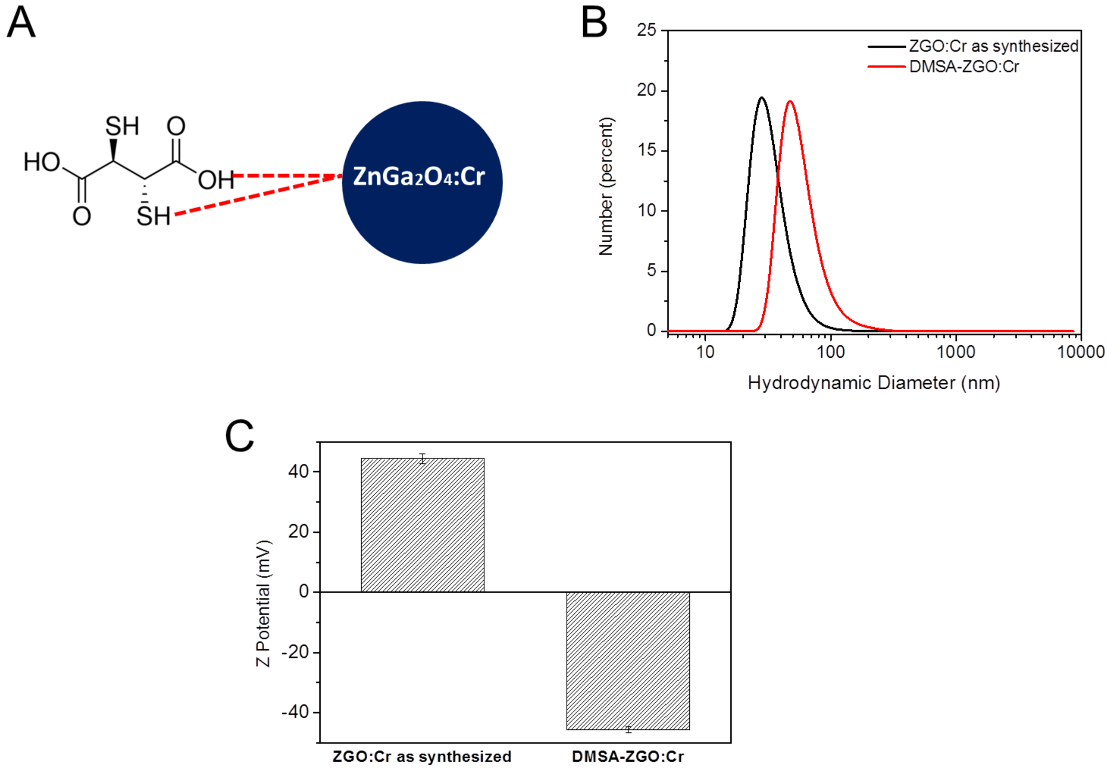

Figure 3.9: Characterization of DMSA functionalization. A) ZGO:Cr-DMSA coordination complex formation B) Hydrodynamic diameter measured by DLS of as synthesized ZGO:Cr (in black) and DMSA coated ZGO:Cr (in red) C) Zeta potential measurements of as synthesized ZGO and DMSA coated ZGO.

DMSA is a promising capping agent for biomedical research due to the ability to form strong and stable binding with NPs surface through metal coordination, water solubility, biocompatibility and tetra-functionalisation that offers the possibility to conjugate biomolecules. Bioconjugation with TAT peptide is discussed in the next section as a model peptide.

3.5.4 Bioconjugation with cell penetrating peptide

Similarly to the GNRs bioconjugation discussed in section 2.5.3 of Chapter 2, ZGO was modified with TAT peptide using the carboxyl acid available in DMSA as scaffolds for bioconjugation. Condensation reaction was carried out between the amine end of the peptide and activated carboxylic acid on LPNPs surface to yield an amide bound. Activation of carboxylic acid was accomplished by the use of a carbodiimide, EDC, and an active ester; NHS. This leads to a highly active intermediate that reacts with a primary amine forming an amide bound (See section 2.5.1). Using this system, HSA (human serum albumin) was previously bound to ZnO nanorod arrays using DMSA as a capping agent[30].

Here, bioconjugation was again assessed by measuring the hydrodynamic diameter and the surface charge of the NPs. Consistently, in each step of the process there was an increase of the hydrodynamic diameter, confirming the surface modification (Figure 3.10 A). In addition, Z potential measurements were in agreement with the data obtained by DLS (Figure 3.10 B). When carboxylic acids were activated, surface charge became less negative, Z potential shifted from -45.5 mV to -26.3 mV, confirming the formation of a neutral charged ester, but the composite remains still negative enough to stabilize the colloid (not all groups were activated). When TAT was conjugated to ZGO:Cr NPs surface charge of the hybrid material became positive, exhibiting a zeta potential of +39 mV. This confirmed the surface modification of TAT peptide, which is rich in positive aminoacids, conferring an average positive surface charge to the bioconjugate. We have conjugated TAT to ZGO:Cr NPs because it has been reported that cell penetrating peptide such as TAT can increase cellular uptake, which might be beneficial for our labelling purposes. [32] However, this strategy can be extrapolated to bind other type of molecules or structures that have an amino group available.

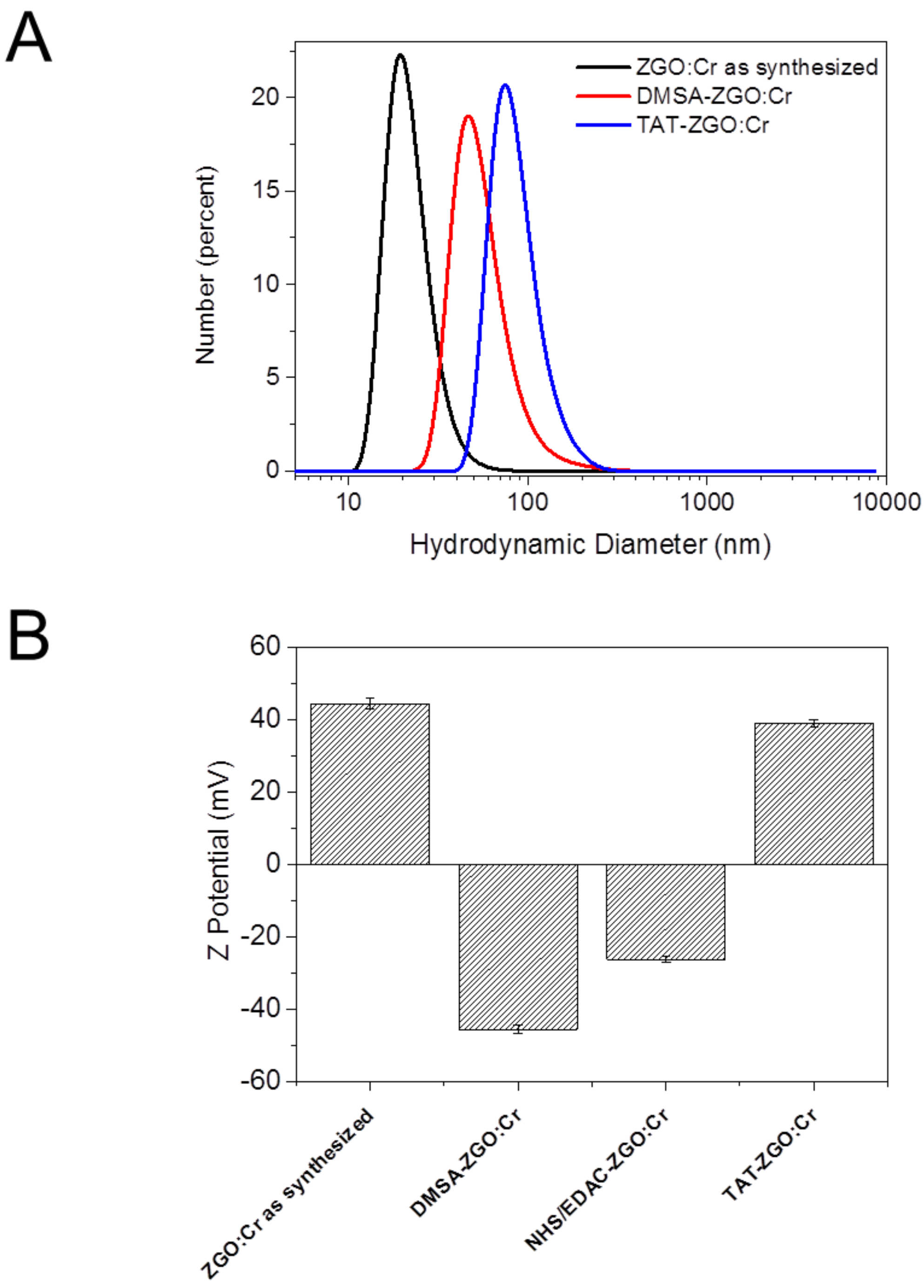

Figure 3.10: Characterization of TAT bioconjugation. A) Hydrodynamic diameter measured by DLS of as synthesized ZGO:Cr (in black) and DMSA coated ZGO:Cr (in red) B) zeta potential of unmodified ZGO:Cr, DMSA coated ZGO:Cr, intermediate activated ZGO:Cr and TAT conjugated ZGO.

3.6 Gold Nanorods-Zinc Gallium Oxide Bimodal Probe

An ideal probe or imaging system has not been established up to date. Moreover, every technique and their corresponding contrast agent have advantages and disadvantages. A possible solution is the imaging by two complementary techniques simultaneously. Indeed, one of the perspectives for NPs as contrast agents is multimodal imaging. Recent advances in imaging techniques allow the fusion of different imaging methods such as CT-PET coupled systems, already mentioned in section 1.1.[33] This combines the high spatial resolution of CT with the high sensitivity of PET. Under these promises, ^{18}F-doped cross-linked iron oxide (CLIO) have been successfully used to simultaneously image the liver and the blood pool of mice *in vivo*.[34] Radiolabelled isotopes have also been introduced in other NPs for multimodal imaging such as NIRF contrasts loaded in silica NPs in combination with optical imaging[35] and iron oxide NPs for MRI.[36]

Here, we used a core-shell approach where SH-PEG-COOH modified GNRs (See section 2.4.2) were used as scaffolds to bind APTES modified ZGO particles (See section 3.5.2) though EDAC/NHS amide condensation reaction (See section 2.5.1). Unfortunately, as it can be observed in the TEM image (Figure 3.11), binding of LPNPs was very efficient. This might be due to the tendency shown by APTES-ZGO NPs to agglomerate (Figure 3.11). A better control of the colloidal stability could lead to a better LPNPs shell formation around GNRs. An alternative to this method could be the use of DMSA coated ZGO:Cr, since DMSA functionalisation is carried out under hydrophilic conditions ensuring the stability of particles.

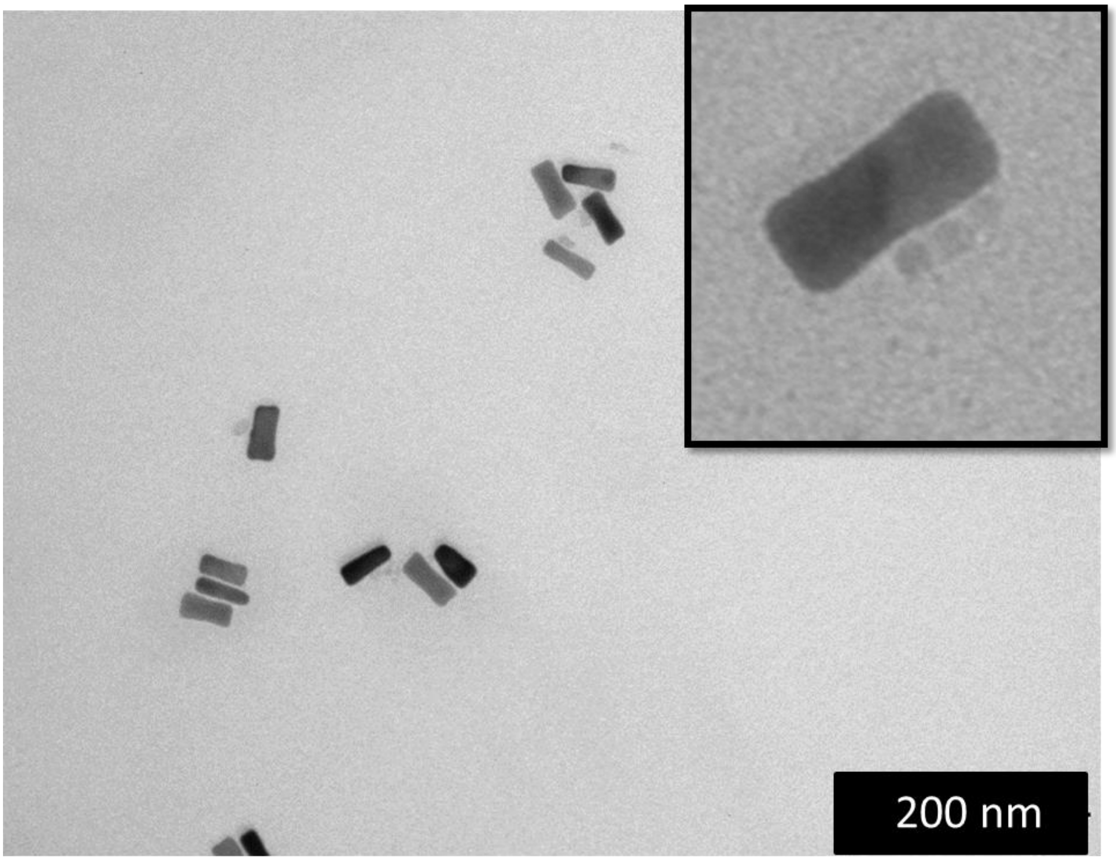

Figure 3.11: TEM image of GNRs-ZGO composites.

3.7 Conclusions

ZGO NPs were synthesized following a single step hydrothermal approach resulting in monodispersed nanoparticles with an average diameter of around 6 nm. A sharp emission at 696 was measured, appropriate for *in vivo* imaging. The crystal structure and elemental composition was characterized showing the presence of a pure cubic spinel crystal structure with a Zn/Ga ratio of 1:2. In addition, these as synthesized nanocrystals were stable in water.

Different surface modification strategies were studied such as polymer coating or APTES modification. Among the ligands used, DMSA was the most promising one for different reasons. First, it is a FDA approved treatment for heavy metal poisoning in humans. In addition, DMSA is soluble in water and a stable binding to ZGO NPs is achieved *via* metal coordination. This ligand also offers the possibility to conjugate biomolecules. In this chapter the bioconjugation with TAT peptide was shown as an example. DMSA has been used to modify the surface of different NP (GNPs, silver nanoparticles, iron oxide, zinc oxide nanorod arrays and CdSe quantum dots). However, to the best of our knowledge, DMSA has not previously been used for functionalizing LPNPs.

3.8 Bibliography

1. le Masne de Chermont, Q. *et al.* Nanoprobes with near-infrared persistent luminescence for in vivo imaging. *Proc. Natl. Acad. Sci. U. S. A.* **104,** 9266–9271 (2007).

2. Viana, B. *et al.* Long term in vivo imaging with Cr3+ doped spinel nanoparticles exhibiting persistent luminescence. *J. Lumin.* **170,** 879–887 (2015).

3. Li, Y., Gecevicius, M. & Qiu, J. Long persistent phosphors—from fundamentals to applications. *Chem. Soc. Rev.* (2016). doi:10.1039/C5CS00582E

4. Yang, L., May, P. W., Yin, L., Brown, R. & Scott, T. B. Direct Growth of Highly Organized Crystalline Carbon Nitride from Liquid-Phase Pulsed Laser Ablation. *Chem. Mater.* **18,** 5058–5064 (2006).

5. Smet, P. F., Avci, N., den Eeckhout, K. Van & Poelman, D. Extending the

afterglow in CaAl2O4:Eu,Nd persistent phosphors by electron beam annealing. *Opt. Mater. Express* **2,** 1306–1313 (2012).

6. Liu, F. *et al.* Photostimulated near-infrared persistent luminescence as a new optical read-out from Cr^{3+}-doped $LiGa_5O_8$. *Sci. Rep.* **3,** 1554 (2013).

7. Fu, X. *et al.* Long persistent near infrared luminescence nanoprobes LiGa 5 O 8 : Cr 3 + -PEG-OCH 3 for in vivo imaging. *Opt. Mater. (Amst).* **36,** 1792–1797 (2014).

8. Maldiney, T. *et al.* The in vivo activation of persistent nanophosphors for optical imaging of vascularization, tumours and grafted cells. *Nat. Mater.* **13,** 418–426 (2014).

9. Wu, S.-Q., Chi, C.-W., Yang, C.-X. & Yan, X.-P. Penetrating Peptide-Bioconjugated Persistent Nanophosphors for Long-Term Tracking of Adipose-Derived Stem Cells with Superior Signal-to-Noise Ratio. *Anal. Chem.* **88,** 4114–4121 (2016).

10. Li, Z. *et al.* Direct aqueous-phase synthesis of sub-10 nm ‘luminous pearls’ with enhanced in Vivo renewable near-infrared persistent luminescence. *J. Am. Chem. Soc.* **137,** 5304–5307 (2015).

11. Li, Z. *et al.* In Vivo Repeatedly Charging Near-Infrared-Emitting Mesoporous SiO\n 2\n /ZnGa\n 2\n O\n 4\n :Cr\n 3+\n Persistent Luminescence Nanocomposites. *Adv. Sci.* 1500001 (2015). doi:10.1002/advs.201500001

12. Xiao, Q., Xiao, L., Liu, Y., Chen, X. & Li, Y. Synthesis and luminescence properties of needle-like SrAl2O4:Eu, Dy phosphor via a hydrothermal co-precipitation method. *J. Phys. Chem. Solids* **71,** 1026–1030 (2010).

13. Peng, T. *et al.* Combustion synthesis and photoluminescence of SrAl2O4:Eu,Dy phosphor nanoparticles. *Mater. Lett.* **58,** 352–356 (2004).

14. Zou, R. *et al.* Silica shell-assisted synthetic route for mono-disperse persistent nanophosphors with enhanced in vivo recharged near-infrared persistent luminescence. *Nano Res.* (2017). doi:10.1007/s12274-016-1396-z

15. Jun, Y. W. *et al.* Nanoscale Size Effect of Magnetic Nanocrystals and Their

Utilization for Cancer Diagnosis via Magnetic Resonance Imaging. *J. Am. Chem. Soc.* **127,** 5732–5733 (2005).

16. Errandonea, D., Kumar, R. S., Manjón, F. J., Ursaki, V. V & Rusu, E. V. Post-spinel transformations and equation of state in ZnGa 2 O 4 : Determination at high pressure by in situ x-ray diffraction. 1–6 (2009). doi:10.1103/PhysRevB.79.024103

17. Allix, M. *et al.* Considerable improvement of long-persistent luminescence in germanium and tin substituted ZnGa2O4. *Chem. Mater.* **25,** 1600–1606 (2013).

18. Viana, B. *et al.* Storage of Visible Light for Long-Lasting Phosphorescence in Chromium-Doped Zinc Gallate. (2014). doi:10.1021/cm403050q

19. Bessière, A. *et al.* ZnGa 2 O 4 : Cr 3 + : a new red long-lasting phosphor with high brightness. **19,** 10131–10137 (2011).

20. Pan, Z. Sunlight-activated long-persistent luminescence in the near-infrared from Cr3+-doped zinc gallogermanates. *Nat. Mater.* **11,** 58–63 (2011).

21. Ramírez-García, G. *et al.* Functionalization and characterization of persistent luminescence nanoparticles by dynamic light scattering, laser Doppler and capillary electrophoresis. *Colloids Surfaces B Biointerfaces* **136,** 272–281 (2015).

22. Li, J. *et al.* Specific Recognition of Breast Cancer Cells In Vitro Using Near Infrared-Emitting Long-Persistence Luminescent Zn3Ga2Ge2O10:Cr3+ Nanoprobes. *Nano-Micro Lett.* **7,** 138–145 (2015).

23. Abdukayum, A., Chen, J., Zhao, Q. & Yan, X. Functional Near Infrared-Emitting Cr 3+ /Pr 3+ Co-Doped Zinc Gallogermanate Persistent Luminescent Nanoparticles with Superlong Afterglow for in Vivo Targeted Bioimaging. (2013). doi:10.1021/ja404243v

24. Ohmori, M. & Matijević, E. Preparation and Properties of Uniform Coated Inorganic Colloidal Particles: 8. Silica on Iron. *J. Colloid Interface Sci.* **160,** 288–292 (1993).

25. Paterson, A. S. *et al.* Persistent luminescence strontium aluminate nanoparticles as reporters in lateral flow assays. *Anal. Chem.* **86,** 9481–9488 (2014).

26. Zhang, L., Lei, J., Liu, J., Ma, F. & Ju, H. Biomaterials Persistent luminescence nanoprobe for biosensing and lifetime imaging of cell apoptosis via time-resolved fl uorescence resonance energy transfer. *Biomaterials* **67,** 323–334 (2015).

27. Zhao, H.-X., Yang, C.-X. & Yan, X.-P. Fabrication and bioconjugation of B III and Cr III co-doped ZnGa 2 O 4 persistent luminescent nanoparticles for dual-targeted cancer bioimaging. *Nanoscale* **8,** 18987–18994 (2016).

28. Uygun, D. A., Jurado-Sánchez, B., Uygun, M. & Wang, J. Self-propelled chelation platforms for efficient removal of toxic metals. *Environ. Sci. Nano* **3,** 559–566 (2016).

29. Silva, L. H. A. *et al.* Labeling mesenchymal cells with DMSA-coated gold and iron oxide nanoparticles: assessment of biocompatibility and potential applications. *J. Nanobiotechnology* **14,** 59 (2016).

30. Liu, T., Liao, H., Lin, C., Hu, S. & Chen, S. Biofunctional ZnO Nanorod Arrays Grown on Flexible Substrates. 5804–5809 (2016). doi:10.1021/la052363o

31. Sevinç, E., Ertas, F. S., Ulusoy, G., Ozen, C. & Acar, H. Y. Meso-2,3-dimercaptosuccinic acid: from heavy metal chelation to CdS quantum dots. *J. Mater. Chem.* **22,** 5137 (2012).

32. Josephson, L., Tung, C., Moore, A. & Weissleder, R. High-Efficiency Intracellular Magnetic Labeling with Novel Superparamagnetic-Tat Peptide Conjugates. 186–191 (1999). doi:10.1021/bc980125h

33. Townsend, D. W. Combined Positron Emission Tomography–Computed Tomography: The Historical Perspective. *Semin. Ultrasound, CT MRI* **29,** 232–235 (2008).

34. Devaraj, N. K., Keliher, E. J., Thurber, G. M., Nahrendorf, M. & Weissleder,

R. 18F Labeled Nanoparticles for in Vivo PET-CT Imaging. *Bioconjug. Chem.* **20,** 397–401 (2009).

35. Kumar, R. *et al.* In Vivo Biodistribution and Clearance Studies Using Multimodal Organically Modified Silica Nanoparticles. *ACS Nano* **4,** 699–708 (2010).

36. Xie, J. *et al.* PET/NIRF/MRI triple functional iron oxide nanoparticles. *Biomaterials* **31,** 3016–3022 (2010).

Chapter 4

Labelling Cells with Gold Nanorods and Chromium-doped Zinc Gallium Oxide Nanoparticles

4.1 Introduction

4.1.1 Transport Pathways Across the Cell Membrane

Cell membrane (CM) is the first and most relevant barrier a NP has to deal with to internalise inside cells. CM is a dynamic structure that protects cells from their extracellular environment. Its main function is to maintain homeostasis inside cells acting as a selective barrier regulating the entry and exit of ions and molecules. There are different mechanisms of transportations across the CM. While ions and small molecules can cross through passive diffusion or protein pumps and channels, big biomolecules are transduced into the cell through a process called endocytosis[1]. Although some small NPs (< 5 nm) have been reported to cross the CM in a receptor independent manner such as passive diffusion[2], it is agreed that the main mechanism of cell entrance for NPs is endocytosis.[3] Therefore, we will focus here on the different types of regulated endocytosis.

Endocytosis is a type of active transport that consists in an engulfment of molecules by membrane invaginations that leads to a pinching-off of fragments of the membrane, finally forming endocytic vesicles containing the different molecules and nutrients inside the cell. Endocytosis can be divided in two big types; phagocytosis and pinocytosis. Phagocytosis in mammals primary occurs in Phagocytes such as macrophages, monocytes and neutrophils. It is a highly specific process that is usually triggered by opsonisation, i.e. binding of opsonins such as immunoglobulins, blood proteins that are later specifically recognized by receptors on cell surface.[4] Different families of receptors are involved in phagocytosis such as scavenger receptors, Fc receptors and complement receptors. Binding of opsonins to these receptors triggers a signalling cascade mediated by Rho-family GTPases leading into the formations of phagosomes. Phagocytosis has special relevance in the inflammatory response against pathogens such as bacteria or in the clearing of apoptotic cells. Phagocytosis response to NPs has also been broadly studied after systemic injection.[5] Pharmacokinetics of nanocarriers can be compromised when detected by the mononuclear phagocyte system (MPS), previously referred as reticuloendothelial system (RES), reducing the circulation half-life of NPs. The use of sterically shielding polymers such as PEG have been shown to escape the MPS by protecting NPs from opsonisation which leads to an improvement of the pharmacokinetic profile by increasing the circulation time.[6] Doxil® is the first liposome-based chemotherapeutic drug approved by the FDA and it is a good example of the latter.

Pinocytosis, on the other hand, occurs in all cells and four main mechanisms have been described; chlathrin-mediated endocytosis (CME), caveolae-dependent endocytosis (CDE), Chlatrin/caveolae independent endocytosis (CIE) and macropinocytosis. CME takes place in a region of the membrane rich in chlathrin. Chlathrin is actively involved in the formation of vesicles in CME. Examples of receptors involved in CME include low-density lipoprotein (LDL) receptors, which play a role in the metabolism of cholesterol, and transferrin (TFn) receptors, which have been exploited for active drug delivery systems. Sometimes CME occurs in a receptor-independent manner. In these cases, non-specific hydrophobic or electrostatic interactions triggers cell uptake.[4] Another endocytic mechanism is CDE, involving caveolae, which are flak-shaped invaginations in cell membrane very abundant in both epithelial and non-epythelial cells.[7] CDE has been proposed to facilitate many physiological processes such as regulation of signalling cascades, homeostasis of intracellular cholesterol and other lipids and membrane tension.[8] An important role of CDE is the uptake of serum albumin (SA) though receptors Gp60 present in caveolae structures. Abraxane® is a cancer nanotherapeutic based on the binding of paclitaxel to albumin proteins. It exploits the albumin affinity toward this endocytic receptor, facilitating its transport across the tumour interstitial spaces, where paclitaxel is released.[9] Other membranes microdomains are involved in CIE. These lipid-rich microdomains are generally referred as rafts. The mechanisms and structures involved in this type of endocytosis are poorly understood.[1] However, folic acid has been reported to undergo this mechanism of cellular transport through folate receptors.[10] Folate-modified NPs are also uptaken after recognition and binding to this receptors.[11] Interestingly, particles undergoing cellular uptake by folate receptors are taken in endocytic compartments or directly transported into the cytoplasm.[12] Finally, macropinocytosis differs from the previous endocytosis pathways since it is based on a rearrangement of the protrusion of the CM that collapse and fuses with the membrane. This leads to the formation of big endocytic vesicles (0.2-5µm), referred as macropinosomes.[13] It is thought to play a role in the downregulation of signalling molecules such as some growth factors[14] and in immune surveillance.[15] This entrance pathway could be relevant for the cell uptake of larger NPs due to the big volume of macropinosomes.[16]

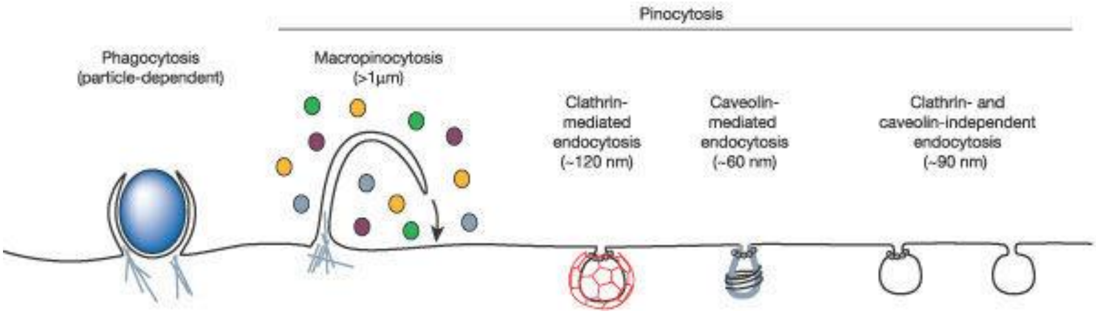

Figure 4.1: **Different mechanisms of endocytosis in the cell.** From reference 1

4.1.2 Cell Uptake of Nanoparticles

Cellular uptake is a crucial step in the development of NPs for biomedical applications. Therefore, a deep understanding of this process is needed for the design of effective NPs-based treatments. As it was shown before, entry to the cell is a highly regulated and sophisticated process where many factors play an important role. These factors can be divided in three main groups; physicochemical properties of NPs, the biological component and the experimental conditions (such as incubation time, temperature, cell type, etc.). [4]

The effect of physicochemical properties on NP-CM interactions has been thoroughly studied. Properties such as size, shape, charge and hydrophobicity have been reported to play a role in cell uptake. Regarding size, different studies conducted with macrophages indicate that larger NPs experienced a higher phagocytic internalization.[17-18] Furthermore, 50 nm NPs have been indicated to be the optimum size in different cell lines.[19] It has been theorized that 50 nm can occupy an elevated number of receptors while not being too big to pose problems with the membrane wrapping process.[20] In addition, size not only has a repercussion on the quantitative uptake of NPs but also dictates the intracellular localization. It was shown that while non-functionalized red quantum dots QDs (2.1 nm) accumulated in the nucleus and nucleoli of cells, red QDs (3.4 nm) were found in the cytoplasm.[21] Related to size is the effect that aggregation of NPs has on cell uptake. It is well-known that some NPs may aggregate when exposed to physiological conditions due to its high ionic strength. Both theoretical models[22] and experimental studies[23] agree that clusters or aggregates formation enhances cell uptake, probably due to a higher sedimentation rate. Shape of nanomaterials also modulates cell uptake. Different studies have highlighted the more efficient uptake shown by spherical shaped NPs compared to its rod-shaped counterpart.[24,19,25] Two possible explanations have been proposed; membrane wrapping of rods takes longer and also surfactants adsorbed in the longitudinal axis of rods could have a negative effect. Uptake experiments with different sized rod-shaped NPs have also been conducted and have concluded that Aspect ratio (AR) also plays a decisive role. Shorter rods with a smaller AR were shown to have a better uptake profile than those longer with bigger AR due to the longer wrapping time, previously mentioned.[26,19] It has also been proposed that not only longer GNRs inhibits cell uptake but also the absolute size/area value influences cell uptake.[27]

Surface charge has an important impact on the interactions of NPs with the CM as well. It was shown that positive and negative NPs underwent different endocytosis pathways in Hela cells. Cationic particles are internalized only via CME while negatively charged particles undergo both CME and caveolae-dependent endocytosis.[28] An extensive work has been done for a better understanding of the interactions between charged particles and CM all of them highlighting the importance of charge to trigger cell uptake. Molecular dynamic simulations showed that attraction of cationic NPs to membrane phospholipid is bigger than uncharged NPs and that they can also trigger membrane wrapping.[29] In addition, similar studies revealed that the membrane disruptive effect of cationic NPs increases with charge.[30] Studying interaction of NPs with artificial lipid bilayer assemblies has brought some light to this topic as well. It was found that both, positively and negatively charged NPs bind to lipids exerting changes in the bilayer. It was shown that the particles can bind either to N^+ or T^- terminus of lipids.[31] Moreover, cationic NPs were divided in three groups according to their disruptive effect of the lipid bilayers. Some NPs such as PAMAN G3-NH_2 dendrimers, tend to accumulate around a defect without creating new defects. NPs such as GNP-NH_2 diffuse across existing defects enhancing them. Finally, TAT sequence was found to create new holes and defects.[32] This different mechanisms of cellular uptake have also implications on the amount of NP's uptake and intracellular localization. For example, a study showed that cationic GNPs induce a 5-fold bigger uptake than their negatively charged counterpart. In addition, the authors showed that half of the cationic NPs diffuse across the CM creating holes and could be found in the cytoplasm while anionic particles were also found inside cellular endosomes.[33] Our group also found that positively charged TAT-modified GNPs could diffuse across the cell membrane directly to the cytosol and nucleus and the mitochondria.[34] Positively charge GNRs were also found to transduce more effectively inside Hela cells than negatively charged particles.[35] However, it was found that cationic NPs induce membrane depolarisation in several cell lines which increases the intracellular concentration of Ca^{2+}. This might result in modification of cellular pathways such as inhibition of proliferation or reduction of viability.[36] Finally, hydrophobicity is another parameter to take into consideration to understand cell uptake of NPs. Molecular dynamic simulations showed that while hydrophobic NPs are thermodynamically stable in the core of lipid bilayers, hydrophilic NPs have a higher affinity for the surface of the lipid bilayer.[37] Moreover, hydrophobic QDs were found to form hybrids with lipid of the bilayer being dispersed around the bilayer.[38] It is important to understand that NPs intended for biological applications need to be stable in physiological conditions which are hydrophilic. Therefore there is a need to find a compromise between hydrophobicity and hydrophilicity. Lipinski's rules of 5, also called Pfizer's rules of 5, predicted that molecules with drug-like properties (i.e. good solubility in physiological conditions are able to cross biological membranes), octanol-water partition coefficient log *P* should not be greater than 5.[39] Our group recently reported a work studying the interaction of amphiphilic GNPs with biological membranes acting as artificial ion channels.[40]

The interaction of NPs with biological components can interfere with cellular uptake. NPs used for biological studies are exposed to physiological environments such as blood and cell-culture medium. Biomolecules such as serum proteins are present in these environments at high concentrations. These proteins can be adsorbed on the surface of NPs forming a protein corona, changing the composition of NPs surface.[41] Since NPs are presented to cells through their surface, this protein layer could have a great importance in cellular-NPs interactions.[42] Lesniak *et al* showed the relevance of protein corona in silica NPs. Serum free incubation of this particles resulted in a higher cell uptake than when particles where incubated with serum proteins. They also showed that protein corona also affected to the cellular location of NPs. While complete medium resulted in entrapment of NPs in endosomes, some NPs were found free in the cytosol when serum free medium was used.[43] In addition, different variants of the protein corona such as composition (i.e. source of proteins and type of proteins), number of protein bounds and conformation influences the fate of NPs.[44,45]

4.1.3 Chapter Overview

The aim of cell labelling is to confer a distinctive contrast to our cells of interest in order to distinguish them from endogenous components using bioimaging techniques. In this chapter, cell labelling with the different probes described in chapter 2 and 3 is discussed. Selecting the most appropriate nanoparticle-ligand conjugates was the main aim here. The selection is based on the efficacy of nanoparticles as contrasts for the different imaging techniques employed in each case (see chapter 5). Cell uptake is one of the parameters studied to assess the effectivity of nanoparticles as potential probes. As mentioned in the introduction many factors affect the cell uptake of nanoparticles. In this chapter we will only focus on the differences that stem from the modification of surface of GNRs and ZGOs, because the other parameters such as size and shape were fixed to obtain the desired optical properties as seen in previous chapters. It must be noted that cell uptake, understood as number of nanoparticles inside the cell, is not the only parameter to take into account here. The highest uptake is not necessarily the best condition. We optimised our conditions to achieve the highest contrast or in other words the highest increase of a specific optical parameter, obviously, without affecting cell viability. Thus, it is crucial for us to assess the optical properties of labelled cells, better than the absolute amount of material (Au or ZGO) in cells. Hence, for GNRs, we focused on the conservation of optical properties of GNRs after cell uptake measured by vis-NIR spectroscopy, since PAI ultimately relies in the absorption of light by contrast agents. Whilst for ZGO the efficacy was assessed by measuring luminescence of labelled cells in the same instrument than preclinical imaging it has to be performed, i.e. in vivo imaging system (IVIS).

4.2 Experimental

Cell line: murine mesenchymal stem/stromal cell line MSCD1 (CRL-12424) cell line, were used for cell culture experiments. The cells were purchased from ATCC® and obtained from the bone marrow of *Mus musculus*, mouse.

Reagents: Dulbecco's Modified Eagle Medium (DMEM) was obtained from Gibco. Phosphate-buffered saline (PBS), penicillin−streptomycin and silver enhancer kit from Sigma Aldrich. Fetal bovine serum (FBS) was purchased from Life Technologies.

Protein corona and medium stability: PEG-COOH-GNRs and TAT-GNRs were incubated overnight with cell culture medium (DMEM supplemented with 10% FBS). Size of particles before and after incubation was determined by Dynamic Light Scattering (DLS) and optical properties by vis-NIR spectroscopy**.**

Cell labelling: In a typical experiment, 2×10^5 MSCs were seeded in 6-well plate with 2 mL cell culture medium (DMEM supplemented with 10% FBS) and incubated at 37°C with 5% CO_2 humidified atmosphere for 24hs. After 24 h, medium was replaced with 400 µL of NPs in 1.6 mL of fresh medium with 1% penicillin−streptomycin. For GNRs labelling, 400 µL PEG-COOH-GNR at an optical density (O.D) of LSPR band = 6 were mixed with 1.6 mL of fresh medium (i.e. final concentration in cell culture medium was 1.2 O.D). For ZGO labelling, 400 µL of 10 mg/mL DMSA-ZGO:Cr were mixed with culture medium (i.e. final concentration was 2 mg/mL). For dual labelling, a mixture of NP of PEG-COOH-GNRs at 24 OD and 10 mg/mL of DMSA-ZGO was used instead giving a final concentration in cell culture medium of 4.8 and 2 mg/mL respectively. Finally, cells were incubated with NPs for 24 h.

Silver enhancement staining: Cells were labelled as described above, but seeding 5× 10^4 MSCs cells in 24-well plates. After 24 hours incubation, cells were fixed with 4% para-formaldehyde (PFA) at room temperature. Cells were washed with PBS and dH_2O. 400 µL of a mixture prepared with equal volumes of the kit's two reagents were added in each well and left to 10 mins. Cells were washed with dH_2O before adding 400 µL of sodium thiosulfate (2.5% in aqueous solution) and washed several times with dH_2O. Finally cells were imaged using a Leica's light microscope.

Sample preparation for vis-NIR spectroscopy: After incubation with PEG-modified GNRs in 6-wells microplate, cells were washed several times with PBS and dissociated using trypsin. Cells were resuspended in fresh medium, washed twice with PBS by sequential centrifugations (500g for 3 mins), and number of cells was determined using an automated cell counter (TC10, BioRad). 9×10^5 cells were transferred to eppendorfs in PBS for vis-NIR measurements.

Persistent luminescence measurements: Persistent luminescent measurements were acquired using an IVIS spectrum system (PerkinElmer). 10^4 MSCs cells were seeded in 96 black well flat bottom plates and incubated for 24 hours. Dilutions of naked ZGO:Cr, DMSA-ZGO:Cr and TAT-ZGO:Cr were prepared to average emission intensity to 600,000 p/s (photons per second) in all samples as measured by IVIS. MSCs were incubated with 20 µL of ZGO with the different functionalities in 80 µL of fresh medium for 24 hours. Cells were washed several times with PBS. Excitation of particles was performed by exposing the plate to 2 BLS-series white BioLED light sources (3000K, 12W), purchased from Mightex, for 5 minutes. Persistent luminescence measurement were performed by open filter and acquisition time was set to 2 minutes. Each condition was prepared and measured in triplicates.

Preparation of cells for TEM: The samples were prepared for transmission electron microscopy (TEM) using the following protocol: after 24 h incubation, cells were fixed with a solution containing 1% paraformaldehyde and 3% glutaraldehyde in 0.1 M cacodylate buffer (pH 7.4). Then, cells were incubated with a reduced osmium staining solution, containing 2% OsO_4 and 1.5% $K_4[Fe(CN)_6]$, for 1 hour. This was followed by a second 1 hour osmium staining (2% OsO_4) step and overnight staining with 1% uranyl acetate. Cells were washed with water for 3 minutes, 3 times after every staining step. Samples were then dehydrated in graded ethanol (30%, 50%, 70%, 90% and 2x 100%) for 5 minutes each. Finally, samples were infiltrated with medium TAAB resin 812 and embedded within the same resin. The resin was cured for 48 h at 60°C. Finally, ultrathin sections of 350 µm x 350 µm x 74 nm were cut and placed in 200-mesh Formvar/Carbon filmed grids. They were post-stained with uranyl acetate (4% UA in a 50:50 ethanol/water solution) and Reynolds lead citrate before TEM imaging.

Cell Imaging: Cell were imaged using a Tecnai G3 spirit TEM at 120 keV, For cryo TEM, cells were labelled on a TEM grid and placed inside an FEI Vitrobot Mk2 vitrification system at 8 °C. The samples were blotted twice before being plunged into liquid ethane. Environmental scanning electron microscopy (ESEM) was performed in a FEI Quanta 250 FEG scanning electron microscope.

Cell viability (ATP assay): Cell viability was assessed with Cell Titer Glo ATP Assay (Promega). Cells were labelled as described above, but seeding 10^4 MSCs cells in 96-well plates. Cells were incubated with 0, 0.1, 0.5, 1, 3, 5 mg/mL ZGO:Cr in medium, for assessing toxicity of dual labelling cells were incubated with 2mg/mL DMSA-ZGO, 1 nM (4.8 O.D in cell medium Approx.) PEG-COOH-GNRs and a mixture of both NPs at the same concentrations (80% medium and 20% NPs solution in each case) for 24 h. After labelling, cells were washed 3 times with PBS. 50 μL of medium were added to each well and then 25 μL of the ATP reagent was added. The plate was mixed in an orbital shaker and, after 10 minutes, the contents of the plate were transferred to white, opaque, 96-well plates and the luminescence measured with a plate reader (Fluostar Omega, BMG Labtech). Each condition was assessed in triplicate and results are given as % ± SD in respect to cells that were incubated with no GNRs.

Notes about concentrations of nanoparticles

Concentration of nanoparticles is expressed in many different ways in the literature depending on the type of nanoparticles, application, or author’s preferences. Some times this can make the comparison between types of nanoparticles or between different works difficult. To facilitate comprehension to the reader of this thesis, we include here a table with approximate equivalences. Note that we normally expressed GNR concentration as O.D. of the LSPR peak because they were going to be used as probes for optical imaging and it is the best way to minimize the slight variations between batches. ZGO concentrations are normally given in mg/mL because it is the most usual way in the literature for these NPs.

For the calculations we used absorbance at 400 nm of GNRs to obtain atomic Au concentration[46] and the size of nanoparticles to obtain the theoretical weight of a nanoparticle (m=d×V).

LSPR peak (O.D.)	A_{400}	atomic Au (mM)	mg Au/mL	GNR/mL	GNR (pM)
0.1	0.03	0.01	2.79×10^{-6}	1.35×10^{10}	22.38
1	0.34	0.14	2.79×10^{-5}	1.35×10^{11}	223.80
2.4	0.82	0.34	6.70×10^{-5}	3.24×10^{11}	537.11
3.6	1.22	0.51	1.00×10^{-4}	4.85×10^{11}	805.67
4.8	1.63	0.68	1.34×10^{-4}	6.47×10^{11}	1074.22

Table 4.1: Calculations of GNRs concentrations.

mg ZGO:Cr/mL	NP/mL	NP (µM)
0.5	6.37×10^{14}	1.06
1	1.27×10^{15}	2.11
1.5	1.91×10^{15}	3.17
2	2.55×10^{15}	4.23
2.5	3.18×10^{15}	5.28

Table 4.2: Calculations of ZGO:Cr NPs concentrations.

4.3 Labelling cells with GNRs

As seen in section 2.1, the use of surfactants such as CTAB in GNRs synthesis is crucial for the synthesis of anisotropic nanoparticles. However, CTAB is a cytotoxic surfactant at the concentration used in the synthesis (100 mM)[47,48,35]. As table 4.1 shows, CTAB cytotoxicity is dose dependant. Concentrations above 20 µM resulted in cell death when incubated for 24 hours with murine mesenchymal stem/stromal cell line (MSCs). It was also found that at this range of concentrations, the quantity of CTAB is too low to guarantee the colloidal stability of GNRs and the particle tend to aggregate in cell culture medium. Therefore, it is clear with those results that surface of GNRs had to be modified to avoid toxicity. Different strategies have been discussed in chapter 2; in this section we will focus on the interaction with cells of the 2 types of PEG explained in chapter 2. Note that PEG is a biocompatible molecule widely use in pharmaceutical products (such as the stabilizer Carboxwax®) and as capping agent/surfactant for a range of nanoparticles.[49]

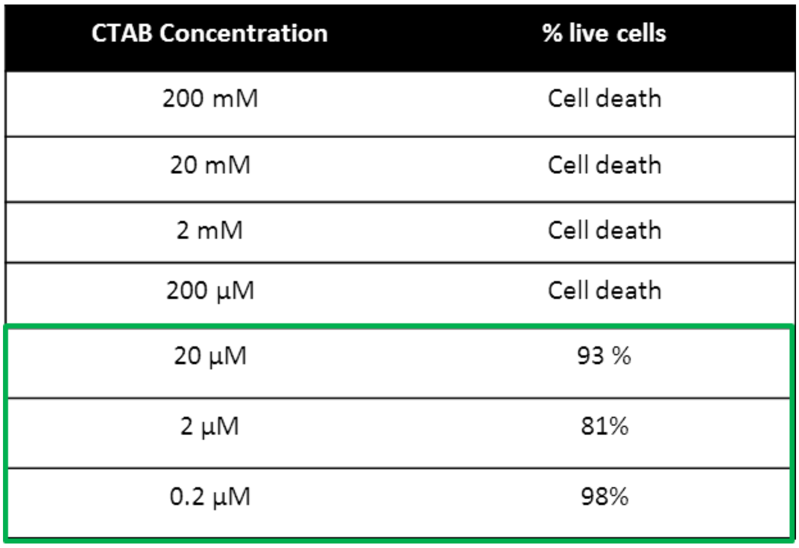

CTAB Concentration	% live cells
200 mM	Cell death
20 mM	Cell death
2 mM	Cell death
200 µM	Cell death
20 µM	93 %
2 µM	81%
0.2 µM	98%

Table 4.3: Cell viability by trypan blue test after 24 hours incubation of MSCD1 with different concentration of CTAB in solution.

4.3.1 SH-PEG 5000 Vs. SH-PEG-COOH: protein corona formation and its implications on cell uptake.

4.3.1.1 Incubation of SH-PEG-5000 with stromal-mesenchymal cells

In our first approach SH-PEG-5000 was used as capping agent. GNRs functionalised with SH-PEG-5000 as explained in section 2.4.1 were incubated with MSCs for 24 hours. Presence of GNRs in cells was screened with optical microscopy. To facilitate their visualisation, contrast of GNPs was improved by using a silver enhancer which uses colloidal gold as a nucleation core, leading to a higher contrast, which enables visualisation of GNPs with an optical microscope.[50] Black stains in the area of the cells is an indication of GNPs inside cells. However, other techniques such as electron microscopy would be needed for conclusive results. CALNN-capped GNPs were incubated simultaneously as a positive control of cell uptake. Figure 4.2 shows the optical microscopy pictures of labelled cells before and after silver enhancement. Cells incubated with CALNN-capped GNPs showed a great amount of black stains after silver enhancer, indicating a relevant internalisation of NPs. On the other hand, no significant uptake was observed with PEGylated GNRs. Nonetheless, cell death and aggregation problems observed with CTAB were overcome using PEG as a capping agent.

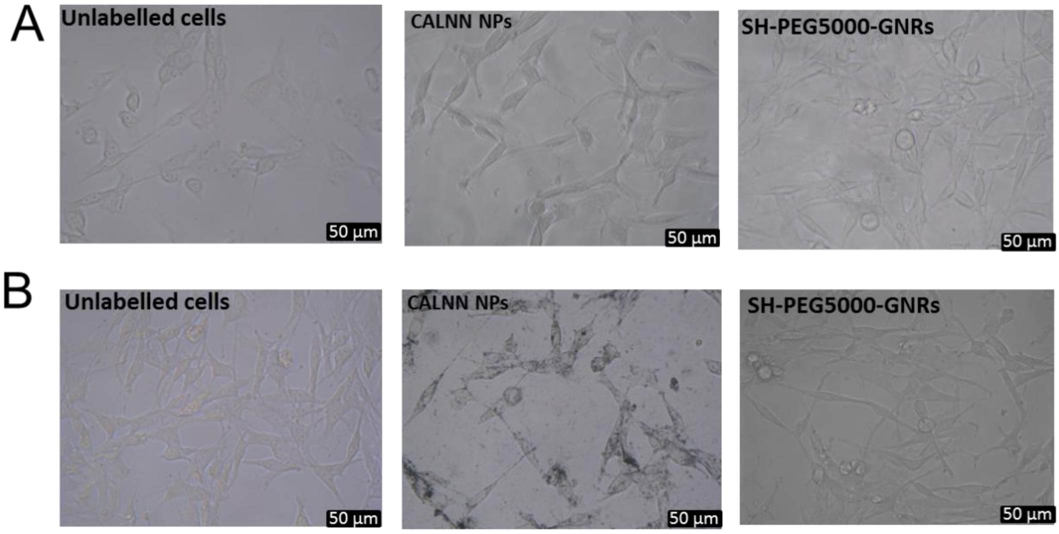

Figure 4.2: Optical microscopy picture of unlabelled cells, CALNN NPs and SH-PEG-5000 labelled cells before (A) and after (B) silver enhancement. This preliminary experiment shows that SH-PEG-5000 did not elicit any major effect on cell viability, but no uptake was observed. CALNN NPs was used here as a positive control of uptake.

4.3.1.2 Incubation of SH-PEG-COOH with stromal-mesenchymal cells

Optical microscopy studies indicated that GNR-SH-PEG-5000 did not show a significant cell uptake, or at least, it was shown to be much lower than CALNN NPs suggesting that PEG 5000 is not a good candidate for our final application. This is in agreement with other works.[51] This effect on cell uptake has been proposed to be achieved by avoiding or reducing protein adsorption due to the “brush” conformation that PEG particles adopt in solution.[52] This fact has been related to a lower uptake by immune cells (often described as a stealth effect) observed for nanoparticles capped with this type of PEG.[53] We therefore, started working with a short (523 Da) carboxyl-terminated PEG (SH-PEG-COOH). Briefly, this new PEG provides a thiol group, which has high affinity to gold surface; a short hydrocarbon chain to improve ligand packing; and finally a carboxylic group which is deprotonated at physiological pH, providing negative charge and therefore electrostatic stability (see chapter 3.4.2 for details on the conjugation). In this section, some of the results obtained by labelling stem cells with GNRs modified with SH-PEG-COOH will be discussed. Further results are shown in the next sections as well.

MSCs were incubated with SH-PEG-COOH-GNRs for 24 hours and imaged by optical microscopy. Black stains in cells were easily spotted for this condition even with no need to use silver enhancement, thus indicating presence of gold in cells. (Figure 4.3 A). It was observed that those stains followed a circular pattern around the central part of the cells. These types of patterns are indicative of the accumulation of nanoparticles around the nucleus after their uptake. [54] All in all, this supports the hypothesis that contrarily to SH-PEG-5000, this smaller PEG induced uptake of GNRs by MSCs. We believe that the different interaction with proteins from the serum might explain why these GNRs were uptaken by cells. To study these interactions, we incubated GNR-SH-PEG-COOH in cell medium supplemented with serum and measured changes on their hydrodynamic diameter by Dynamic light scattering (DLS) (figure 4.3 C). A shift to larger diameters was observed after incubation. This increase in the hydrodynamic diameter can only be explained with the recruitment of proteins on the particle surface, since the nanorods did not experience any degree of aggregation as demonstrated by the maintenance of their optical properties (Figure 4.2 D). This is therefore very likely attributed to unspecific adsorption of proteins from the medium. As mentioned in chapter 2, this is a well-known process affecting many different types of nanoparticles in biological medium, often known as protein corona. [55] It must be noted here that DLS is unable to provide the actual values of the increase in the hydrodynamic diameter of GNRs. As we mention in previous chapters, anisotropy of GNRs resulted in two components of Brownian motion, which is translated in two peaks in DLS data. Therefore more than the absolute values, the important information here is the observed shift to larger diameters and the conservation of the anisotropy, which agrees with the adsorption of proteins and absence of aggregation.

In order to further study our system, SH-PEG-COOH GNRs were incubated in a serum free medium (i.e. cell medium without proteins). In the absence of proteins, optical microscopy pictures showed big aggregates of particles around the cells but no black contrast was observed around the central part of cells (Figure 4.3 B). This data suggests that serum proteins in medium plays an important role on the stability of GNRs, and consequently on their interactions with cells. Although PEG-COOH GNRs were stable under physiological pH (Figure 2.4 A in chapter 2), the high ionic strength of cell culture medium is likely to be the reason of their aggregation. Therefore, spontaneous adsorption of serum proteins not only protects SH-PEG-COOH-GNRs from aggregation in cell culture medium, but they also are very likely to favour their uptake. Charge provided by COO^- seems to quench the shielding effect observed in large PEGs. It has been reported that the charged counterpart of PEG have a greater affinity toward proteins and therefore a higher cell uptake.[56] With all this information, PEG-COOH was selected as a better candidate for our purposes. Uptake of these GNRs and their bioconjugates are studied in greater detail in the next sections.

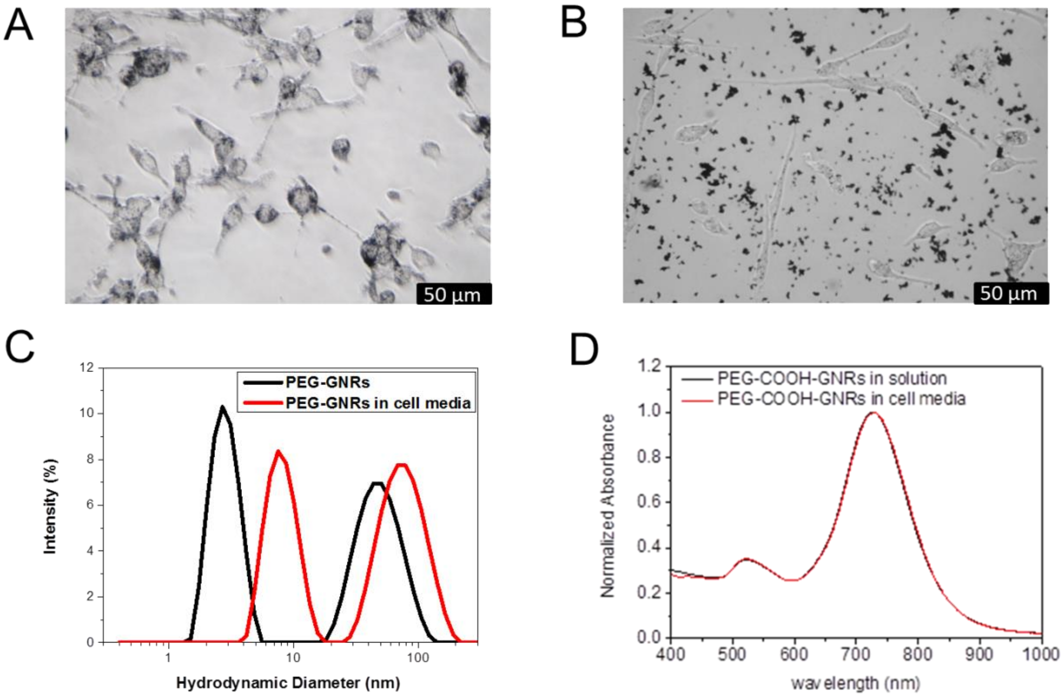

Figure 4.3: Cell uptake of GNRs modified with PEG-COOH. Figure A) Optical microscopy pictures (40 x magnification) of MSCD1 cells incubated GNRs with serum (A) and without serum (B) C) vis-NIR spectra of PEG-COOH modified GNRs in HEPES (in black) and after 24hs incubation with cell medium (in red). D) Normalized vis-NIR spectroscopy of PEG_COOH-GNRs before and after incubation in cell medium.

4.3.1.3 Uptake of SH-PEG-COOH-GNRs and the effect on the optical properties of labelled-cells.

As mentioned before in this chapter, Photoacoustic Imaging (PAI) deeply relies on the ability of probes to absorb light, rather than on gold content inside the cells (See chapter 5). Therefore, it is important to study vis-NIR spectrum of labelled cells since confinement of GNRs inside vesicles in cells (e.g. endosomes) can alter their optical properties due to agglomeration and/or plasmon coupling. After incubation of cells with GNRs, the resulting labelled cells were trypsinized and vis-NIR spectroscopy conducted (Figure 4.4). It was observed a significant gain in the 700-900 nm region of the spectrum, which is the region used in PAI. It was also observed a broadening and a decrease in intensity of the LSPR absorbance, compared to the one corresponding to the same GNRs in solution This phenomenon is symptomatic of GNRs agglomeration inside the cell [57]. When the labelled cells were lysed by ultrasounds, the intensity and shape of the LSPR was completely recovered (figure 4.4 in blue). This proved that it is an agglomeration rather than sintering. The broadening of the LSPR is ascribable to the well-known plasmon coupling effect [58]. When particles are confined in a small volume, the electric field of a particle disturbs the neighbouring particles fields which leads to an alteration of the optical properties [59]. This is the precise scenario when particles are uptaken by cells via endocytosis and packed in the endosomes. GNRs only retrieve their stability and resulting optical properties when they are released from this confinement after cell lysis. Despite an evident broadening and loss of intensity of the LSPR band, there is still a clear increase in the absorbance at 700-900 nm, which made this strategy suitable for PAI of cells. Obviously avoiding plasmon coupling and/or agglomeration in endosomes, would result in higher sensitivity. In this regard, we have observed that co-incubation of GNR-SH-PEG-COOH with ZGO have a huge impact in avoiding this phenomena (see details in section 4.5.1). Also, in a parallel work we have developed a strategy to minimise plasmon coupling in cells by coating GNRs with a 35 nm silica shell.[60]

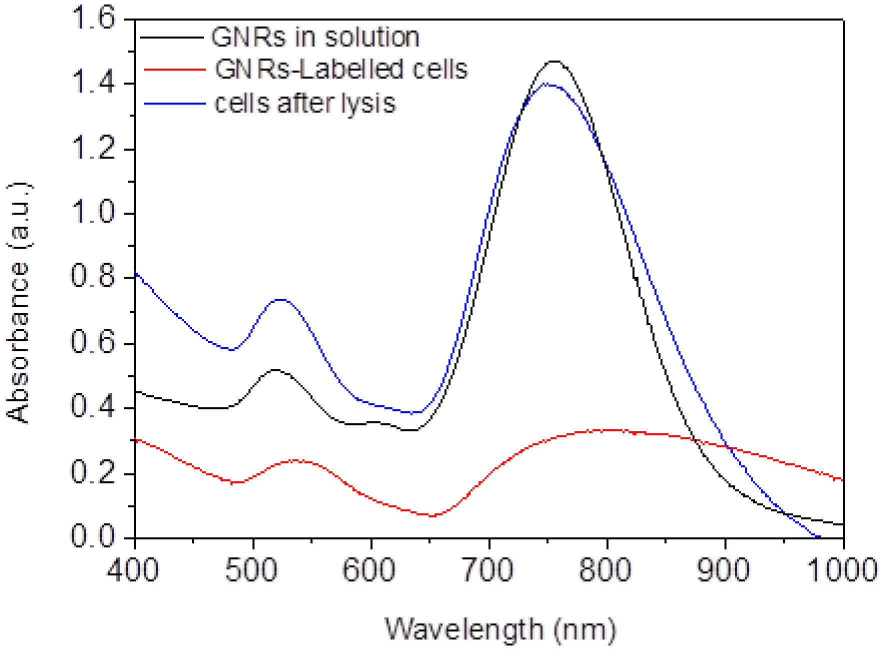

Figure 4.4: Optical properties of PEG-COOH-GNRs-labelled cells. vis-NIR spectra of PEG_COOH_GNRs in solution (black), GNRs- labelled cells (red) and labelled cells after lysis by ultrasounds (blue).

4.3.1.4 Electronic microscopy imaging of cells labelled with SH-PEG-COOH-GNRs

Optical microscopy and vis-NIR spectroscopy of labelled cells provided information indicating that GNRs modified with SH-PEG-COOH were transported inside the cell. However, electron microscopy imaging is still needed to confirm uptake and localize GNRs inside the cell. A battery of electron microscopy techniques were used here for imaging labelled cells after 24 hours incubation. Transmission electron microscopy (TEM), Cryo-TEM and environmental scanning electron microscopy (ESEM) were selected here as complementary techniques to image labelled cells. TEM (Figure 4.5) is one of the most widely used techniques due to its high resolution, which can be down to 0.1 nm. Due to the possibility to image not only NPs but also subcellular structures, allows discriminating the mechanism of uptake (e.g. endocytosis) and also the assessment of signs indicative of cytotoxicity such as apoptotic vesicles. However, the sample preparation is time consuming so high throughput of samples is not possible. Sample preparation and staining may lead to shrinking problems changing the physiognomy of cells[61-62]. For this reason a cryogenic approach (Figure 4.6), where fixation process is avoided, provides complementary information about the cell in more similar conditions to the standard hydration level while still being able to image cellular organelles[63]. In addition, ESEM (Figure 4.7) allows the possibility to control the humidity levels of samples during the imaging. This permits the imaging of hydrated cells, i.e. in similar conditions to the cells culture. However, contrast is not good enough to see details at the subcellular level.

All in all these techniques allowed the imaging of individual particles and provided with complementary information about the localisation of GNRs and physiognomy of cells after different treatments. From the images obtained with the three techniques, it is consistent that GNRs form mainly clusters inside the cells. Moreover, from the TEM and cryo-TEM images, it is observed that GNRs are closely packed in cell vesicles, most likely endosomes. This indicates that PEG-GNRs are transported across the cell membrane via endocytosis. In some vesicles of the cell, it seems that gold cores are even being fused. This is consistent with data obtained with the vis-NIR spectroscopy which showed a broadening of the LSPR due to agglomeration of NPs and plasmon coupling.

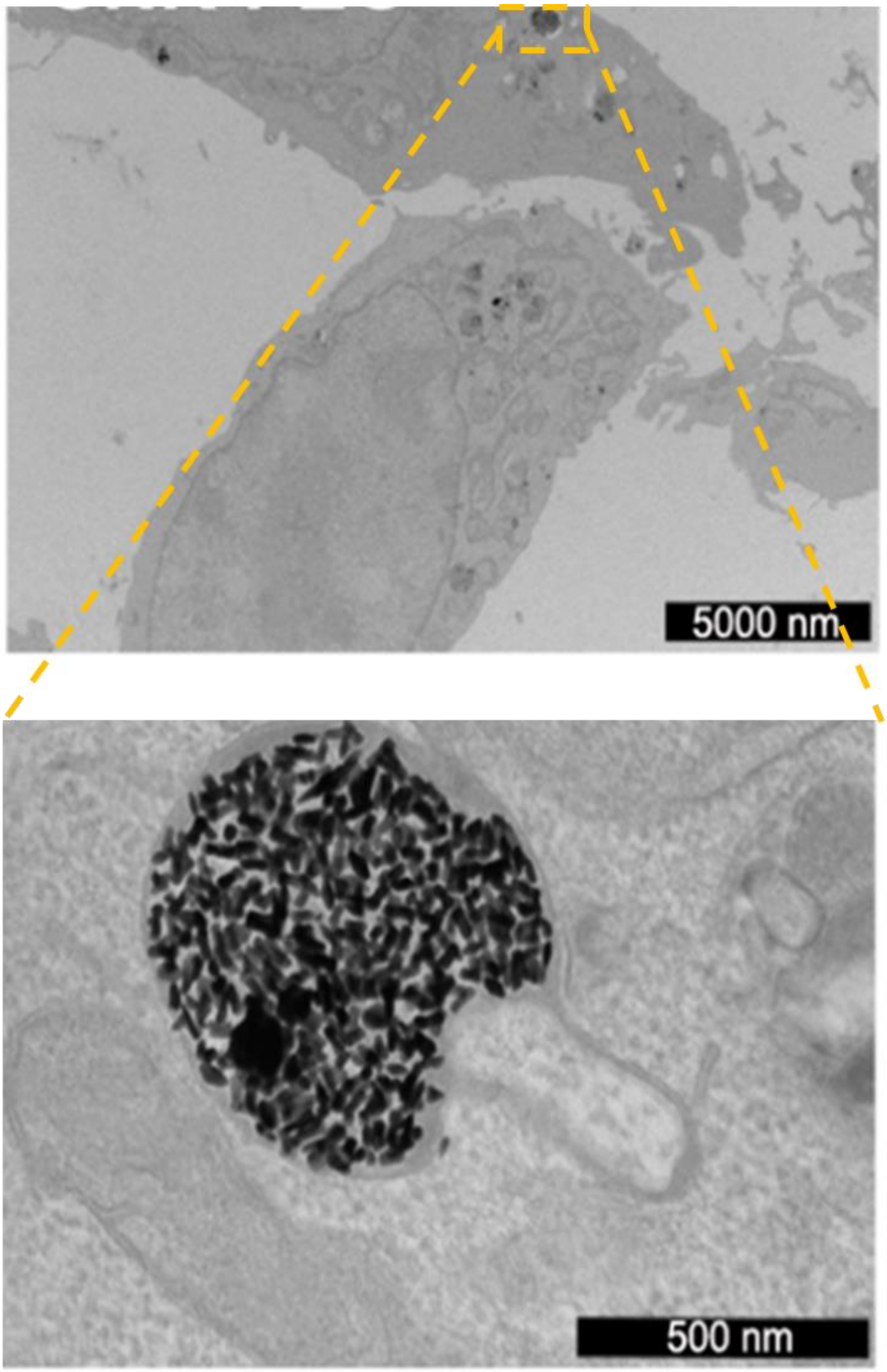

Figure 4.5: **TEM imaging of MSCs labelled with PEG-COOH-GNRs.**

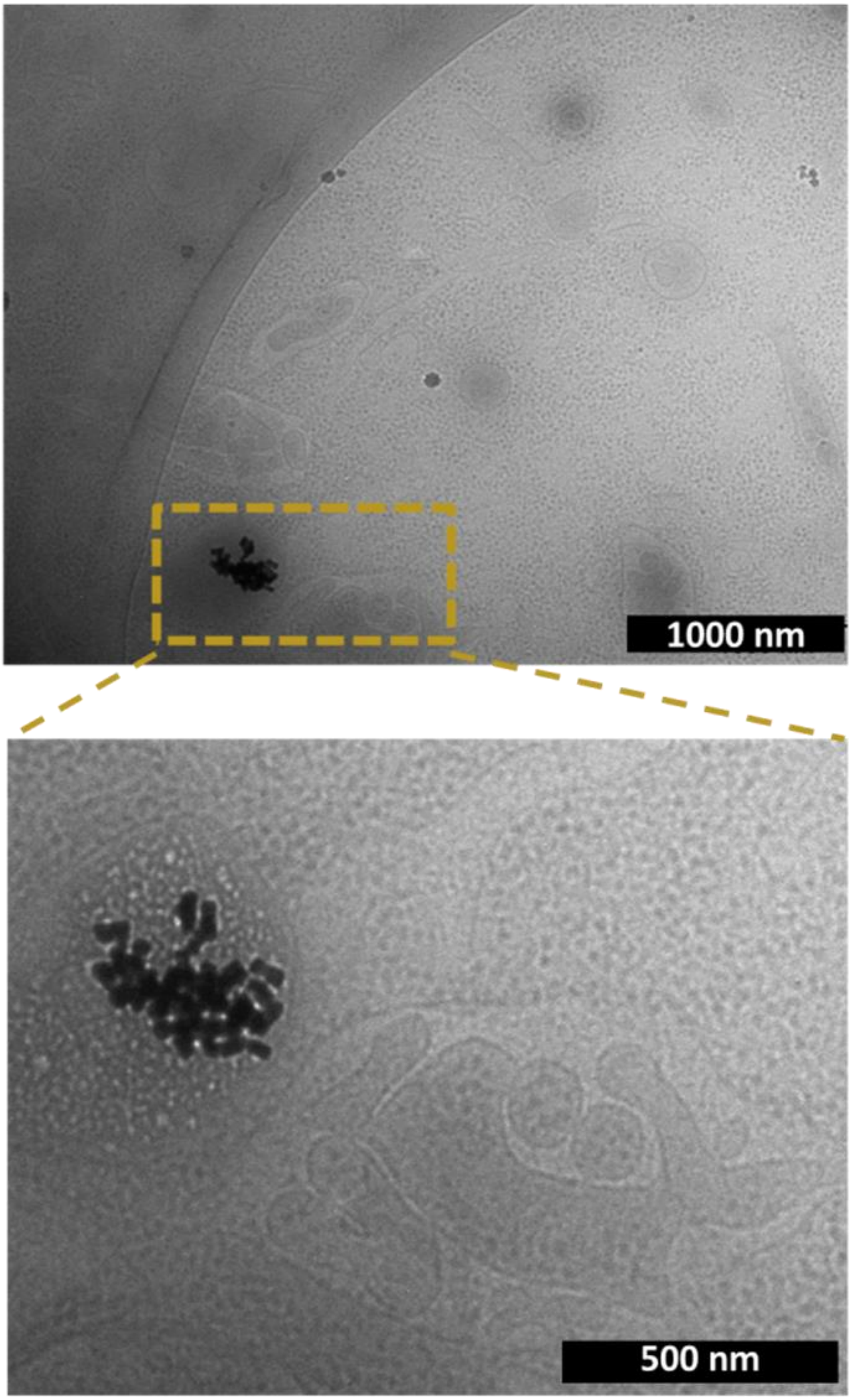

Figure 4.6: Cryo-TEM imaging of MSCs labelled with PEG-COOH-GNRs.

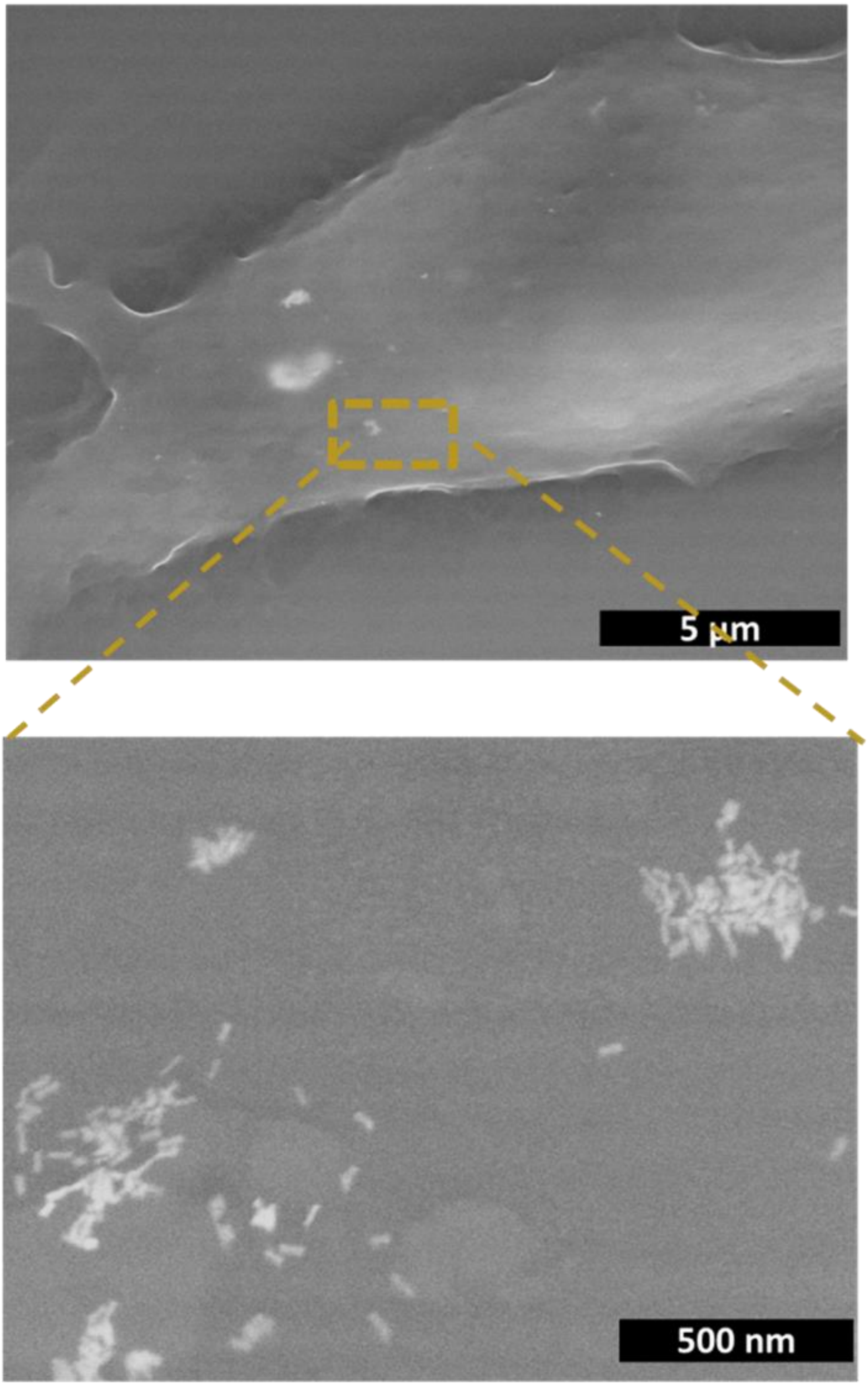

Figure 4.7: ESEM imaging of MSCs labelled with PEG-COOH-GNRs.

4.3.2 SH-PEG-COOH modified GNRs and its bioconjugates derivatives

SH-PEG-COOH is a promising ligand for labelling cells with GNRs as results discussed in the previous section suggests that they are stable under physiological conditions and they can be transported through the cell membrane. This ligand can also be used as scaffolds to bind biomolecules as it was discussed in section 2.5 of chapter 2. This offers many possibilities such as attachment of drugs for drug delivery or building complex structures with other active NPs to form bimodal probes (section 3.6 in Chapter 3). Figure 4.8 summarizes the conjugation approach. In this section, we focus on the relevant biological differences between PEG-GNRs and its covalent bio-conjugates.

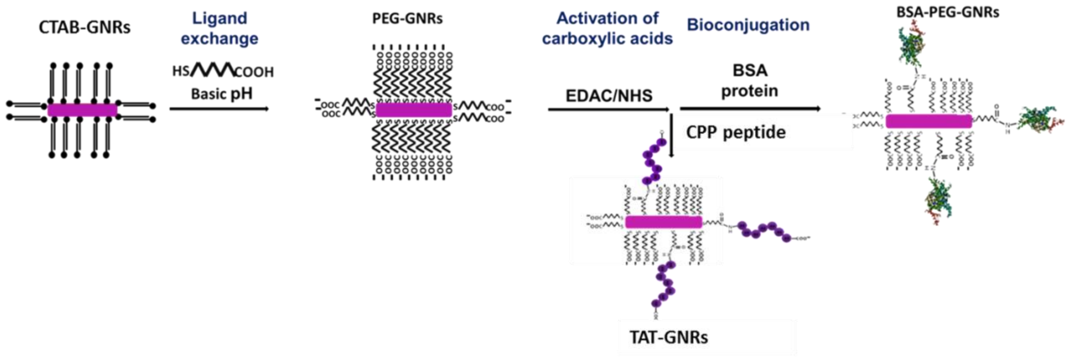

Figure 4.8: Diagram summering the bio-conjugation of GNRs with CPP and BSA.

Bovine Serum Albumin (BSA) protein and transactivator of transcription (TAT) peptide were selected for being bound to GNRs (See sections 2.5.2 and 2.5.3 respectively). We selected these biomolecules due to its biological relevance. BSA is the most predominant protein in cell culture medium. Our aim here was to study the differences in cell uptake between a spontaneous protein corona formed *in situ* in the cell culture dish and a covalently bound BSA to GNRs. In addition, as mentioned in chapter 2, TAT (GRKKRRQRRRPQ) was the first discovered Cell Penetrating Peptide (CPP). It is the basic domain of HIV TAT protein and a polycationic arginine-rich peptide. The first NP conjugated with TAT was presented by Josephson *et al* in 1999.[64] It was shown that there was a 100-fold enhancement of cellular delivery when superparamagnetic NPs were conjugated with TAT. [64] It has been debated that TAT can traduce into cells in a receptor-independent manner. This was supported by the observation that small Antp peptides (RQIKIWFQNRRMKWKK), which is the third helix of Antennapedia homeodomain, can cross cell membranes at 4 °C[65], indicating that receptors do not have a role in the mechanism and therefore all cell type could benefit from the observed enhanced cell uptake triggered by the peptide. However, the cell uptake mechanism has not yet been completely elucidated.

In order to assess stability, PEG and TAT modified GNRs were incubated in complete cell medium for 24 hours before GNRs were purified by centrifugation. Zeta potential measurements (Figure 4.9 A) showed that TAT and PEG modified NPs had very different surface charge in aqueous solution. The deprotonated carboxylic acids on the surface of the particles make an average negative charge while TAT is a peptide rich in positively charged aminoacids. However, the final surface charge after incubation of both particles in cell medium was virtually the same, even when particles were purified. Proteins in medium have an average negative charge. Therefore, these results show that proteins covered the surface of both particles, leading to the same final average surface charge.

On the other hand, hydrodynamic diameter distribution curves obtained after incubation of the particles in cell culture medium showed differences when the two conditions were compared. PEG-COOH-GNRs retained colloidal stability since only a shift of a few nanometres and two peaks were always observed (Figure 4.3 C). This also revealed that proteins do not lose their native conformation as denaturalized protein would precipitate and form big aggregates. TAT modified GNRs posed a different scenario; shift in the hydrodynamic diameter was not only bigger after incubation with cell culture medium, but big structures close to 10000 nm were observed (Figure 4.9 B). In addition, the two peaks in the diameter distribution graph, distinctive of anisotropic particles, were starting to be lost. Alike PEG-GNRs, surfaces modified with TAT triggers the formation of big particle aggregates as measured by the DLS. Most likely this was due to the denaturalization of serum protein which led to a crosslinking of GNRs.[66,67] vis-NIR spectroscopy of the different GNRs is consistent with the latter results. No changes in the optical properties were observed when PEG-COOH-GNRs were incubated under physiological conditions (Figure 2.3 D), proving their remarkable colloidal stability. On the contrary, vis-NIR spectrum of TAT-GNRs after incubation showed a broadening of the LSPR. In addition, the increase in optical density at long wavelengths indicated an increase of the scattering component in the optical spectrum, which is related to the presence of bigger particles. This confirmed the aggregation of GNRs functionalised with TAT when exposed to cell medium.

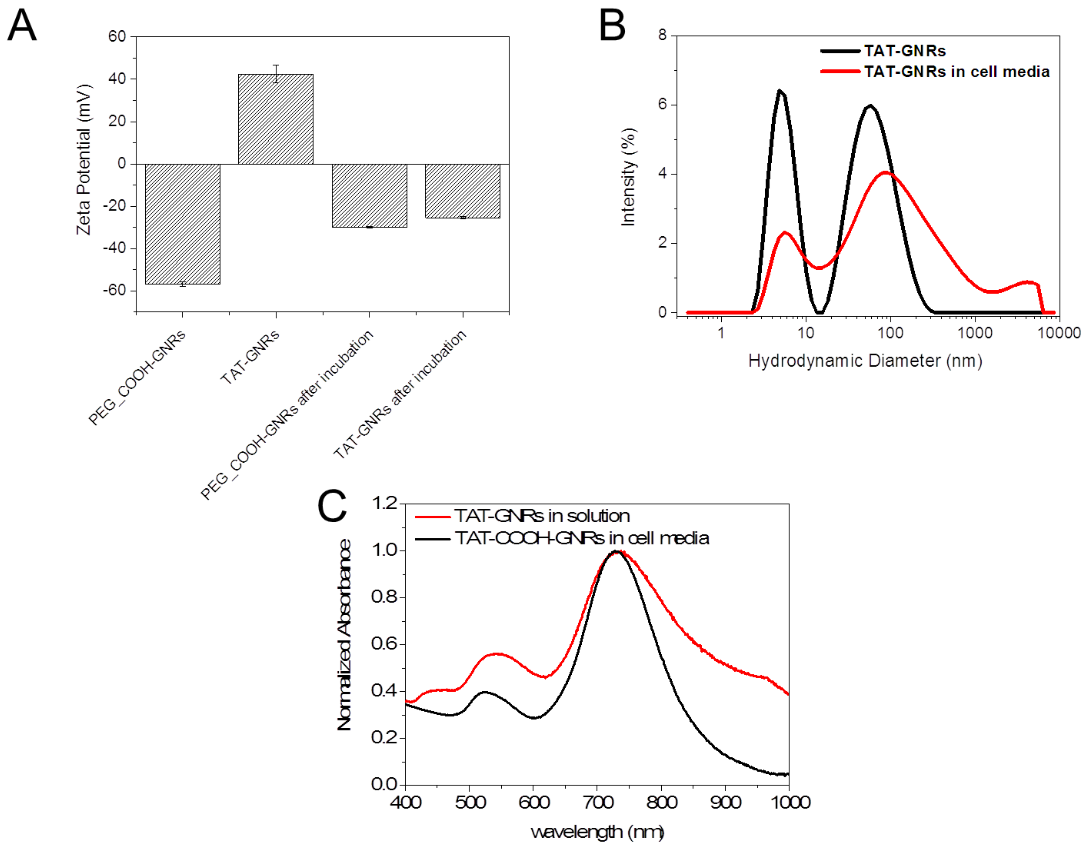

Figure 4.9: Stability of TAT-GNRs and PEG-COOH-GNRs in complete cell culture medium. A) Zeta potential of GNRs before and after incubation in cell culture medium. B) Hydrodynamic diameter measured by DLS of TAT-GNRs before and after incubation. C) Normalized vis-NIR spectroscopy of PEG_COOH-GNRs before and after incubation in cell medium.

Figure 4.10 shows the spectrum obtained after labelling MSC with PEG-GNRs and its two different bioconjugates after a subsequent washing of the treated cells. All samples tested showed a broadening in the LSPR, which is a “symptom” of plasmon coupling. This might indicate that all the different surfaces triggered cell uptake through endocytosis and particles were tightened inside cell vesicles. However, differences in the shape of plasmons and in area under the curves (AUC) are observed in the graph. The type of binding of proteins to GNRs had an effect on the cell uptake of particles. Area under the spectrum of PEG modified GNRs was bigger than in the covalent protein corona one. This indicated a bigger uptake when PC was formed *in situ* in the dish. It is difficult to predict what was causing this difference since many variables have to be taken into consideration when working with cells. Only BSA was available on the surface of covalent protein corona while there was a big range of proteins in the serum used in cell culture. Different protein composition on the surface of particles could create a different response. It is also possible that when the amide bond is formed between an amine of the protein and the carboxylic acid, BSA could suffer a small change of conformation, which could lead to a lower affinity toward the Gp60 receptors (serum albumin receptor) on cell membrane.[45] On the contrary, as it was expected from the vast literature on TAT conjugated NPs, TAT-GNRs showed an increase in AUC when vis-NIR of labelled cells was measured. This indicates an enhancement of cell uptake when compared to PEG-COOH-GNRs. However, broadening of LSPR is more prominent with these particles. As it was shown in figure 4.9, TAT-GNRs showed a lower colloidal stability under physiological conditions than PEG-COOH-GNRs which had an impact on optical properties of labelled cells. Here we measured the vis-NIR spectra of labelled cells because we were interested in the optical properties of GNRs and how they change after cellular uptake. Amount of gold inside the cell can be measured more accurately by inductively coupled plasma mass spectrometry ICP-MS.

C. Fleischer *et al*[68] showed that positively charged polystyrene NPs triggered the denaturalisation of BSA while negatively charged NPs were able to retain the native structure. They demonstrated by binding assays, that the secondary structure of the protein corona regulated the binding to different membrane receptor. They speculated this is the reason for the difference observed in cell uptake. This unfolding of proteins triggered by positive charges could be the explanation for the bigger shift observed with TAT modified GNRs after incubation with cell-culture medium (Figure 4.9). To recapitulate, it seems that the protein structure of the proteins adsorbed or deliberately attached to NPs have a repercussion on cellular uptake. While unfolded proteins could have an enhance effect (TAT-GNRs), small changes of conformation (covalent PC) could have the opposite effect.[45]

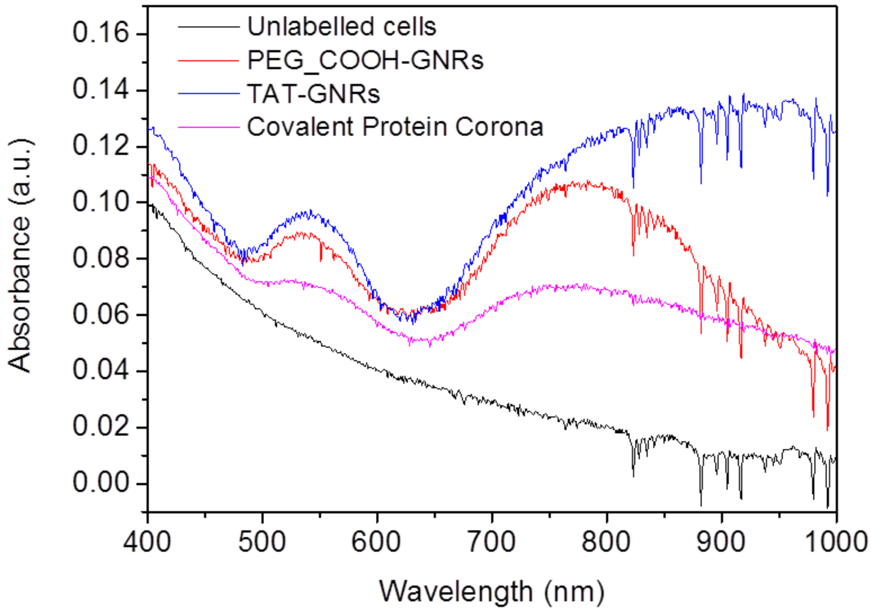

Figure 4.10: Optical properties MSCs labelled with different bioconjugated GNRs. vis-NIR spectroscopy of labelled cells with PEG_COOH, TAT and covalent BSA capped GNRs.

To summarize, optical microscopy showed that PEG-COOH was a better ligand than PEG 5000 in terms of cell uptake, since no internalisation of particles were observed with the latter ligand. In addition, although TAT was shown to improve cell uptake, stability problems in cell medium led to a change in the optical properties of labelled cells due to agglomeration and plasmon coupling. Therefore, we selected SH-PEG-GNRs as the most promising probes to continue to the *in vivo* experiments.

4.4 Labelling cells with ZGO

Results regarding the labelling of MSCs with Chromium-Doped Zinc Gallium Oxide (ZGO) Nanoparticles are presented in this section. Synthesis, surface modification and characterisation of this material are fully discussed in chapter 3. From the library of ligands created in section 3.5, DMSA and TAT modified ZGOs were selected for the *in vitro* studies due to their superior colloidal stability along with the stability of the binding form between ZGO surface and DMSA. Briefly, DMSA forms a coordination bound with heavy metals, in this case Zn. Then, TAT peptide was bound in a covalent manner via condensation reaction. See section 3.5 for details in the conjugation of ZGO. The performance of the different surfaces was assessed by means of IVIS signal and compared with “naked” ZGO.

4.4.1 “Naked” ZGO Labelling

Unlike GNRs, as synthesized ZGO did not elicit any major cytotoxicity. Moreover, cell viability assays showed that cell survival is over 92% even at a concentration of 5 mg/mL of ZGO (Figure 4.11 C). In addition, MSCs were incubated for 24 hours with unmodified and IVIS signal of the resulting labelled was measured. Results obtained by IVIS showed that cells labelled with ZGO concentrations as low as 0.5 mg/mL are detectable. However, total flux, defined as photons per second, increases linearly only after incubations with higher concentrations than 1 mg/mL. Therefore, the aim for surface modification here was improving cell uptake of naked particles at the same time that colloidal stability in physiological conditions was maintained.

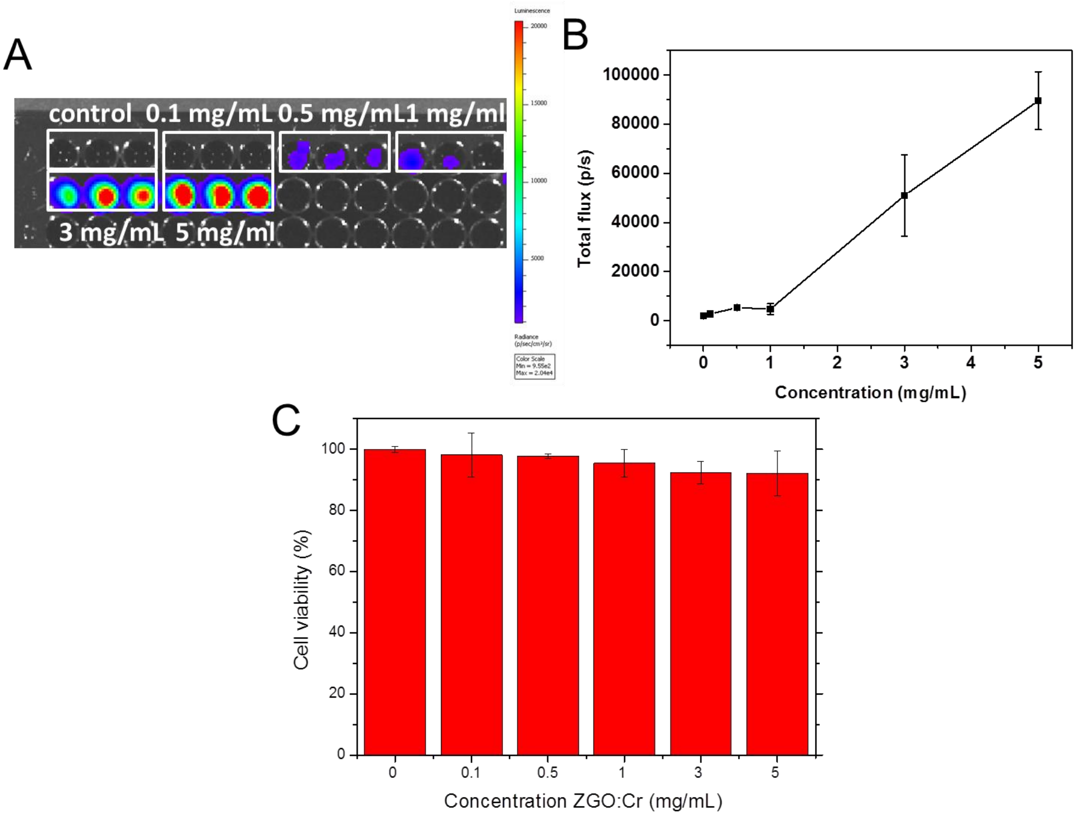

Figure 4.11: Incubation of MSCs with ZGO:Cr. A) Luminescence images shown in radiance, i.e. photons per second per square centimetre per steradian (p/s/cm2 /sr)] of ZGO-labelled MSCs at different concentration after white light excitation for 5 min. B) Total flux recorded with labelled cells. Error bars are the standard deviation of the average over 3 replicates. C) MSCs cell viability after 24 hr of incubation with ZGO:Cr. Error bars are the standard deviation of the average over 3 replicates.

4.4.2 Naked ZGO Vs. DMSA-ZGO Vs. TAT-ZGO

In order to select the most appropriate surface functionality between non-functionalized particles, DMSA-ZGO and TAT-ZGO, we studied the luminescence intensities of labelled cells after 24 hours incubation. The optical signal was normalized to photons per second also expressed as total flux. For this, dilutions of the different particles were prepared so all samples were emitting at the same intensity in total flux (600,000 p/s) before incubation with cells. Note that different concentrations were needed to achieve the same number of photons per second (Table 4.2). IVIS measurements of cells seeded directly in a well-plate, showed a big variance between the different functionalities used (Figure 4.12). While cells labelled with non-functionalized NPs showed luminescence intensity similar to unlabelled cells, TAT NPs presented a remarkable intensity. These results indicate that TAT NPs underwent a much higher cellular uptake than uncoated NPs and DMSA-NPs. Conversely to GNRs, ZGO optical properties are not inhibited by proximity of neighbouring NPs. Therefore, in this case a higher cell uptake is always synonym of better optical properties. However, TAT labelling showed a poorer reproducibility when compared to results obtained with DMSA-ZGO. The higher level of aggregation in cell medium observed with TAT NPs (not only ZGO but also GNRs) could be the cause for this. The formation of these aggregates could also be one of the reasons causing this remarkable cellular uptake along with the cell penetrating properties of TAT peptide. As mentioned in the introduction, it was reported that for some systems, aggregates could enhance cellular uptake.

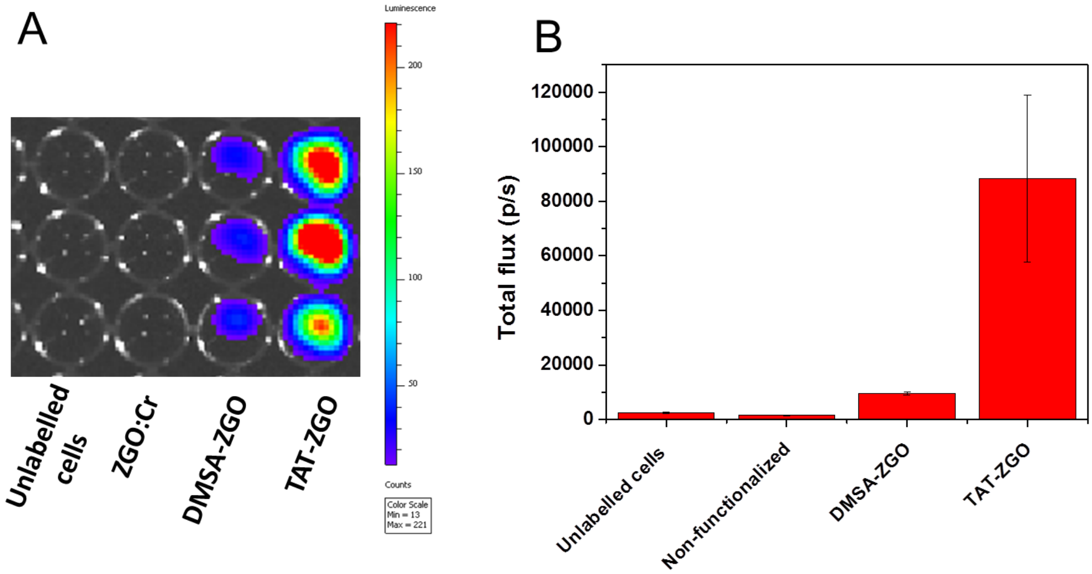

Figure 4.12: Cell uptake of ZGO:Cr, DMSA-ZGO and TAT-ZGO A) Luminescence image of ZGO:Cr, DMSA-ZGO and TAT-ZGO- labelled cells B) intensities (expressed in p/s) of MSCs labelled with ZGO:Cr, DMSA-ZGO and TAT-ZGO. Error bars are the standard deviation of the average over 3 replicates.

Functionality	Concentration	Total flux of ZGO in solution (p/s)	Total flux of labelled cells (p/s)
Non-functionalized	1.8 mg/mL	600000	1464
DMSA-ZGO	0.3 mg/mL	600000	9597
TAT-ZGO	1.7 mg/mL	600000	88237

Table 4.4: Actual concentration of NPs used in figure 4.11 and the intensity shown in total flux (p/s).

Interestingly, when luminescence intensities of labelled cells are related with the actual concentration of NPs used in cell medium, the performance of DMSA and TAT were comparable (31990 and 51904 p/s per mg of ZGO in cells). The fact that lower concentrations of DMSA-ZGO were needed to achieve the same luminescence than their counterparts seems to indicate that this functionalization strategy might improve the performance as contrast agents of ZGO NPs. However, a deeper study of the effect that DMSA has on the optical properties of ZGO would be required to confirm this. A similar effect triggered by the use ligands but in a different system was reported in the literature. Alterations in the intensity of NIR luminescence of protecting monolayers of Au38and Au140 quantum dots were shown by Wang *et al*.[69] They conducted a systematic study about the effect of ligand on NIR luminescence on this system.[69] They found out that the increase in NIR luminescence is proportional to the polarity of the ligands and the level of ligand exchange. They also showed that this increase is due to the binding of electron-withdrawing groups to the gold cores. In addition, they also reported an increase in NIR luminescence intensity after functionalization with carboxylic acids linked by a small chain.[69]

DMSA is a short molecule functionalised with two thiols and two carboxylic acids. Therefore, we might be observing a similar effect on the ZGO NPs. However, as mentioned before a thorough study of the effect of ligands on our system needs to be conducted before jumping into conclusions. In addition, we expect that this effect is size-dependent. Smaller NPs (like ZGO) have greater surface areas and seems likely that this effect on optical properties caused by ligands is happening only on the surface of NPs.

4.4.3 DMSA-ZGO

DMSA was selected as the most appropriate ligand due to its effective luminescence intensity per mg of product and its stability in cell medium. In addition, there is one step less in the DMSA functionalization protocol, improving the final yield comparing to TAT-coated NPs. Cell uptake of DMSA was studied in more detail and compared to non-functionalized ZGO. Figure 4.13 shows the luminescence measured of labelled MSCs with non-functionalized and DMSA coated ZGO at different concentration. Similarly to section 4.4.2, dilutions were made here so the particles were emitting at a comparable intensity in solution and then MSCs were incubated for 24 hours. As it can be observed in figure 4.13 A DMSA-ZGOs clearly underwent a much higher cellular uptake. In the graph it can be seen that the intensities of MSCs labelled with DMSA-ZGOs are 3-fold higher than with “naked” ZGO. Moreover, TEM pictures confirmed the remarkable uptake with DMSA ligands. Similarly to GNRs, ZGO particles are trapped in cellular vesicles, indicating that NPs were uptaken *via* endocytosis. As mentioned before, the luminescent optical properties of ZGO NPs are not affected by the packing in endosomes.

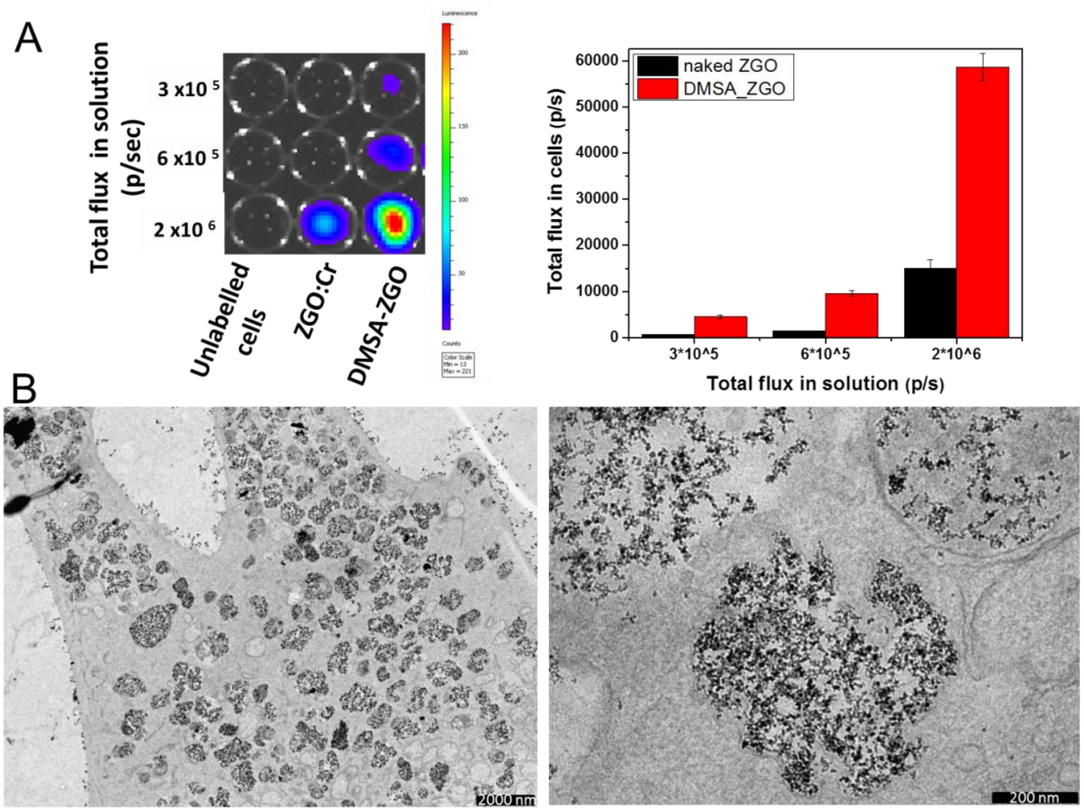

Figure 4.13 Cell uptake of DMSA coated NPs. A) Luminescence intensities of MSCs labelled at non-functionalized and DMSA-ZGOs at different concentrations. Error bars are the standard deviation of the average over 3 replicates. B) TEM pictures of MSCs slices after 24 hours incubation with DMSA-ZGO at 2 mg/mL.

4.5 Dual labelling

Multimodal imaging is a necessary field since it can overcome the drawback of a particular imaging technique by combining it with a different technique. When probes are designed to be injected systemically, there is a reasonable need to bind both probes to make sure that the signal measured by the different techniques is located in the same anatomical region. In our case, NPs are used for cell labelling and both GNRs and ZGO were shown to be uptaken *via* the same cellular mechanism, being both of them found in the endosomes. Another advantage of co-labelling over hybrid probes is that the different components can be easily modulated by increasing (or decreasing) the concentration before the incubation. In addition, it is well known that metals such as gold can quench emission of fluorophores depending on distance[70,71,72]. In addition, in our specific case, the number of ZGO NPs incubated with cells was much bigger than GNRs. For example, 2 mg/mL ZGO corresponded approximately to 4.75×10^{15} NP/mL, whilst GNRs were incubated at a concentration = 1 nM (i.e. 6.47×10^{11}). Although, this proportion was not necessarily maintained inside cells, seems obvious that the number of ZGO needed to provide a good signal has to be much higher than that for GNRs, which for this application makes it difficult the use of hybrids. For this reason we chose a co-labelling approach. Instead of binding both probes together, we decided to co-incubate both types of NPs with the cells simultaneously. We expected to find both probes in the same endosomes; hence we should be able to locate both signals inside cells. The potential drawbacks of co-labelling to be considered are: adverse effects on colloidal stability due to interparticle interactions and effects on cell viability much bigger than the ones for individual NPs. DMSA modified ZGO NPs and PEG-COOH modified GNRs were pre-mixed at the appropriate concentrations before incubation. No aggregation effects were observed, the negative charge of both NPs resulted in an electrostatic repulsion attributable for the colloidal stability of the mixture. In order to quantify the percentage of viable cells we used a luminescent based assay which measures the amount of ATP after cells are lysed. ATP available is directly proportional to cell viability. Note that colorimetric assays such as MTT were not the most appropriate here because the absorbance of GNRs could interfere with the final results, contrarily ZGO does not interfere with luminescence assays since they need to be activated with white light to show emission. Figure 2.14 shows the results obtained with ATP assay after 24 hours of incubation with PEG-COOH-GNRs (1 nM), DMSA-ZGO (2 mg/mL) and dual labelling (i.e. 1 nM GNRs and 2 mg/mL ZGO). The results showed that no dramatic changes resulted from the incubation of MSCs with the different probes since the viability of all the samples tested was higher than 80 %.

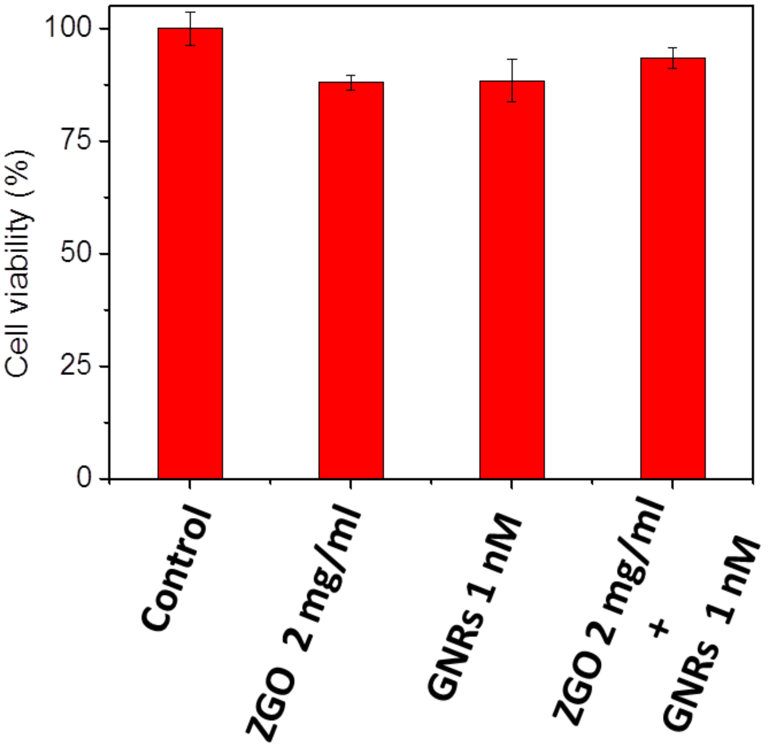

Figure 2.14: Cell viability of MCDs. ATP assay after labelling cells with PEG-COOH modified GNRs, DMSA modified ZGO and co-incubation of both probes at the final concentrations used for 24 hours. Error bars are the standard deviation of the average over 3 replicates.

4.5.1 Effect of dual labelling on optical properties of GNRs

As shown in section 4.3.1.3, optical properties of GNRs might change after being uptaken by cells and packed in endosomes, which might favour agglomeration and/or plasmon coupling. We showed in a parallel work that optical properties of GNRs in solution could be preserved inside cells by physically separating the gold cores using a 35 nm silica shell.[60] We showed that this leads to the improvement of sensitivity in photoacoustic detection of stem cells *in vivo*.

Figure 4.15 A shows the vis-NIR spectra of MSCs labelled cells with GNRs alone and dual labelling with GNRs and ZGOs. As it was expected, cell labelling with GNRs alone (in red) resulted in a broad plasmon band and decrease of intensity in the 700-900 nm range. Conversely, when ZGOs and GNRs are co-incubated simultaneously, LSRP was better preserved and intensity in this range was much higher. Moreover, when the spectra obtained with dual labelled cells was compared with the spectra of GNRs in solution, there is a shift of just a few nanometres. Therefore, these results show that co-incubation of GNRs with ZGOs had a protective effect against plasmon coupling. Figure 4.15 B shows the spectrum obtained from the two different labelled cells after lysis and plasmon coupling reverted. As it was previously explained, packing of NPs in endosomes is reverted when cells are lysed, recovering their optical properties. Interestingly, AUC was higher when GNRs were incubated alone. This indicates that the concentration of gold in cells was actually higher, but less effective in maintaining the optical signature of GNRs. These results highlight the importance of avoiding plasmon coupling to enhance the efficiency of GNRs when the final application relies on their optical properties.

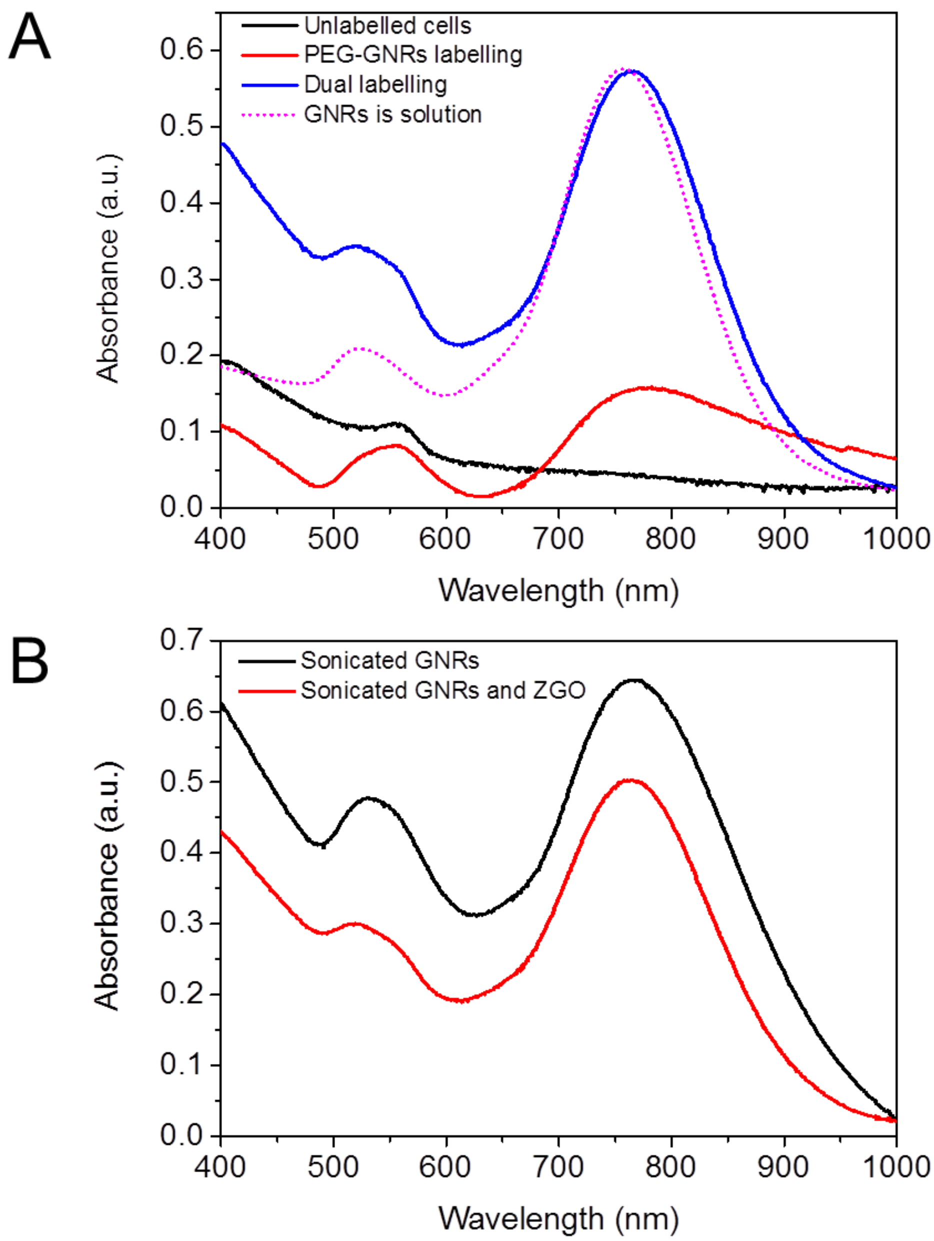

Figure 4.15: Optical properties of labelled cells with GNRs and co-labelling with GNRSs and ZGOs. A) vis-NIR of labelled cells. Dashed line shows the spectra of PEG-GNRs in solution for a comparison with the labelled cells. B) vis-NIR of cells shown in A after sonication and consequent lysis of cells.

TEM pictures of labelled cells confirmed the packing of NPs inside endosomes. Figure 4.16 A shows the agglomeration of GNRs inside the cellular vesicles. Moreover, fusion of gold cores can be observed in some cases. This is in agreement with the decrease in intensity and broadening of the LSPR band observed in the vis-NIR spectra. On the other hand, TEM pictures of co-labelled cells showed that ZGOs physically separated GNRs (Figure 4.16 B), improving like this the optical properties of GNRs in cells. Avoiding plasmon coupling not only improves the intensity of our contrast and hence, sensitivity of the imaging method but it can also avoid irreproducibility problems since plasmon coupling inside the cell has a random nature.

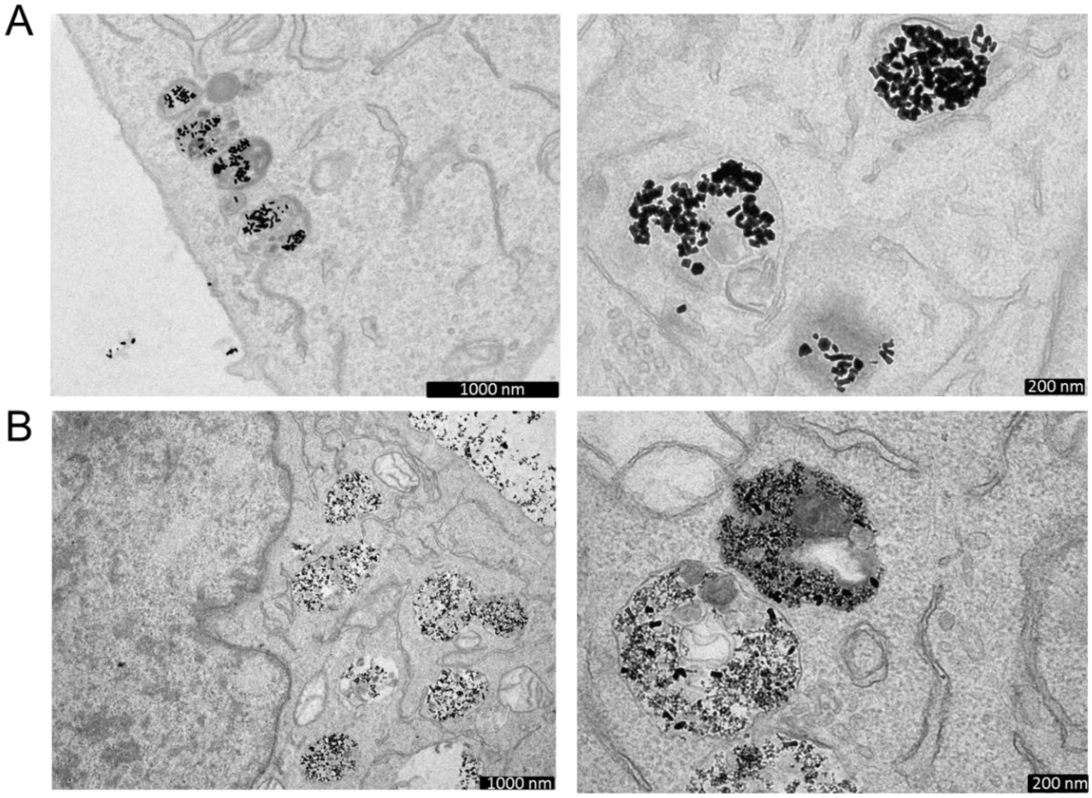

Figure 4.16: TEM pictures of A) PEG_COOH-GNRs labelled cells and B) Dual labelling (i.e. DMSA-ZGOs and PEG_COOH-GNRs).

4.5.2 Effect of dual labelling on optical properties of ZGOs

The effect that GNRs may produce in the luminescent properties is more delicate. As mentioned before quenching of fluorescence by metallic NPs has widely been reported in the literature. While this effect depends on many conditions, distance is one of the most important. Longer distances between the metallic NPs and the fluorophore have been reported to decrease the quenching and even avoiding it completely if distance between probes is big enough.[70] Figure 4.16A shows the luminescence of GNRs (4.8 O.D. in cell culture medium, approximately 1 nM), ZGO (2 mg/mL, or 7.9 µM) and co-incubation of both NPs in cell medium (4.8 O.D. GNRs + 2mg/mL ZGO in cell culture medium). Figure 4.16B shows the luminescent intensities of cells labelled with the previous conditions for 24 hours. In both scenarios, GNRs seem to have an inhibition effect on ZGO luminescent signal. Interestingly, this quantitative decrease is similar in both cases, being around the half of the intensity measured with ZGOs alone. The decrease in luminesce is observed in both the cell medium before labelling and inside the labelled cells. Hence, selective cell uptake of the different NPs is not causing it. In addition, the relatively small number of GNRs compared to ZGO as observed in the TEM picture could indicate that a local quenching is not causing this effect, at least not completely. An inner filter effect is more likely to be causing this decrease that accounts for the half of the luminesce. ZGO NPs have a emission spectra with a sharp peak at 694 nm which partially overlaps with LSRP of GNRs.

This inhibition of the luminescence of ZGO caused by GNRs could be reduced by using longer GNRs that absorbs at longer wavelength in the second optical window, avoiding the overlap of optical properties of both probes. For timing reasons we could not carry out the experiment changing these conditions. In addition, MSOT is measuring between 660 and 900 nm in standard conditions. Therefore LSPR fitting this range are the most appropriate for photoacoustic measures. Despite the decrease on luminescence caused by GNRs, the signal is still high enough to be able to detect a small number of cells (≈30000). In the next chapter, *in vivo* studies obtained with these labelled cells are shown.

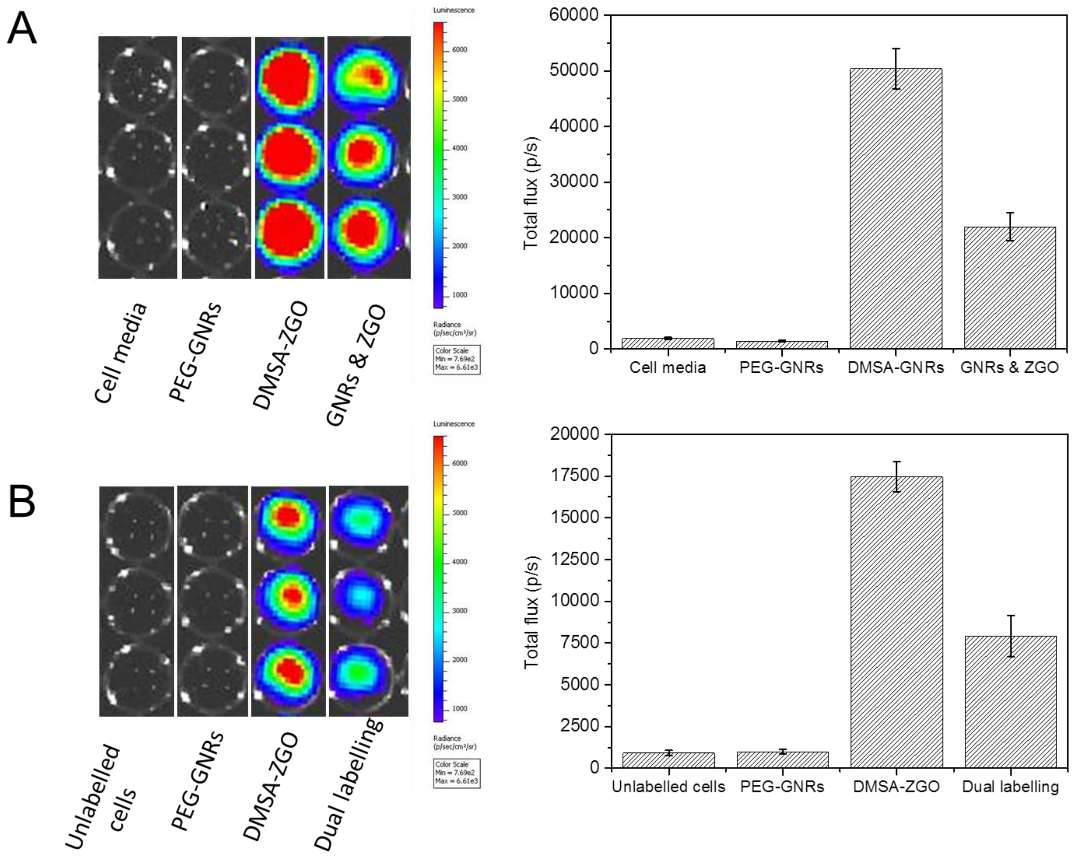

Figure 4.17: Luminescence intensities of A) mixture of ZGO and GNRs in cell medium. B) Different strategies of labelled cells. Error bars are the standard deviation of the average over 3 replicates.

4.6 Conclusions

Cellular interaction of GNRs modified with a long chain PEG and a short chain with a COOH terminus PEG were investigated. Long chain PEG-GNRs did not show any cellular uptake. On the contrary, negative surface charge of GNRs modified with short chain PEG-COOH allowed protein adsorption leading to an increase in the colloidal stability in physiological media and promoted cellular uptake. In addition, TAT and BSA-GNRs bioconjugates exhibiting different surface charges in aqueous solution were studied. However, the average surface charge shifted to negative after incubation with cell culture media in all cases due to the adsorption of proteins on the surface. Therefore, physicochemical properties of NPs need to be assessed before and after exposure to physiological environments in order to understand NP-cell interactions.

DMSA conjugation of ZGO significantly increased cell uptake while maintaining colloidal stability. In addition, the surface effect of DMSA observed on ZGO luminescent intensity needs to be further studied. For this, measuring the intensity of luminescence with different number of DMSA molecules on ZGO surface would provide more information.

Cells were co-labelled with ZGO and GNRs following a simultaneous co-incubation approach. Since the amount of ZGO needed to provide a good signal has to be much higher than that for GNRs, this approach is more appropriate than the use of hybrids. Co-labelling resulted in an alteration of the optical properties of both probes. First, a decrease in the intensity of the luminescent signal was caused by the presence of GNRs. Differences in cell uptake does not seem to be the problem since this was observed also in the cell medium before cell labelling. Absorption of emitted light by GNRS is more likely to be causing this decrease. On the other hand, LSRP of GNRs was better preserved; it only shifted a few nanometres compared with the spectra of GNRs in solution. Moreover, intensity was significantly improved in contrast to cells labelled only with GNRs. This indicates that co-incubation of GNRs with ZGOs attenuates the effect of plasmon coupling on the optical properties of

GNRs. TEM pictures confirmed that both particles are located inside cellular endosomes, separating the gold cores.

4.7 Bibliography

1. Conner, S. D. & Schmid, S. L. Regulated portals of entry into the cell. *Nature* **422,** 37–44 (2003).
2. Wang, T., Bai, J., Jiang, X. & Nienhaus, G. U. Cellular uptake of nanoparticles by membrane penetration: A study combining confocal microscopy with FTIR spectroelectrochemistry. *ACS Nano* **6,** 1251–1259 (2012).
3. Alkilany, A. M. & Murphy, C. J. Toxicity and cellular uptake of gold nanoparticles: What we have learned so far? *J. Nanoparticle Res.* **12,** 2313–2333 (2010).
4. Behzadi, S. *et al.* Cellular uptake of nanoparticles: journey inside the cell. *Chem. Soc. Rev.* **46,** 4218–4244 (2017).
5. Dobrovolskaia, M. A. & McNeil, S. E. Immunological properties of engineered nanomaterials. *Nat. Nanotechnol.* **2,** 469 (2007).
6. Couvreur, P. & Vauthier, C. *Nanotechnology: Intelligent design to treat complex disease*. *Pharmaceutical Research* **23,** (2006).
7. Taggart, M. J. Smooth Muscle Excitation-Contraction Coupling: a Role for Caveolae and Caveolins? *Physiology* **16,** 61–65 (2001).
8. Anderson, R. G. W. The Caveolae Membrane System. *Annu. Rev. Biochem.* **67,** 199–225 (1998).
9. Sahay, G., Alakhova, D. Y. & Kabanov, A. V. Endocytosis of Nanomedicines. *J. Control. Release* **145,** 182–195 (2010).
10. Doherty, G. J. & McMahon, H. T. Mechanisms of Endocytosis. *Annu. Rev.*

Biochem. **78,** 857–902 (2009).

11. Lu, Y. & Low, P. S. Folate-mediated delivery of macromolecular anticancer therapeutic agents. *Adv. Drug Deliv. Rev.* **54,** 675–693 (2002).

12. Kelemen, L. E. The role of folate receptor α in cancer development, progression and treatment: Cause, consequence or innocent bystander? *Int. J. Cancer* **119,** 243–250 (2006).

13. Lim, J. P. & Gleeson, P. A. Macropinocytosis: An endocytic pathway for internalising large gulps. *Immunol. Cell Biol.* **89,** 836–843 (2011).

14. Ridley, A. J. Rho Proteins: Linking Signaling with Membrane Trafficking. *Traffic* **2,** 303–310 (2001).

15. Mellman, I. & Steinman, R. M. Dendritic Cells. *Cell* **106,** 255–258 (2018).

16. Kuhn, D. A. *et al.* Different endocytotic uptake mechanisms for nanoparticles in epithelial cells and macrophages. *Beilstein J. Nanotechnol.* **5,** 1625–1636 (2014).

17. Tabata, Y. & Ikada, Y. Effect of the size and surface charge of polymer microspheres on their phagocytosis by macrophage. *Biomaterials* **9,** 356–362 (1988).

18. Liu, Y. *et al.* Impact of hydrogel nanoparticle size and functionalization on in vivo behavior for lung imaging and therapeutics. *Mol. Pharm.* **6,** 1891–1902 (2009).

19. Chithrani, B. D., Ghazani, A. A. & Chan, W. C. W. Determining the size and shape dependence of gold nanoparticle uptake into mammalian cells. *Nano Lett.* **6,** 662–668 (2006).

20. Jiang, W., Kim, B. Y. S., Rutka, J. T. & Chan, W. C. W. Nanoparticle-mediated cellular response is size-dependent. *Nat. Nanotechnol.* **3,** 145–150 (2008).

21. Nabiev, I. *et al.* Nonfunctionalized nanocrystals can exploit a cell's active transport machinery delivering them to specific nuclear and cytoplasmic

compartments. *Nano Lett.* **7,** 3452–3461 (2007).

22. Chaudhuri, A., Battaglia, G. & Golestanian, R. The effect of interactions on the cellular uptake of nanoparticles. *Phys. Biol.* **8,** (2011).

23. Albanese, A. & Chan, W. C. W. Effect of gold nanoparticle aggregation on cell uptake and toxicity. *ACS Nano* **5,** 5478–5489 (2011).

24. Champion, J. A. & Mitragotri, S. Shape induced inhibition of phagocytosis of polymer particles. *Pharm. Res.* **26,** 244–249 (2009).

25. Chithrani, B. D. & Chan, W. C. W. Elucidating the mechanism of cellular uptake and removal of protein-coated gold nanoparticles of different sizes and shapes. *Nano Lett.* **7,** 1542–1550 (2007).

26. Qiu, Y. *et al.* Surface chemistry and aspect ratio mediated cellular uptake of Au nanorods. *Biomaterials* **31,** 7606–7619 (2010).

27. Gratton, S. E. A. *et al.* The effect of particle design on cellular internalization pathways. *Proc. Natl. Acad. Sci.* **105,** 11613–11618 (2008).

28. Harush-Frenkel, O., Debotton, N., Benita, S. & Altschuler, Y. Targeting of nanoparticles to the clathrin-mediated endocytic pathway. *Biochem. Biophys. Res. Commun.* **353,** 26–32 (2007).

29. Li, Y. & Gu, N. Thermodynamics of Charged Nanoparticle Adsorption on Charge-Neutral Membranes: A Simulation Study. *J. Phys. Chem. B* **114,** 2749–2754 (2010).

30. Lin, J., Zhang, H., Chen, Z. & Zheng, Y. Penetration of Lipid Membranes by Gold Nanoparticles: Insights into Cellular Uptake, Cytotoxicity, and Their Relationship. *ACS Nano* **4,** 5421–5429 (2010).

31. Wang, B., Zhang, L., Bae, S. C. & Granick, S. Nanoparticle-induced surface reconstruction of phospholipid membranes. *Proc. Natl. Acad. Sci.* **105,** 18171–18175 (2008).

32. Leroueil, P. R. *et al.* Wide Varieties of Cationic Nanoparticles Induce Defects in Supported Lipid Bilayers. *Nano Lett.* **8,** 420–424 (2008).

33. Cho, E. C., Xie, J., Wurm, P. A. & Xia, Y. Understanding the Role of Surface Charges in Cellular Adsorption versus Internalization by Selectively Removing Gold Nanoparticles on the Cell Surface with a I2/KI Etchant. *Nano Lett.* **9,** 1080–1084 (2009).

34. Krpetić, Ž. *et al.* Negotiation of intracellular membrane barriers by TAT-modified gold nanoparticles. *ACS Nano* **5,** 5195–5201 (2011).

35. Hauck, T. S., Ghazani, A. A. & Chan, W. C. W. Assessing the Effect of Surface Chemistry on Gold Nanorod Uptake, Toxicity, and Gene Expression in Mammalian Cells. *Small* **4,** 153–159 (2008).

36. Kim, S. T., Saha, K., Kim, C. & Rotello, V. M. The role of surface functionality in determining nanoparticle cytotoxicity. *Acc. Chem. Res.* **46,** 681–691 (2013).

37. Li, Y., Chen, X. & Gu, N. Computational Investigation of Interaction between Nanoparticles and Membranes: Hydrophobic/Hydrophilic Effect. *J. Phys. Chem. B* **112,** 16647–16653 (2008).

38. Gopalakrishnan, G. *et al.* Multifunctional Lipid/Quantum Dot Hybrid Nanocontainers for Controlled Targeting of Live Cells. *Angew. Chemie Int. Ed.* **45,** 5478–5483 (2006).

39. Lipinski, C. A. Lead- and drug-like compounds: the rule-of-five revolution. *Drug Discov. Today Technol.* **1,** 337–341 (2004).

40. Grzelczak, M. P. *et al.* Ion Transport across Biological Membranes by Carborane-Capped Gold Nanoparticles. *ACS Nano* **11,** 12492–12499 (2017).

41. Lynch, I. & Dawson, K. A. Protein-nanoparticle interactions. *Nano Today* **3,** 40–47 (2008).

42. Walczyk, D., Bombelli, F. B., Monopoli, M. P., Lynch, I. & Dawson, K. A. What the Cell ‘Sees’ in Bionanoscience. *J. Am. Chem. Soc.* **132,** 5761–5768 (2010).

43. Lesniak, A. *et al.* Effects of the presence or absence of a protein corona on silica nanoparticle uptake and impact on cells. *ACS Nano* **6,** 5845–5857

(2012).

44. Treuel, L., Docter, D., Maskos, M. & Stauber, R. H. Protein corona - from molecular adsorption to physiological complexity. *Beilstein J. Nanotechnol.* **6,** 857–873 (2015).

45. Saptarshi, S. R., Duschl, A. & Lopata, A. L. Interaction of nanoparticles with proteins: Relation to bio-reactivity of the nanoparticle. *J. Nanobiotechnology* **11,** 1–12 (2013).

46. Pastoriza-Santos, I. & Liz-Marzán, L. M. Reliable Methods for Silica Coating of Au Nanoparticles BT - Nanomaterial Interfaces in Biology: Methods and Protocols. in (eds. Bergese, P. & Hamad-Schifferli, K.) 75–93 (Humana Press, 2013). doi:10.1007/978-1-62703-462-3_6

47. Alkilany, A. M. *et al.* Cellular uptake and cytotoxicity of gold nanorods: Molecular origin of cytotoxicity and surface effects. *Small* **5,** 701–708 (2009).

48. Rayavarapu, R. G., Petersen, W. & Hartsuiker, L. In vitro toxicity studies of polymer-coated gold nanorods. (2010). doi:10.1088/0957-4484/21/14/145101

49. Jokerst, J. V, Lobovkina, T., Zare, R. N. & Gambhir, S. S. Nanoparticle PEGylation for imaging and therapy. *Nanomedicine (Lond).* **6,** 715–728 (2011).

50. Mercer, R. R. *et al.* Alteration of deposition pattern and pulmonary response as a result of improved dispersion of aspirated single-walled carbon nanotubes in a mouse model. *Am. J. Physiol. - Lung Cell. Mol. Physiol.* **294,** L87–L97 (2008).

51. Chithrani, D. B. Polyethylene Glycol Density and Length Affects Nanoparticle Uptake by Cancer Cells. *J. Nanomedicine Res.* **1,** (2014).

52. Walkey, C. D. & Chan, W. C. W. Understanding and controlling the interaction of nanomaterials with proteins in a physiological environment. *Chem. Soc. Rev.* **41,** 2780–2799 (2012).

53. Niidome, T. *et al.* PEG-modified gold nanorods with a stealth character for in vivo applications. *J. Control. Release* **114,** 343–347 (2006).

54. Taylor, A., Wilson, K. M., Murray, P., Fernig, D. G. & Levy, R. Long-term tracking of cells using inorganic nanoparticles as contrast agents: are we there yet? *Chem. Soc. Rev.* **41,** 2707–2717 (2012).

55. Lundqvist, M. *et al.* The evolution of the protein corona around nanoparticles: A test study. *ACS Nano* **5,** 7503–7509 (2011).

56. Hillaireau, H. & Couvreur, P. Nanocarriers' entry into the cell: Relevance to drug delivery. *Cell. Mol. Life Sci.* **66,** 2873–2896 (2009).

57. Zhang, W., Ji, Y., Meng, J., Wu, X. & Xu, H. Probing the behaviors of gold nanorods in metastatic breast cancer cells based on uv-vis-nir absorption spectroscopy. *PLoS One* **7,** (2012).

58. Funston, A. M., Novo, C., Davis, T. J. & Mulvaney, P. Plasmon coupling of gold nanorods at short distances and in different geometries. *Nano Lett.* **9,** 1651–1658 (2009).

59. Sánchez-Iglesias, A., Grzelczak, M., Pérez-Juste, J. & Liz-Marzán, L. M. Binary Self-Assembly of Gold Nanowires with Nanospheres and Nanorods. *Angew. Chemie Int. Ed.* **49,** 9985–9989 (2010).

60. Comenge, J. *et al.* Preventing Plasmon Coupling between Gold Nanorods Improves the Sensitivity of Photoacoustic Detection of Labeled Stem Cells in Vivo. *ACS Nano* **10,** 7106–7116 (2016).

61. Droste, M. S. *et al.* Noninvasive measurement of cell volume changes by negative staining. *J. Biomed. Opt.* **10,** 64017 (2011).

62. Richter, T. *et al.* Pros and cons: Cryo-electron microscopic evaluation of block faces versus cryo-sections from frozen-hydrated skin specimens prepared by different techniques. *J. Microsc.* **225,** 201–207 (2007).

63. Kunisawa, J. *et al.* Fusogenic liposome delivers encapsulated nanoparticles for cytosolic controlled gene release. *J. Control. Release* **105,** 344–353 (2005).

64. Josephson, L., Tung, C., Moore, A. & Weissleder, R. High-Efficiency Intracellular Magnetic Labeling with Novel Superparamagnetic-Tat Peptide Conjugates. 186–191 (1999). doi:10.1021/bc980125h

65. Derossi, D., Calvet, S. & Trembleau, A. Cell Internalization of the Third Helix of the Antennapedia Homeodomain Is Receptor-independent *. **271,** 18188–18193 (1996).

66. Yokoyama, K. & Welchons, D. R. The conjugation of amyloid beta protein on the gold colloidal nanoparticles' surfaces. *Nanotechnology* **18,** 105101 (2007).

67. Yuna, K., Min, K. S. & Jwa-Min, N. Protein–Nanoparticle Interaction-Induced Changes in Protein Structure and Aggregation. *Chem. – An Asian J.* **11,** 1869–1877 (2016).

68. Fleischer, C. & Payne, C. K. Secondary Structure of Corona Proteins Determines the Cell Surface Receptors Used by Nanoparticles. *J. Phys. Chem. B* (2014). doi:10.1021/jp502624n

69. Wang, G., Guo, R., Kalyuzhny, G., Choi, J. P. & Murray, R. W. NIR luminescence intensities increase linearly with proportion of polar thiolate ligands in protecting monolayers of Au38and Au140quantum dots. *J. Phys. Chem. B* **110,** 20282–20289 (2006).

70. Jin, Y. & Gao, X. Plasmonic fluorescent quantum dots. *Nat. Nanotechnol.* **4,** 571–576 (2009).

71. Bardhan, R., Grady, N. K., Cole, J. R., Joshi, A. & Halas, N. J. Fluorescence enhancement by au nanostructures: Nanoshells and nanorods. *ACS Nano* **3,** 744–752 (2009).

72. Ma, X. *et al.* Photoluminescence of Individual Au/CdSe Nanocrystal Complexes with Variable Interparticle Distances. *J. Phys. Chem. Lett.* **2,** 2466–2471 (2011).

Chapter 5

Photoacoustic and Optical Imaging

5.1 Introduction

The recent advances in the development of non-invasive *in vivo* molecular imaging techniques and their respective appropriate contrast agents are having a large impact on different biomedical fields including oncology[1], cardio-vascular deseases[2] and cell tracking[3]. Studying the fate of implanted stem cells (i.e. biodistribution, viability and possible tumorigenicity) might help in the translation of regenerative medicine treatment into humans.[4]

Optical imaging is broadly being used in biological research thanks to the advances made in the field such as the development of the fluorescent protein technology.[5] The improvement of near infrared (NIR) optical contrast along with appropriate instruments enables the use of this technique in the whole-body imaging of small animals.[6,7] Their remarkable sensitivity (in the picomolar range), its low cost and user-friendly handling make it a popular imaging technique. [8, 9] However, this technique is limited by the poor penetration depth (< 1 cm) due to the photon scattering in tissue. On the other hand, Photoacoustic imaging (PAI) is arising as a versatile and powerful tool in bioimaging.[10] It relies on the ability of a chromophore to absorb light pulses and generate a subsequent ultrasound.[11] Thus, PAI is a hybrid method that combines the high sensitivity of optical methods, in the picomolar range, with the high resolution of ultrasound detection, 150 µm in our system.[12] In addition, scattering coefficient in biological tissue of USs is 2 or 3 orders of magnitude lower than photons,[13] improving the penetration depth of pure optical imaging techniques. Multispectral optoacoustic tomography (MSOT) is an imaging method derived from PAI, the distinctive characteristic of MSOT respect to other photoacoustic imaging devices is the possibility to irradiate at different wavelengths.[14] This enables the spectral resolution of different endogenous chromophores in animal tissues (e.g. haemoglobin and melanin) in real time[15] and even the volumetric quantitative molecular imaging in entire small animals at the same time that anatomical information is provided.[14] The signal is based on the generation and propagation of ultrasounds. Therefore, imaging of anatomical regions where density and sound speed varies from the rest of the body is challenging.[16] Moreover, organs such as lungs or stomach cannot be imaged by this technique due to air content. We have combined the high resolution and penetration depth of MSOT with the sensitivity and whole-body imaging that pure optical methods offer.

The detection capabilities of MSOT can be greatly enhanced by the use of exogenous contrast agents. While direct labelling methods are predominant for this technique, including nanoparticles (NPs) and dyes, some reporter genes such as near infrared fluorescent protein iRFP720 have been used as well.[17] Among the different approaches for direct labelling, gold nanoparticles (GNPs) have attracted a lot of attention as PAI contrasts due to their strong absorption as a consequence of the surface plasmon resonance (SPR) effect.[18] Optical absorption of GNPs is several orders of magnitude higher than organic dyes.[19] For *in vivo* PAI, only GNPs that absorb in the NIR or optical window are used.[20] This includes gold nanorods (GNRs), gold nanoshells, gold nanoprisms, gold nanocages and gold nanostars.[21] GNRs have been extensively used due to the relatively simple preparation method and the possibility to tune the optical properties within the NIR window. MSOT is a spectroscopic technique able to resolve different chromophores, false positives due to endogenous cromophores with a similar absorption profile can occur. This may happen especially in highly vascularized organs such as the liver due to the absorption of pulsed light by haemoglobin.[22] Therefore, using a complementary technique might be beneficial not only to image regions where photoacoustic imaging is not possible, but also to discriminate false positives.

Here we explore the combination of GNRs with persistent luminescent nanoparticles (PLNPs). PL is an optical phenomenon that involves photoelectron storage after optical charging with UV, vis or NIR light and the slow release of charged carriers that can last from minutes to hours.[23,24] These long lifetimes addresses the auto-fluorescence reported in fluorescent probes that increases the background signal since excitation and emission measurement can be separated in time.[25] This ultimately increases the signal-to-noise ratio, improving the limit of detection of the method.[26] This along with the optical properties (excitation and emission) in the NIR and improvement of synthetic routes made in the recent years has positioned LPNPs as promising optical contrast agents.[23] Here we have used Chromium doped zinc gallium oxide (ZGO:Cr) nanocrystals synthesized by a single-step hydrothermal approach,[27] as a complementary imaging method to MSOT.

Direct methods (i.e. labelling with probes) suffer from the signal dilution of the contrast agent over cell division. In addition, cell viability cannot be tracked and the release of probes after cell death may lead to misinterpretation of data.[28] Reporter genes overcome these problems since are retained in the successive generation after cell division.[29] Bioluminescence imaging (BLI) has the potential to offer an extraordinary sensitivity when reporter genes such as luciferase are used.[30] Firefly luciferase has extensively been used due to the fact that its substrates are well tolerated by animals and their emission peaks at around 562 nm, closest to the infrared window for in vivo imaging.[31] However, not all cells can be transfected. For example, primary cells such as macrophages have very low transfection efficiency being very challenging to image them by BLI.[32] In addition, this approach is obviously restricted to preclinical models due to the need to genetically modify the cells. Thus, although it is still in the early stages, the emerging field of PLNPs has a huge potential to extend the use of luminescence for *in vivo* imaging.

In this chapter, we present the imaging results obtained by MSOT, BLI and persistent luminescence imaging in mice after subcutaneous and intracardiac injection of GNRs and ZGOs-labelled mesenchymal stem cells (MSCs).

5.2 Experimental

Cell labelling: 5×10^5 MSCs were seeded in a 60 mm dish with 5 mL of cell culture medium (DMEM supplemented with 10% FBS). After 24 h, medium was replaced with 400 µL of NPs in 1.6 mL of fresh medium with 1% penicillin−streptomycin. For GNRs labelling, cell culture media was replaced with 5 mL of PEG-COOH-GNRs at a final concentration of 1.2 optical density (O.D.) in fresh media. For ZGO labelling, a final concentration 2 mg/mL of DMSA-ZGO in fresh was used. For dual labelling, a NPs mixture of PEG-COOH-GNRs at 4.8 O.D. and DMSA-ZGO:Cr at 2 mg/mL in fresh media . Finally, cells were incubated with NPs for 24 hours and dissociated using trypsin. Cells were resuspended in fresh medium, washed twice with PBS by sequential centrifugations (500g for 3 mins), and number of cells was determined using an automated cell counter (TC10, BioRad). An appropriate number of cells for each experiment in 100 μL of PBS were transferred to microcentrifuge tubes.

Animals. 8–10 week-old female SCID hairless outbred (SHO) mice (Charles River, Margate, UK) for whole body imaging or 8-10 week-old female CD1 mice (Charles River, Margate, UK) for the initial subcutaneous experiments were housed in individually ventilated cages at a 12 h light/dark cycle, with *ad libitum* access to food and water. Experimental animal protocols were performed in accordance with the guidelines under the Animals (Scientific Procedures) Act 1986 (licence PPL70/8741) and approved by the University of Liverpool Animal Welfare and Ethical Review Body.

All cell injection and imaging procedures of mice were carried out under general isoflurane/oxygen anaesthesia.

Subcutaneous injection: For GNRs-labelled cells, 8 to 10 week old female CD1 mice were shaved, and fur was epilated around the abdomen using depilatory cream. 2×10^6 unlabelled MSCs and 1×10^6, 2×10^6, and 6×10^6 PEG-COOH-GNR-labelled MSCs in 100 μL of PBS were injected subcutaneously at four different positions of the mouse flank (top right, top left, bottom right, and bottom left). For multimodal imaging, 7.5×10^5 MSCs were injected in SCID hairless outbred (SHO) instead.

Intracardiac injection: 10 weeks female Nude mice were positioned supine on a heated platform. Fur around the chest area was removed using depilatory cream and limbs were taped down to keep the mouse position fixed. Ultrasound gel was applied liberally to the chest area and the ultrasound transducer (Prospect imaging system, S-Sharp) was positioned above the chest so the long axis view of the left ventricle was visible. 100 µl of cell suspension was drawn up into an insulin syringe (29 G) and, using the ultrasound image as guidance, was inserted into the left ventricle of the heart. Cell suspension was then administered slowly over a period of approximately 30 s.

Bioluminescence imaging: IVIS spectrum system (PerkinElmer) was used. Animals received an intraperitoneal injection of D-luciferin (150 µg/g body weight, in PBS) 10 min prior to imaging (open filter, automatic mode).

Persistent luminescence imaging: Persistent luminescent measurements were acquired using an IVIS spectrum system (PerkinElmer). Excitation was performed by exposing the animals to 2 BLS-series white BioLED light sources (3000K, 12W), purchased from Mightex, for 5 minutes. Persistent luminescence measurements were performed by open filter and acquisition time was set to 2 minutes.

Photoacoustic imaging: An MSOT inVision 256-TF small animal imaging system (iThera Medical GmbH, Munich, Germany) was used. [33] After acclimatisation for 10 min inside the water bath, a whole-body scan was performed on the mouse with 1 mm steps and the following wavelengths for acquisition: 660, 670, 680, 690, 700, 705, 710, 715, 725, 735, 750, 765, 780, 795, 810, 820, 830, 840, 850, 860, 870, 880, 890, 900, 910, 920, 930, 940, 1025, 1050, 1075, and 1100 nm. Heavy water was used in the water bath due to its low absorbance at wavelengths >910 nm (contrary to regular water). Linear-mode-based reconstruction and guided ICA or lineal regression multispectral processing were applied using view MSOT software v3.6 (iThera Medical GmbH).

5.3 Imaging of Nanoparticles in solution

5.3.1 Imaging of GNRs in solution by Multispectral Optoacoustic Tomography (MSOT)

MSOT relies in the detection of ultrasonic waves generated as a consequence of a rapid thermoelastic expansion of photoabsorbing agents. The thermoelastic expansion and the consequent mechanical waves are a result of a temporal increase of temperature initiated by the absorption of light pulses.[34] For this reason, GNPs have arisen as powerful PA contrasts due to their strong and sharp absorption which results from surface plasmon resonance (SPR) effect. [21]

We assessed the performance of our GNRs in terms of sensitivity and multispectral resolution. Increasing concentration of GNRs were placed in phantoms and imaged by MSOT, corresponding MSOT intensities were calculated after multispectral reconstruction (Figure 5.1). GNRs at concentration as low as 6.5 pM were detected in phantoms. In addition, a linear relation between concentration of GNRs and MSOT signal was observed.

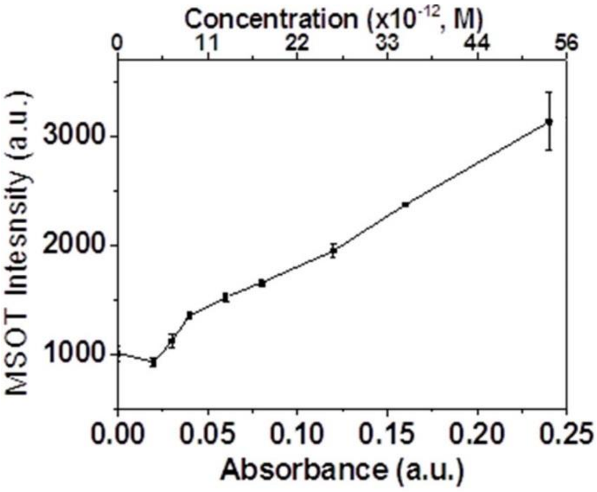

Figure 5.1: Limit of detections of MSOT. MSOT signal in arbitrary units (a.u.) of as synthesized GNRs in solution at different concentrations measured in phantoms. Concentration of GNRs is expressed in absorbance of the LSPR peak (a.u.) and in molarity.

The multi-wavelength approach of MSOT allows distinguishing between different cromophores. To test this feature with our system, GNRs with different aspect ratio (A.R) and therefore, different vis-NIR spectrum, were imaged in a phantom (Figure 5.2 A and B). The left well of the phantom was loaded with GNRs with an AR= 2.7 and the right well with GNR with an AR= 2.0. Acquisition wavelengths from 680nm until 900 nm in 5 nm wavelengths steps were used for this experiment. Images were processed in two different ways; single wavelength or multispectral (Figure 5.2 C and D respectively). Figure 5.2 A shows the single wavelength images of a phantom cross-section. MSOT intensities as a response to pulses of different wavelengths are presented (I=690nm, II=700nm, III=760 and IV=870 nm), showing the different intensities of MSOT signal in the different samples, which correlates with the different vis-NIR spectrum of the GNRs used here. For example, MSOT intensity at 800 nm is much higher for GNRs with AR=2.7, which absorb at longer wavelengths. Images processed by multispectral reconstruction (Figure 5.2 D), showed that the technique resolved GNRs with different A.R. After applying the reconstruction with the corresponding spectra, it perfectly discriminates between both GNRs.

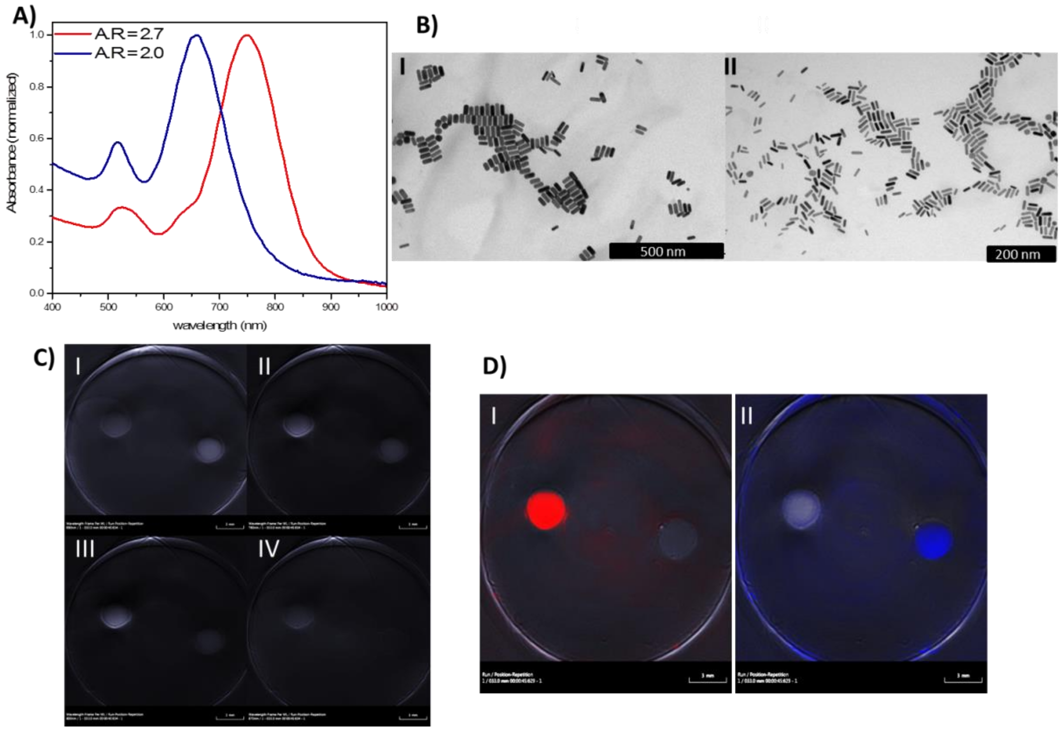

Figure 5.2: MSOT analysis of GNRs in solution. A) UV-VIS spectra of GNRs. B) TEM images of GNRs I) aspect ratio is 1.9. Scale bar represents 500 nm. II) Aspect ratio is 2.7. Scale bar represents 200 nm. C) Cross-section of commercial phantom at different wavelength. MSOT reconstruction was made by mode lineal method. I) image recorded at 690 nm. II) at 760 nm. III) at 800 nm. IV) at 870 nm. D) Multispectral reconstruction of a phantom cross-section using lineal regression reconstruction.

5.3.2 Imaging of Chromium doped zinc gallium oxide (ZGO:Cr) in solution

Persistent luminescent materials (PL) have arisen as promising candidates as optical probes for *in vivo* imaging due to its long emission times. These materials can glow for seconds, minutes or even hours after excitation is finished. This, allows the measurement in the absence of any excitation source, avoiding tissue auto-fluorescence and ultimately improving the signal to noise ratio.[26]

To investigate if ZGO:Cr NPs are suitable for optical bioimaging, optical properties of nanocrystals in solution were studied by IVIS Spectrum system (PerkinElmer). A good characterisation of probes *in vitro* is a crucial step to success in the *in vivo* stage. For this, first ZGO:Cr at a concentration of 10 mg/mL were excited at different wavelengths and the fluorescent emission signals measurements were compared (Figure 5.3 A). The highest emission signal recorded was a result of excitation at 570 nm and decreased as we moved from this wavelength. This is consistent with the optical properties measured with a fluorometer shown in chapter 3 and with the literature[27]. In addition, persistent luminescence of ZGO:Cr in solution was also studied. NPs were activated with a white LED lamp for 5 minutes and imaged at time 0, 2.5 minutes and 5 minutes after the activation (Figure 5.3 B). Intensity of the IVIS Spectrum System signal decreased with time until 5 minutes, when it was barely detectable. Once again, there was a consistency with the decay time measured with the fluorometer presented in Chapter 3.

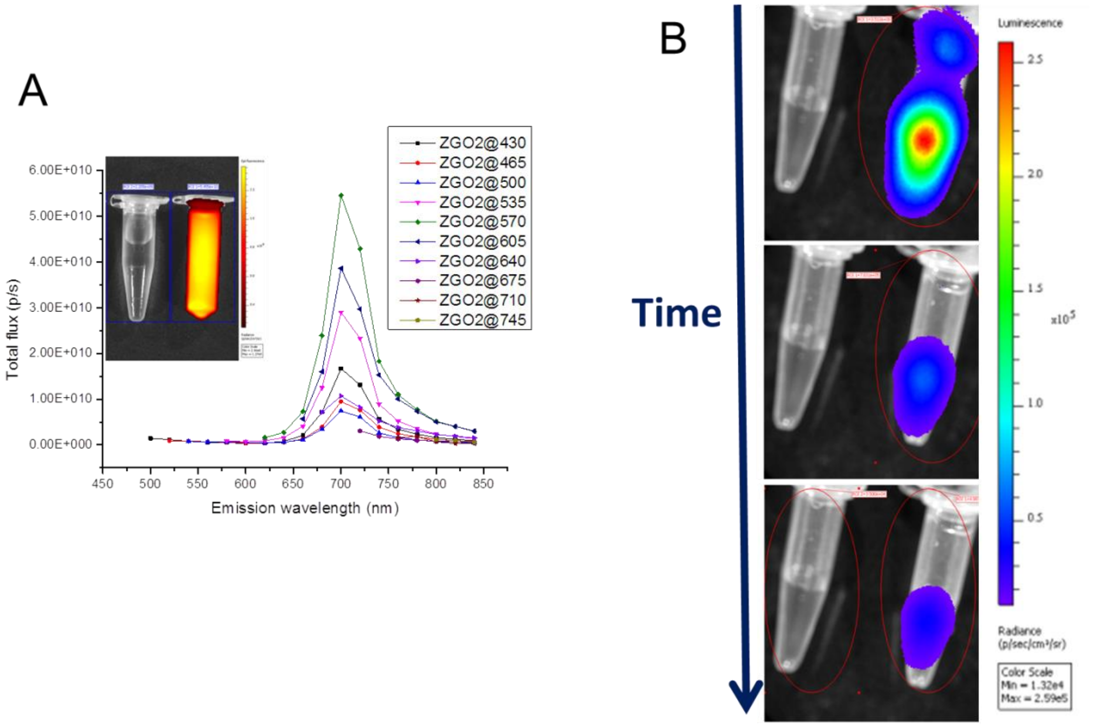

Figure 5.3: Optical properties of ZGO: Cr in solution measured by IVIS Spectrum system. A) Fluorescent emission signals after excitation at different wavelengths. Inset shows water and ZGO:Cr fluorescence at 570 nm B) Luminescence decay after activation with a white LED lamp for 5 mins. Measurement times shown are t=0, t= 2.5 mins and t=5 mins after the activation. Colour scale from 1.32×10^4 to 2.59×10^5 p/sec/cm^2/sr

5.4 Imaging of labelled cells

5.4.1 Imaging of GNRs-labelled cells by MSOT

Cells were labelled as previously explained, briefly MSCs were incubated with GNRs at O.D.= 1.2 in cell medium for 24 hours, washed with PBS and trypsinised. 3×10^5 GNRs-labelled MSC on a phantom were imaged by means of MSOT. Figure 5.4 shows the imaged processed by single wavelengths (A) and multispectral reconstruction (B). Labelled cells (right well of the phantom) were compared to unlabelled cells (left), used as control. Similarly to section 5.3.1, different intensities were obtained as a response to pulses of different wavelengths. Wavelengths from 690 to 900 with 5 nm steps were used for MSOT imaging. Here we show: I) 690 nm II) 730 nm III) 780nm IV) 900 nm). The higher intensities obtained correspond to the wavelength close to the LSPR peak, proving that the signal is generated by GNRs and excluding any artefact.

Multispectral processing was conducted as well with the labelled cells (Figure 5.4 B). Figure 5.4 C shows the MSOT intensities given by the background, the unlabelled cells used as negative control and the labelled cells. It is worth mentioning that the background and the control have equivalent intensities. The signal recorded by labelled cells is four times higher than the ones in the control and in the background. Note that background comes from the phantom, which is made out of a polymer with properties that mimics biological tissue in terms of transparency and sound propagation.

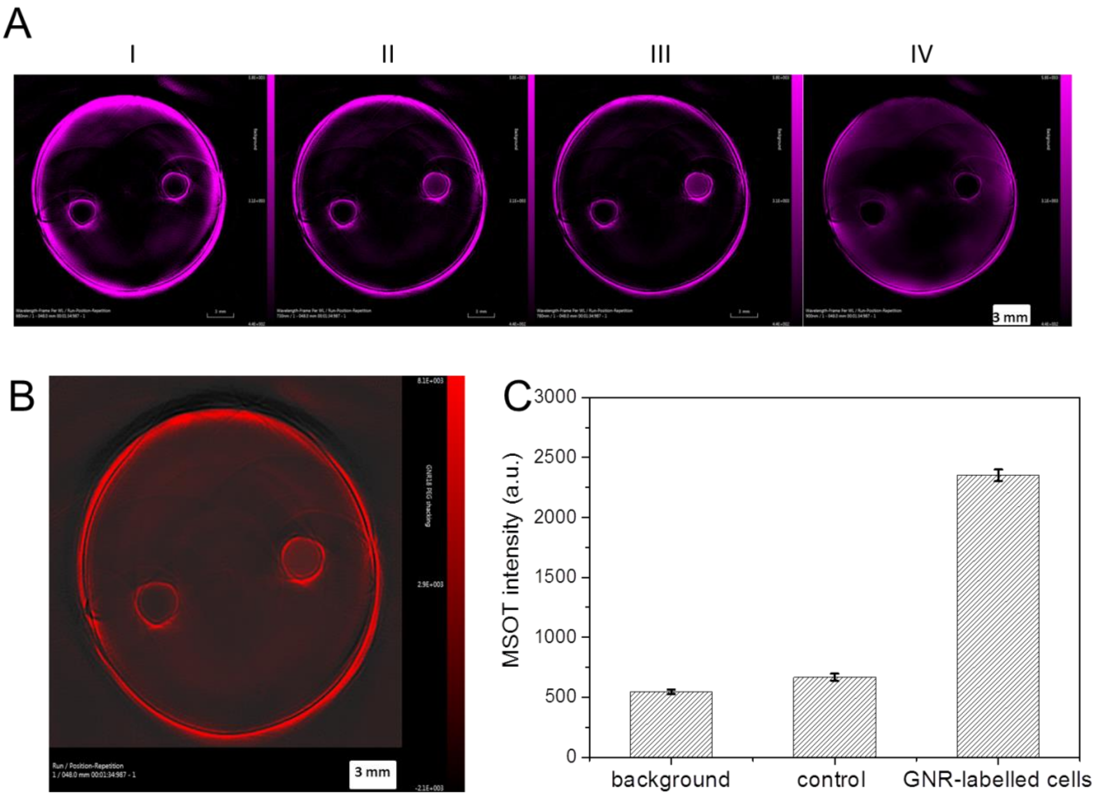

Figure 5.4: A) Mode lineal reconstruction of PEG-COOH GNRs labelled mesenchymal cells. Cross section phantom at different wavelengths I) 690 nm II) 730 nm III) 780nm IV) 900 nm. Colour scale from 4.4 x10^2 to 5.8 x10^3 MSOT units **B) Multispectral reconstruction of PEG-COOH GNRs labelled mesenchymal cells.** Lineal regression method was used here. Colour scale from 2.1 x10^3 to 8.1 x10^3 **C) MSOT intensities of the multispectral reconstruction** in arbitrary units of background, unlabelled cells used as control and PEG-COOH GNRs labelled mesenchymal cells.

5.4.2 Imaging of ZGO-labelled cells by Luminescence Imaging

Results obtained with cells labelled with ZGO:Cr NPs were presented and discussed in chapter 4.

5.5 *In vivo* Imaging after Subcutaneous injection of labelled cells

5.5.1 Cells labelled with GNRs

GNRs-labelled cells were diluted in PBS to obtain 6 million, 2 million and 1 million cells. 100 μ*L* of each sample, including 2 million unlabelled cells used as control, were subcutaneously injected in a CD1 mouse. The animal was irradiated with pulsed light ranging from 680nm to 900 nm in 5 nm wavelengths steps. Figure 5.5 is a good example of the main advantages of MSOT imaging: it provided functional imaging allowing the detection of a specific optical signature (GNRs in our case), and the spatial resolution was much better than classic optical-based imaging technologies, enabling anatomical imaging. For example, here organs such as kidneys and spinal cord were easily imaged.

Multispectral analysis allowed the detection and quantification of GNR-labelled cells and effectively avoids the overlap between target probe and signal coming from endogenous absorbers in internal organs as figure 5.5 illustrates. Only the injection sites where labelled cells were implanted had a photoacoustic spectrum similar to our GNRs. Therefore, after applying the multispectral approach, the signal was localized in the injections sites and not in other regions such as spinal cord vessels, even they had strong photoacoustic signal (but at different wavelengths)

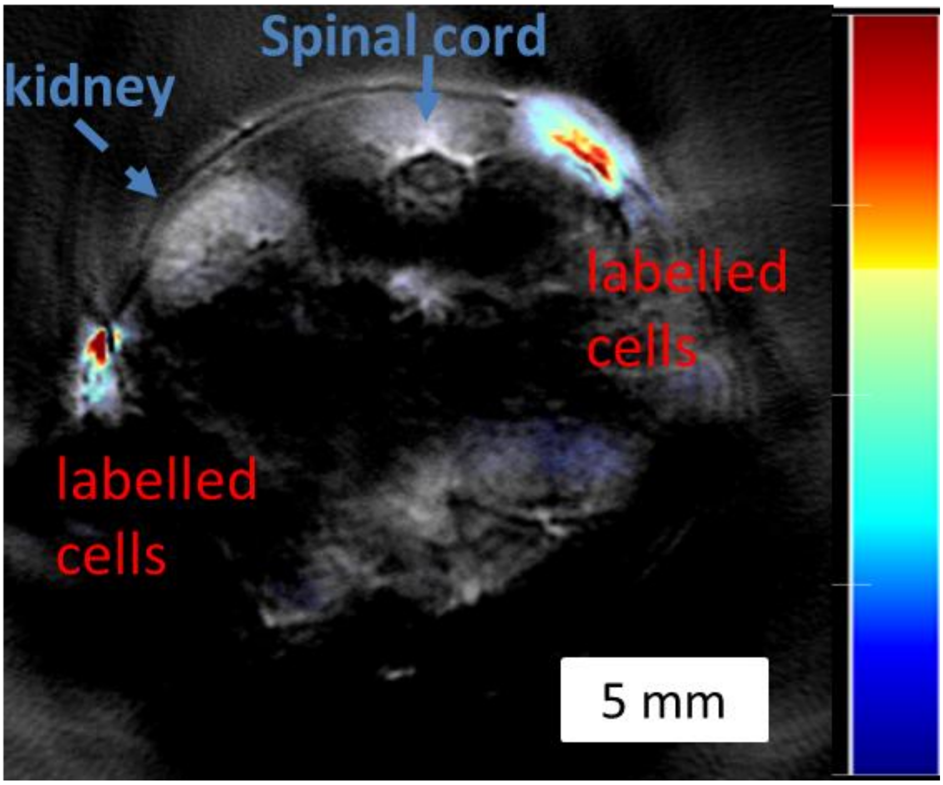

Figure 5.5: *In vivo* imaging of subcutaneously injected MSCs labelled with GNRs. Cross-section of the flank of the mouse showing 2 injection sites and some anatomical details such as left kidney and spinal cord. Colour scale from 4.5 x10^3 to 1.5 x10^4 MSOT units. Background image corresponds to 900 nm.

MSOT intensity is proportional to the concentration of GNRs (or number of GNRs per voxel). Figure 5.6 shows how the intensity in the region of interest increased on the positions where cells had been implanted. As expected the intensity was bigger as the number of cells increased. Since cell clusters had different volumes, area under the curve provided a better approximate estimation of the total intensity. Hence, the 1 million cells cluster had an AUC = 16175 a.u. and the 2 million cells cluster had an AUC = 31045 (calculated with the integration tool in OriginPro 2016, background intensity was chosen to close the area to be measured). In the case of the 6 million, AUC was lower than one would expect (AUC = 60600). The explanation is that the intensity was saturated for many voxels in this condition, thus the mean intensity was underestimated.

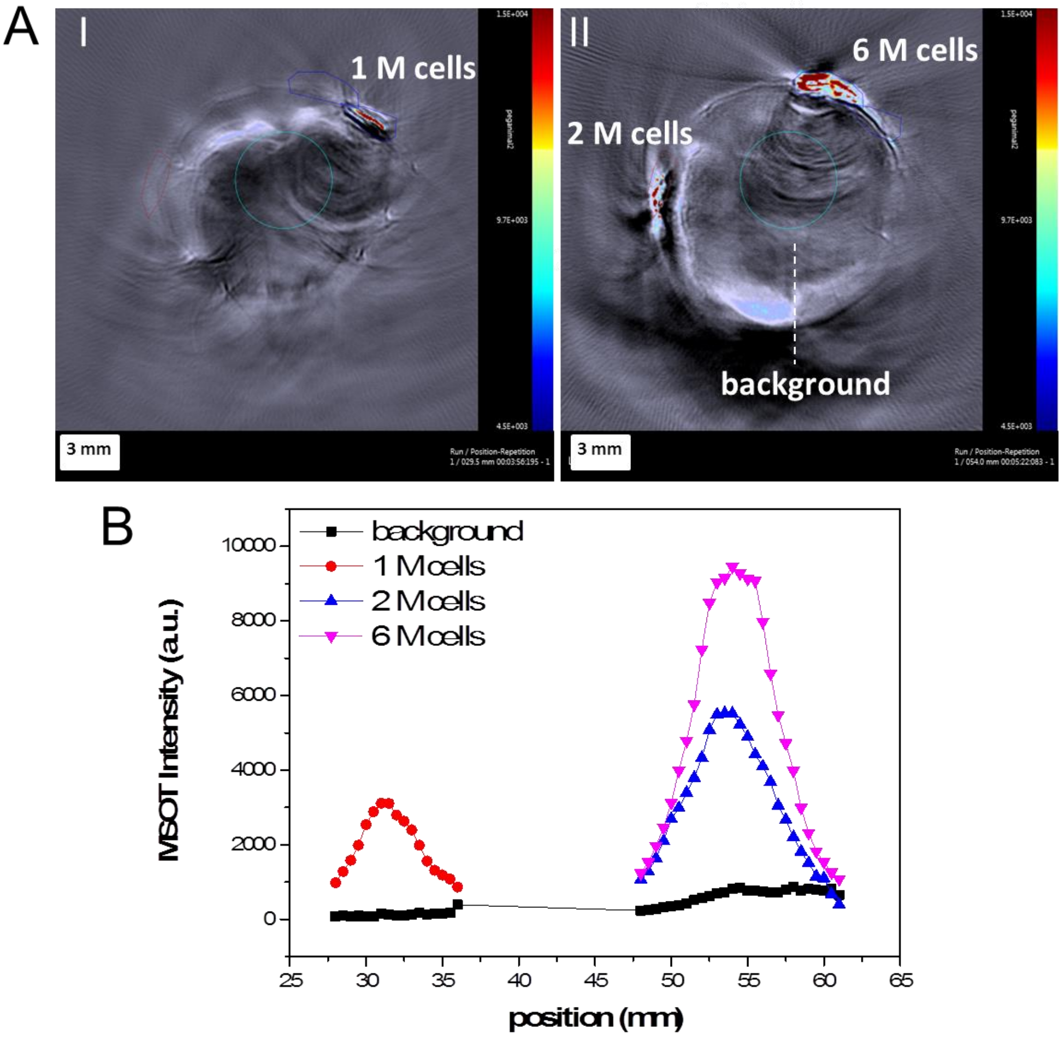

Figure 5.6: A) Multispectral reconstruction of cross section of a mouse first day after subcutaneous injection, showing 1 Million labelled cells (I) 2 and 6 Million labelled cells (II). Colour scale from 4.5 x10^3 to 1.5 x10^4 MSOT units B) MSOT Intensity given in arbitrary units of the different injection sites. The intensity represents the mean pixel intensity of the regions of interest selected for analysis.

We follow up the evolution of the different cell clusters for 19 days by MSOT (Figure 5.7) and bioluminescence (Figure 5.8). 3D maximum MSOT intensity projections provided additional information of the labelled cells distribution in the 3 axes. Cells were monitored without problems up to 19 days with MSOT. At that time intensity was still higher than background but decreased considerably. Interestingly, in bioluminescence imaging (Figure 5.8) it was observed an exponential growth of cells after 12 days. Thus, it is very likely that GNRs concentration per cell decreased as cell clusters grew, which was translated in a decrease in MSOT intensity. Other factors such as cell death and clearance of their content or GNRs aggregation in cell vesicles may also account for that decrease of intensity. It must be also noted that bioluminescence intensity, which is proportional to the expression of luciferase and therefore to the number of cells, was the same for control cells and GNR-labelled cells, which confirmed the lack of cytotoxicity of GNRs.

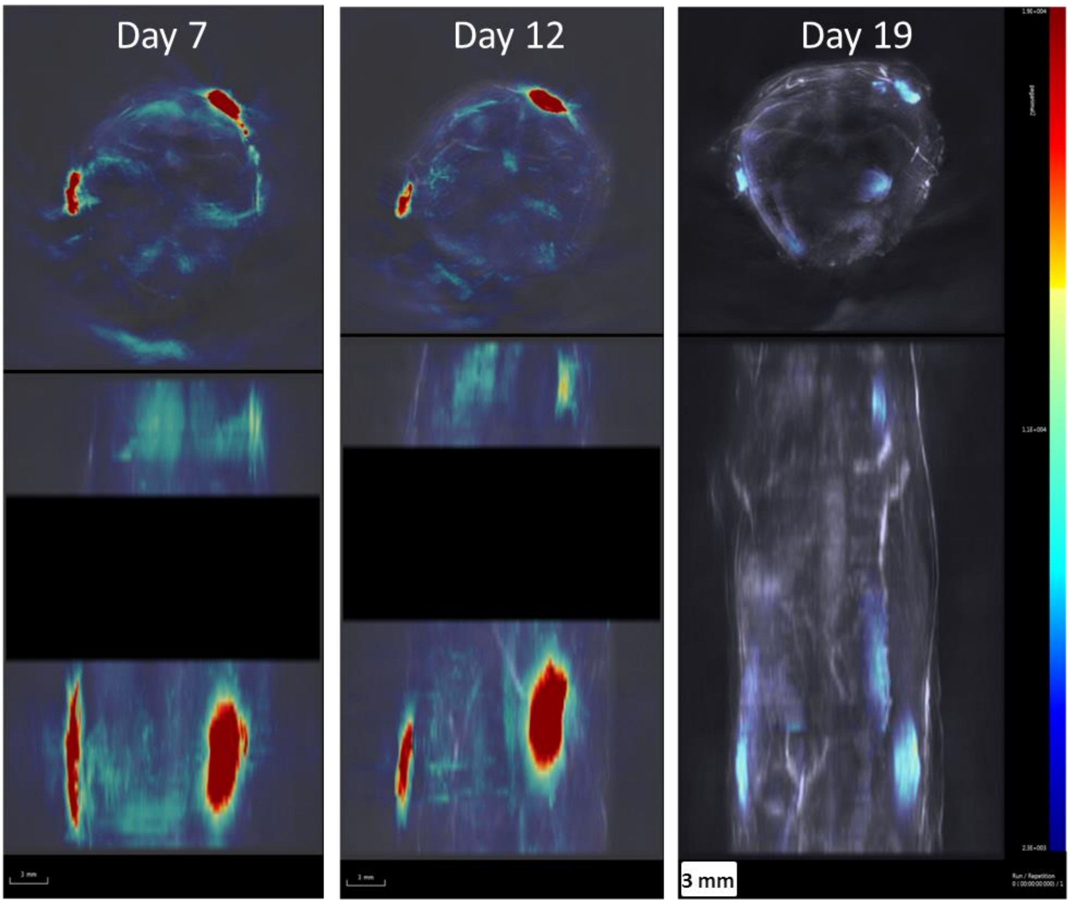

Figure 5.7: Maximum intensity 3D projection at 7th, 12th and 19th day after injection. x-y planes (top row), and x-z planes (bottom row) gives an idea of the thickness and length of the different cell clusters. Note that black regions correspond to regions of the flank without implanted cells that were not imaged for time reasons.

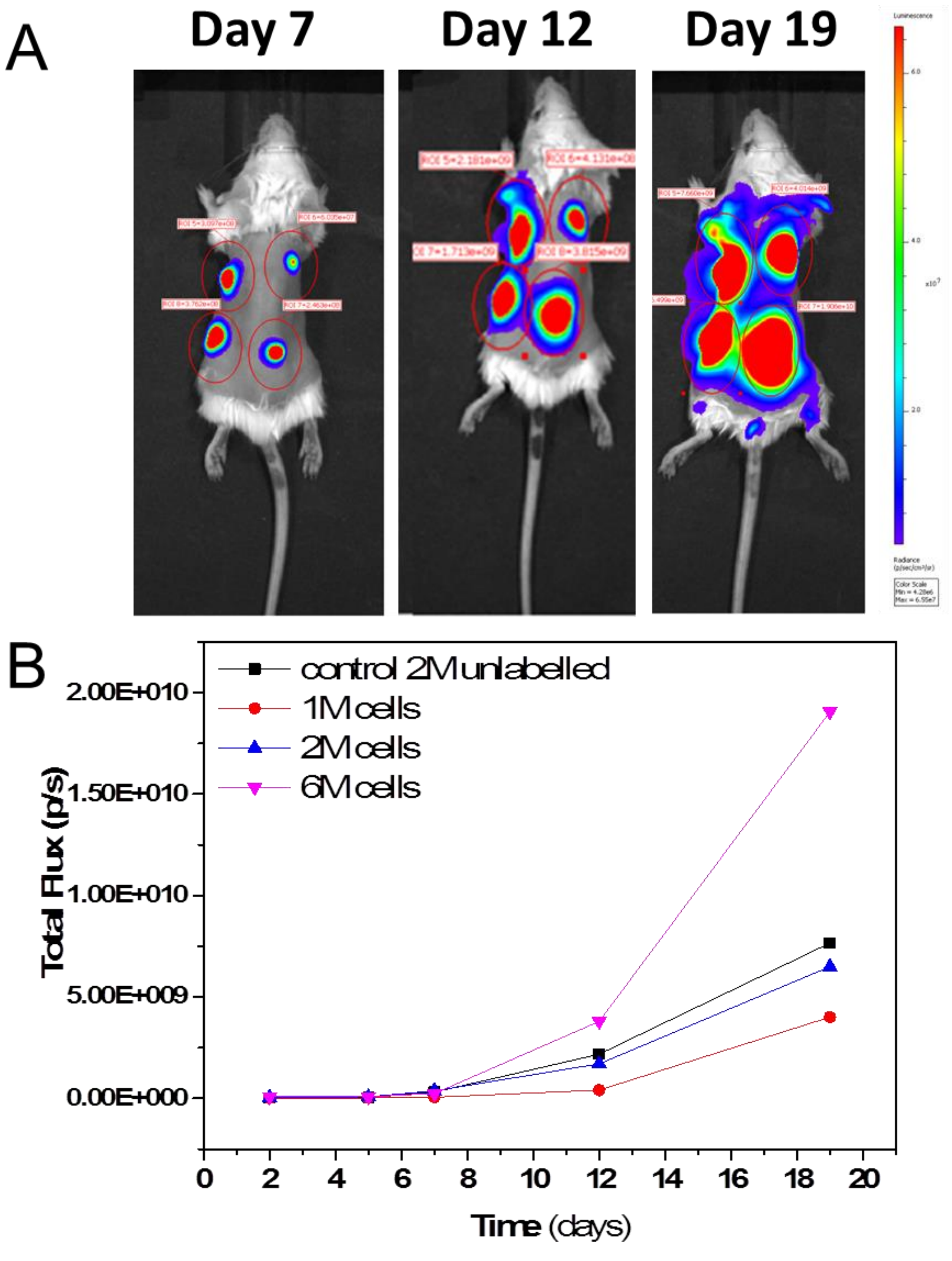

Figure 5.8: Bioluminescence imaging of different number of cells injected subcutaneously. A) Optical imaging pictures signal expressed in radiance (photons/sec/cm^2/sr) of 2 million unlabelled cells (top left flank), 1 Million cells (top right flank), 2 Million labelled cells (bottom left flank) and 6 million labelled cells (bottom right flank). Colour scale from 4.28 × 10^6 to 6.55 × 10^7 p/sec/cm^2/sr B) Luminescence intensity increase with time.

5.5.2 Cells labelled with GNRs and ZGO

For studying the effect of the dual labelling *in vivo* 7.5×10^5 cells were subcutaneously injected at four different positions into the flank: A control (i.e. unlabelled cells) was injected into the top left flank, cells labelled with ZGO:Cr into the top right, GNRs-labelled cells into the bottom left and cells labelled with ZGO:Cr and GNRs into the bottom right. Mouse was imaged by MSOT and optical imaging (IVIS Spectrum System) 3 hours after injection

5.5.2.1 Optical Imaging: Persistent Luminescence Imaging and BLI

After injection of labelled cells, the whole mouse was irradiated with a white LED lamp for 5 minutes before the mouse was set in the imaging chamber and 3 sequential images acquired for 2 minutes each (Figure 5.9 left). As expected, signal was observed only in the two sites where cells contained ZGO:Cr NPs. These sites correspond to the ZGO:Cr labelled cells and dual labelling. As seen for *in vitro* studies (Chapter 4), the presence of GNRs in the dual labelled cells had an effect in decreasing the intensity of the luminescent signal. As explained, this was most likely due to reabsorption of the light emitted by GNRs. In addition, the decay in intensity with time of ZGO-labelled cells is in agreement with what was observed with NPs in solution. This is a clear prove that ZGO:Cr NPs preserve their optical properties after cell uptake and subsequent subcutaneous injection of labelled cells.

To confirm viability of cells labelled with the different strategy, the mouse was also imaged with BLI (Figure 5.9 right). As explained before, chemiluminenscence resulting from the biochemical reaction between luciferase (expressed by the cell line) and its natural substrate luciferin is directly proportional to the number of living cells. As expected from our previous *in vitro* studies, viability was not compromised with any of the treatments.

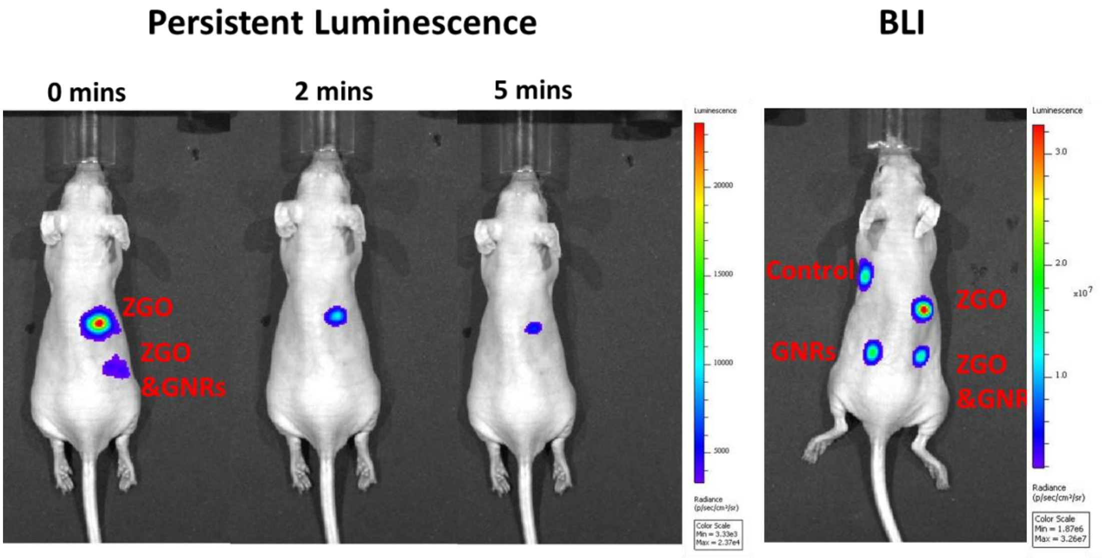

Figure 5.9: Optical Imaging of a whole mouse injected with MSCs labelled with 3 different strategies. Left picture shows the persistent luminescent imaging of the same animal measured at different time points after LED light activation. Right picture shows the bioluminescence imaging of the same mouse after Luciferine injection. Colour scale from 3.33×10^3 to 2.37×10^4 p/sec/cm^2/sr (left) and from 1.87×10^6 to 3.26×10^7 p/sec/cm^2/sr.

ROI	PL Intensity in Total Flux (p/sec)
ZGO-labelled cells	1.22×10^5
ZGO & GNRs-labelled cells	5.07×10^4
Background	2.23×10^4

Table 5.1: PL intensities of the different region of interests (ROIs) expressed in total flux (p/s)

5.5.2.2 Photoacoustic Imaging

MSOT was measured 30 min after the subcutaneous injection of cells. The whole mouse flank was scanned longitudinally with 1 mm steps and a wavelength range between 660 and 1100 nm for every step. Water tank of the instrument was filled with heavy water to minimize absorption at longer wavelengths. As explained above, MSOT relies on the ultrasounds produced after absorption of light pulses. In addition, spectral information of the images can be achieved by processing the information of the images obtained at the different wavelengths. For that purpose, different algorithms can be used to find the components of interest in MSOT images. Here we used 2 of them which are available in the software provided by MSOT manufacturer (iThera viewMSOT v6.2). The first one is the linear regression algorithm which takes into account changes on the intensity at the different wavelengths. Therefore, it emphasises the increases on intensity respect to the background. On the other hand, the guided ICA gives more value to the fitting spectral information of a pixel with a known spectrum. Normally, linear regression works better with high absorbance contrast agents whilst guided ICA works better with slight changes in intensity produced by a known spectrum. In our case, the optical properties were greatly preserved for cells labelled with GNRs and ZGO, whilst plasmon coupling and consequently change in the optical properties occurred for cells labelled only with GNRs as we have explained on chapter 4. Therefore, guided ICA resolved better the condition where spectrum was preserved. On the other hand, both conditions were resolved when linear regression was applied due to the large increase on photoacoustic intensity in both cases (Figure 5.10). Obviously, conditions without GNRs (i.e. control cells and ZGO-labelled cells) did not produce any MSOT signal. GNR-labelled cells were injected into the bottom left of the mouse flank and GNR+ZGO:Cr NPs-labelled cells into the bottom right of the mouse flank. Figure 5.10 shows a cross-section of the part of the flank where cells were injected (top row) and maximum intensity projection of the whole flank (bottom row). Left column shows the analysis after applying a linear regression algorithm for multispectral processing, whilst on the right the algorithm used is guided ICA.

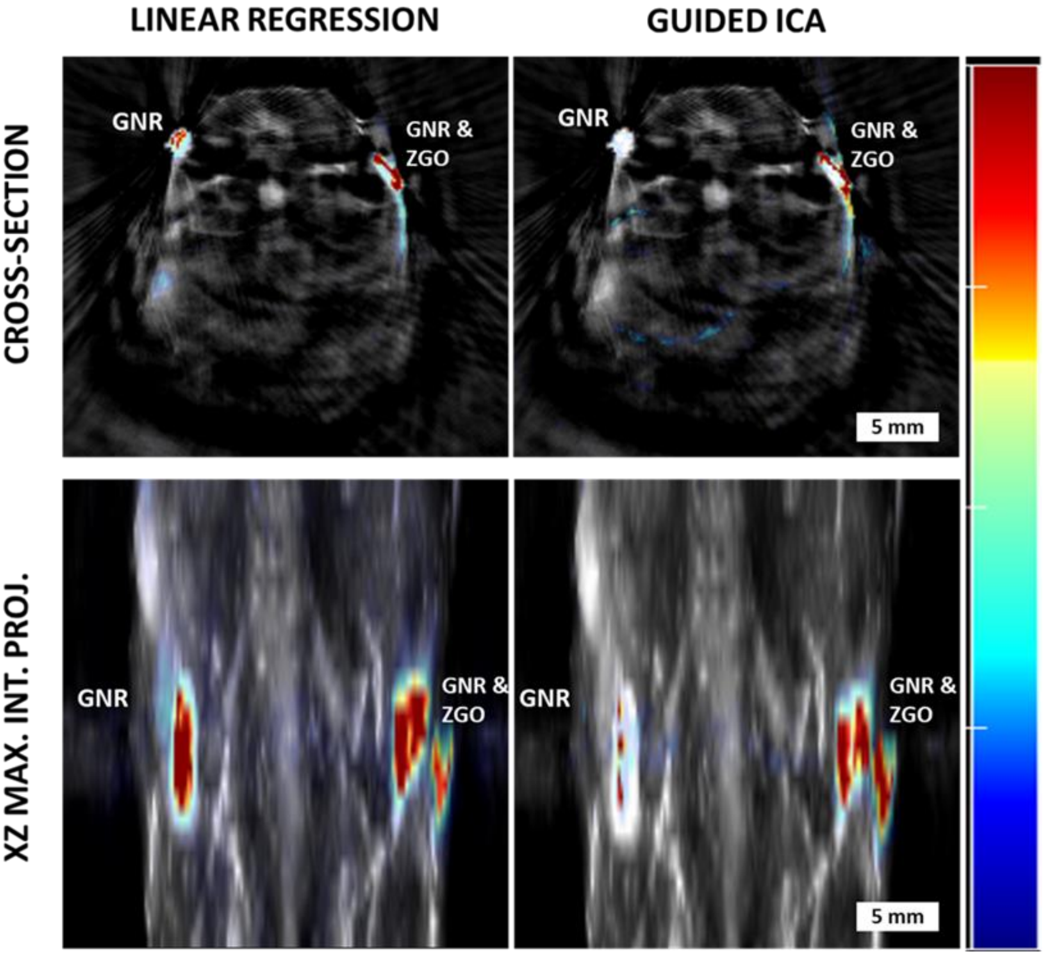

Figure 5.10: MSOT imaging of a mouse after subcutaneous injection of MSCs. Only cells with GNRs produced a MSOT signal. The differences between multispectral reconstructions algorithms are observed here. Colour scales are 1.3 x10^5 to 9.9 x 10^5 for linear regression and 1.8 to 17 for guided ICA. Note that this units are arbitrarily generated after resolving the algorithms and they do not have any physical value.

5.6. Systemic biodistribution of labelled cells

MSCs were incubated with NPs for 24 hours (2mg ZGO:Cr, GNRs at O.D. = 4.8 and a mixture of both NPs). 1.5 million labelled cells were injected *via* intracardiac injection. Mice were imaged 3 hours after injection. Contrarily to subcutaneous injection of cells, where cells were localised in the injection point, cell distribution after systemic administration was much broader, which made it extremely challenging to follow. It must be noted here that cells were administered via ultrasound-guided intracardiac (IC) injection into the left ventricle. Left ventricle administration was chosen for cells to enter the arterial circulation rather than the venous. This allows cells to pass through all organs before returning to the right ventricle and subsequently lungs, where they become sequestered in the pulmonary microvasculature. [35,36]

The imaging routine we used here was as follows: MSOT scan before IC injection, IC injection of cells, MSOT scan after injection of cells, illumination of the animal with a LED light, IVIS imaging, intraperitoneal administration of D-luciferin, 15 min waiting, IVIS imaging.

As we have shown in another work, cells accumulate preferentially in brain capillaries, kidneys, and spinal cord after intracardiac injection.[17] Thus, we will focus on these regions to show our results. Similar cell distribution after IC injection has also been reported previously by other groups using different bioimaging techniques.[37]

5.6.1 Photoacoustic imaging.

5.6.1.1 GNRs labelled cells after systemic administration

As we explained above, optical signature of GNRs was not preserved for this condition. Therefore, the best multispectral approach to try to detect cells labelled only with GNRs was linear regression. Unfortunately, no differences were observed before and after injection of GNR-labelled cells (Figure 5.11). We show here only the kidneys region, but same analysis thorough the animal did not give any significant increase in any region respect to the same animal before injection of cells.

This was not surprising since we have already seen the negative effects of GNRs packing in cell vesicles had on their optical properties. Moreover, cells were expected to have a broad distribution after systemic administration. Therefore a more sensitive approach would have been required for detection. A very different scenario occurred when GNRs were co-incubated with ZGO NPs, we have seen in the previous chapter that optical properties of GNRs were maintained in this condition thanks to the physical separation of GNRs facilitated by ZGO NPs. Results are exposed in the next section

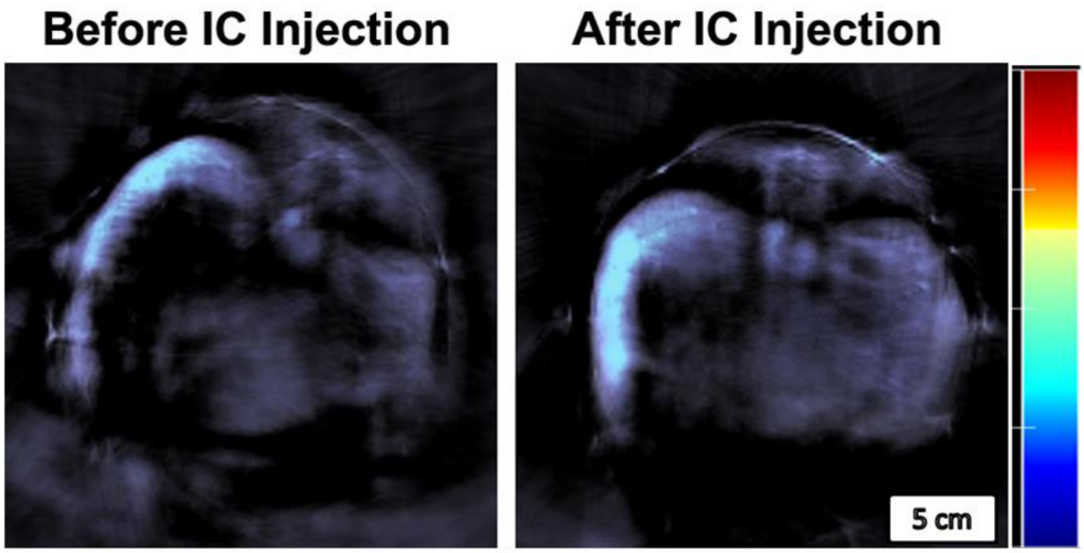

Figure 5.11: MSOT imaging following systemic administration of GNR labelled cells. Scans taken before and after injection of 1.5 × 10^6 labelled-MSCs are shown. Guided ICA multispectral reconstruction was applied. Colour scale from 0 to 6.2 x10^5 MSOT units. Unfortunately, cells could not be monitored using this strategy.

5.6.1.2 GNRs + ZGO labelled cells after systemic administration

A guided ICA multispectral reconstruction was applied here. We have observed that when spectrum is preserved, this approach is able to fit slight changes of photoacoustic intensity fitting with the spectrum of interest, which makes it more suitable when great sensitivity is required, as it is the case due to the broad distribution of cells. In addition, a pre-scan of the animal before receiving the cells was performed to use it as a kind of a baseline to discard false positives, i.e. regions with an endogenous absorption similar to our GNRs.

This was observed, for example, in the region marked with a white circle on Figure 5.12. A MSOT signal was detected after IC injection, but it was also present before IC injection, which indicates a false positive. This region corresponds to the intestines, we noticed in previous experiments that food contained some pigments which resulted in an increase of the signal in similar regions of the spectra than the GNRs used here. Note also that regions with high photoacoustic intensity such as the spleen do not produce any signal after multispectral processing since its optical spectra is quite different to our GNRs. This fact is illustrative of the importance of a multispectral approach to gain sensitivity in molecular imaging.

Taking into account the increase of signal that was seen only after IC injection, we were able to clearly detect cells in kidneys and in the spinal cord, and a slight increase in the brain region, which is indicative of cells being present there. As we explained above, lungs cannot be imaged with techniques based on photoacoustics. It is also observed in this experiment, that MSOT enabled localisation of cells with a much better spatial resolution than bioluminescence, enabling sub-organ localisation, which made possible to precisely localise signals in certain regions such as spinal cord, which would not be possible with fluorescence or bioluminescence imaging.

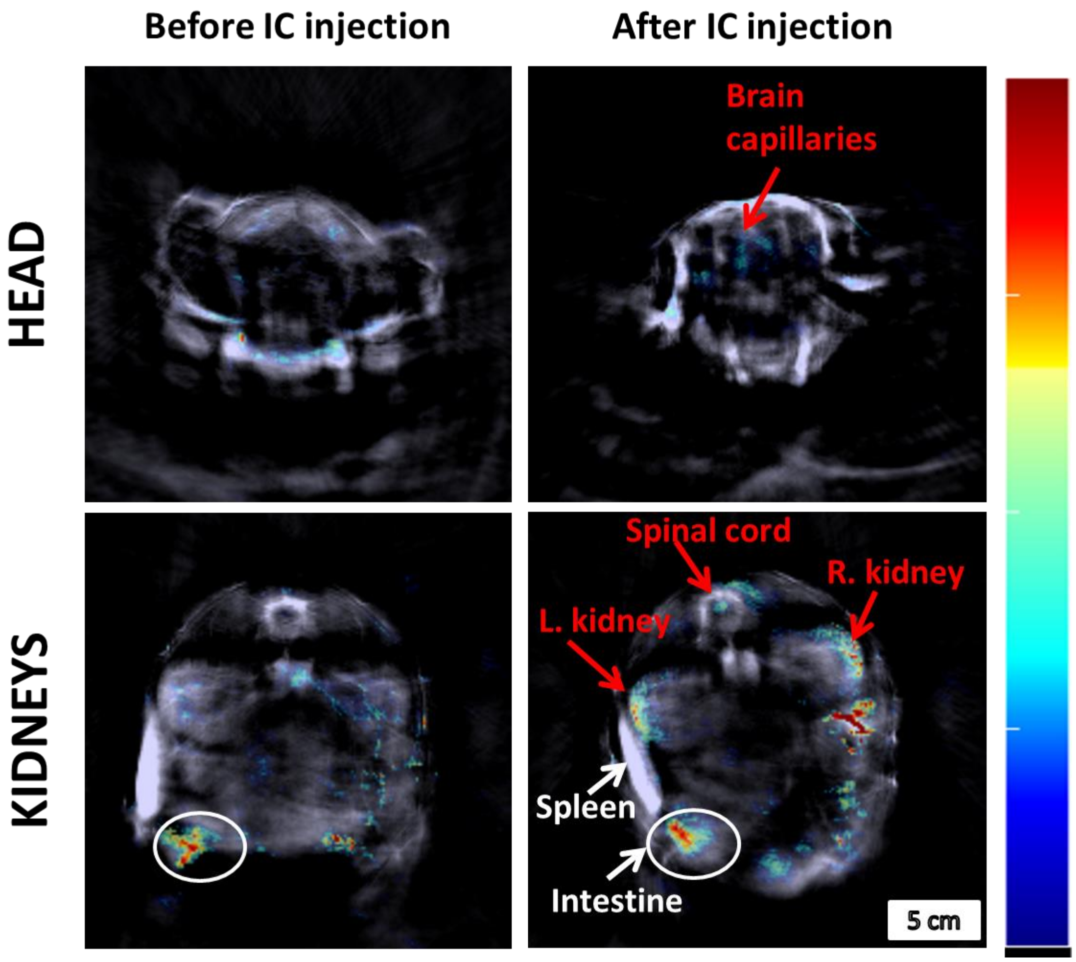

Figure 5.12: MSOT imaging following systemic administration of GNR & ZGO-labelled cells. Cross-section images of relevant areas before and after intracardiac administration of cells. Cross-section of the head is shown in the top row, whilst cross-section of the abdominal region where kidneys are located is shown in the bottom row. Guided ICA reconstruction is applied. Colour scale from 1.04 to 8.05 MSOT units.

Distribution of cells could not be determined when GNRs absorption band was much broader and less intense due to the strong plasmon coupling produced when cells were labelled only with GNRs (Fig 5.11). This was an interesting observation for us. ZGO:Cr NPs are more abundant than GNRs in cell's endosomes, enabling those GNRs to be well separated and consequently, no plasmon coupling was observed, increasing the efficiency of photoacoustic detection. This means that combining GNRs with an excess of other nanomaterials that do not have absorption in the same region is a good strategy to avoid the loss of optical properties following agglomeration inside cell endosomes and therefore to maximize sensitivity for optical detection. We also reported in another work that silica coating is very efficient in maintaining gold cores separated enough to avoid plasmon coupling inside endosomes[38]. However, one may find it not feasible for some applications (e.g. when GNRs functionalised with a specific molecule are needed) so combination with inert, transparent NPs would be an alternative approach to preserve GNRs optical signature in these cases. We used here ZGO:Cr, but other nanomaterials such as silica, TiO2, etc. could be employed for this purpose.

5.6.2 Optical imaging of ZGO labelled cells

1.5×10^6 MSCs labelled with 2 mg/mL of ZGO:Cr were injected systemically as explained above. Imaging measurement were performed 3 hours after the injection. As a control, an untreated mouse (i.e. no injection) was exposed to the same experimental condition as the treated one with labelled cells (Figure 5.13). Images were taken before and after excitation with LED light of the whole animal for 5 minutes. The images showed a signal in the head in both animals. Moreover, there is no clear difference between the control and the treated animal. This reveals that this signal was not coming from the ZGOs but from other source that was activated by light as well. Although luminescence background is less known than auto-fluorescence, it is equally relevant to avoid misinterpretations of imaging data. This spontaneous luminescence background has previously been related to animal diet.[39] The authors of this work systematically studied the spontaneous luminescence of food pellets and of Nu/Nu mice after light exposure. They concluded that the background was very likely to be due to the persistent luminescence of some molecules present in the food. They finally advise that in order to minimize problems related to spontaneous luminescence, food need to be studied before animal experiments and choose the type of food with a lower PL.[39] It was impossible for us to do a last minute change of diet because a modification of the project licence would have been required and approval from UK home office granted. Thus, we were forced to leave this test for a future experiment.

Note also that condition of ZGO + GNRs would have resulted in lower signal due to the inner-filter effect of GNRs.

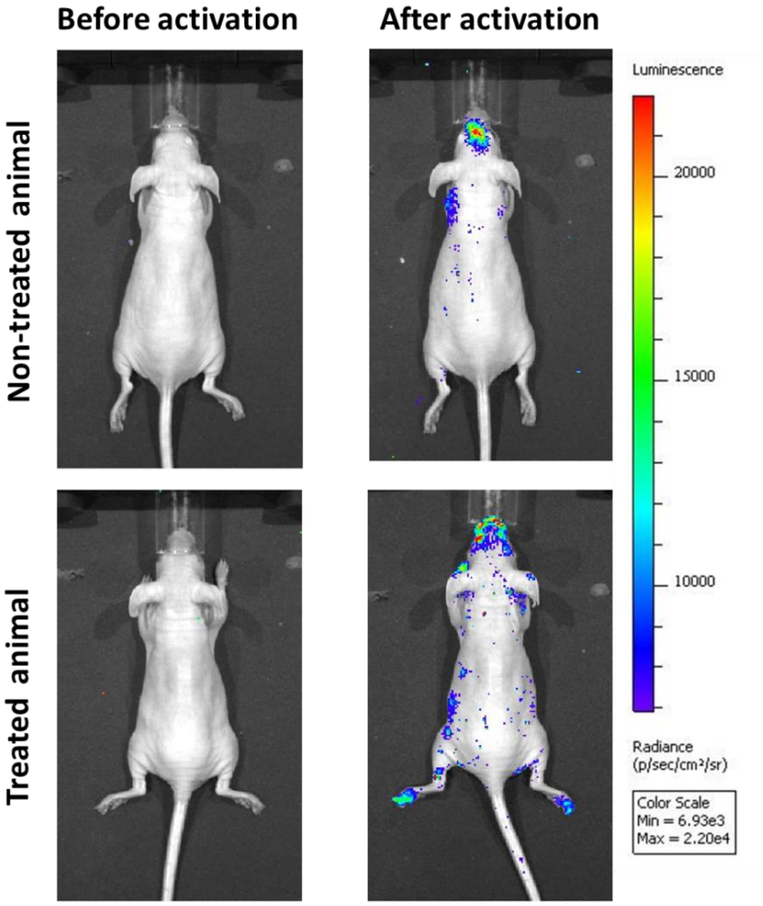

Figure 5.13 *In vivo* optical imaging of mouse injected with ZGO-labelled cells. Images were acquired for 2 minutes before and after excitation with a white LED lamp for 5 minutes 3 hours after intra-cardiac injection of 1.5×10^6 labelled cells. Colour scale from 6.93×10^3 to 2.20×10^4 p/sec/cm^2/sr.

5.5.2.1 Ex vivo Persistent luminescence imaging of dual labelled cells

The *ex vivo* biodistrubution of dual-labelled cells was assessed by imaging the persistent luminescence of main organs (i.e. liver, lungs brain, spleen, heart and kidneys). For this, the animal was sacrificed 4 hours after injection and organs were fixed with PFA and left in PBS for 24 hours, allowing any residual bioluminescence signal from luciferase to be extinguished. The half-life of luciferase in mammalian cells was reported to be approximately 2 hours.[40] Imaging of organs was performed before and after excitation by white LED lamp. Persistence luminescence, associated with ZGO:Cr NPs was found in the liver, the kidneys and the brain (Figure 5.14), showing that cells accumulate in these organs after IC injection. This is in agreement with the *in vivo* imaging obtained by bioluminescence and MSOT. These data show that ZGO:Cr NPs are suitable probes for the study of *ex-vivo* monitoring of labelled cells, which for example would enable their use as tools for *ex vivo* microscopy studies.

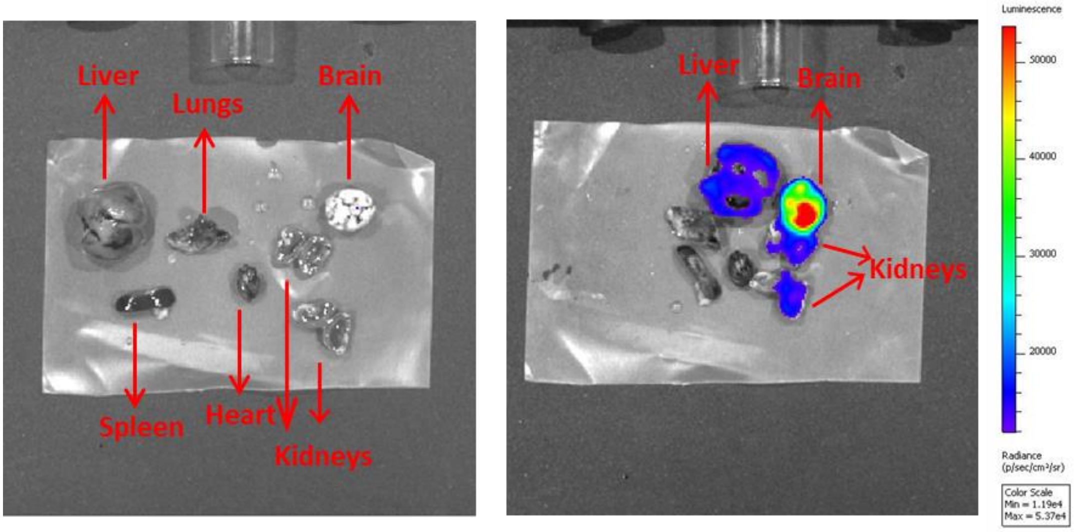

Figure 5.14: Ex vivo PL imaging of main organs after injection of ZGO&GNRs labelled cells. Main organs were extracted and imaged for 2 minutes before and after exposure to a white LED lamp for 5 minutes. Note that organs after LED exposure were closer between them to be uniformly irradiated with our LED source. Colour scale is from 1.19×10^4 to 5.37×10^4 p/sec/cm^2/sr.

5.6.3 Bioluminescence Imaging (BLI)

Bioluminescence was used to validate data obtained by MSOT and persistent luminescence. 1.5×10^6 cells were injected *via* intracardiac injection and intraperitoneal injection of D-luciferine was administrated 3 hours later. Whole body imaging was performed 15 minutes after luciferine injection. The results confirmed that MSCs accumulate in the brain region, kidneys and liver (Figure 5.15), in good agreement with the MSOT *in vivo* imaging and persistent luminescence *ex vivo* imaging.

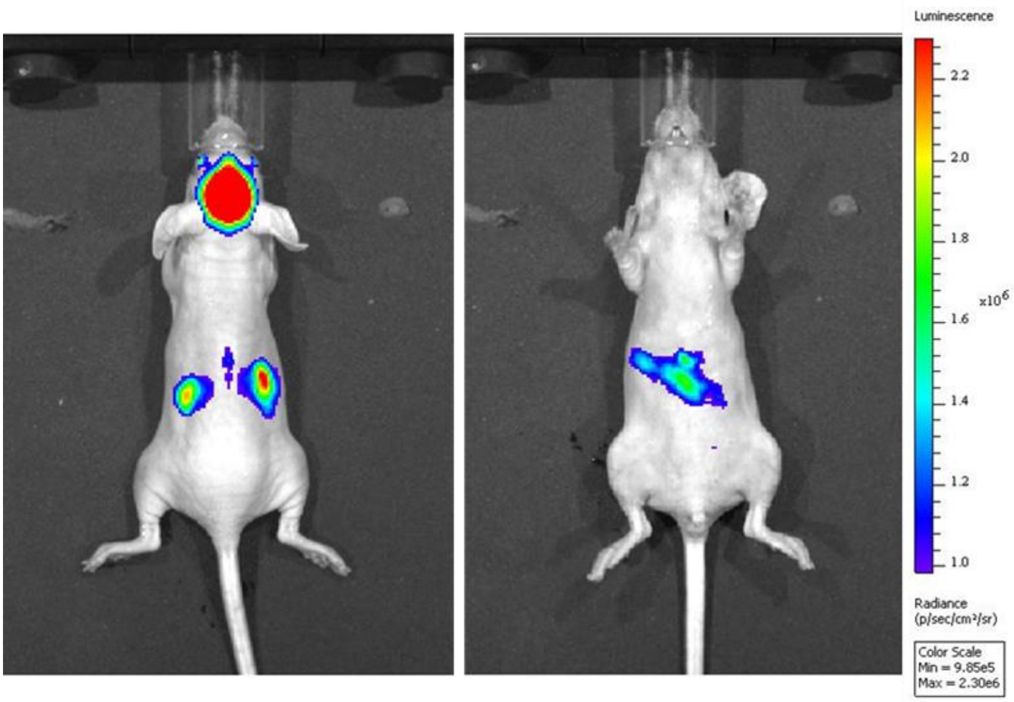

Figure 5.15: *In vivo* cell tracking of cells labelled with GNRs + ZGO by BLI. Results are in agreement with cell accumulation in the brain region, kidneys, spinal cord and liver. Colour scale is from 9.85×10^5 to 2.30×10^6 p/sec/cm^2/sr.

5.7 Conclusions

MSCs labelled with PEG-COOH-GNRs, DMSA-ZGO and co-labelled cells were *in vivo* imaged after subcutaneous and systemic injection. First, the dilution effect was studied with GNRs-labelled cells after subcutaneous injection. The *in vivo* experiments showed that cells were detectable for up to 19 days. Conversely, luciferase-based bioluminescence imaging (BLI) intensity increased with the number of cells indicating that this approach is more appropriate if long-term tumour monitoring is required. In addition, down to 7.5×10^5 GNRs, ZGO and co-labelled cells were imaged by means of MSOT and IVIS spectrum system and all of them resulted in an obvious signal. ZGO NPs were "recharged" inside animals by exposure to a white LED lamp and NIR-light emitted by the lasted for up to 5 min. As expected, the persistent luminescence signal obtained in the presence of GNRs (i.e. co-labelled cells) was lower than when ZGO NPs were labelled independently. This decrease of signal intensity is probably due to absorption of the emitted light by GNRs.

Imaging MSCs after systemic injection was more complicated since cells were distributed along the organism. Detection of persistent luminescence signal coming from ZGO NPs was not possible. This was partially due to the presence of noise from certain food components in the animal's diet. Therefore, persistent luminescence could be only detected in *ex vivo* experiments. Optical imaging measurements of the main organs showed that cells were located in kidneys, liver and brain capillaries. In addition, *in vivo* BLI of systemically injected cells was successfully performed. In this case, bioluminescence offered great sensitivity for cell tracking, showing accumulation of cells in kidneys, brain capillaries and liver.

This was in good agreement with the *ex vivo* imaging. Since cell viability can be monitored by this method, validation of imaging results obtained using NPs was possible.

MSOT imaging was also conducted to track cells after systemic injection. Optical properties of GNRs were improved when the gold cores are separated by co-labelling with ZGOs (see chapter 4, section 4.5.1). For this reason, MSOT signal was higher when cells were co-labelled with both types of NPs than when they were labelled only with GNRs, as subcutaneous experiments showed. Consequently, only co-labelled cells could be tracked after intra-cardiac injection showing that cells accumulated mainly in kidneys, spinal cord and brain capillaries.

5.8 Bibliography

1. Gambhir, S. S. Molecular imaging of cancer with positron emission tomography. *Nat. Rev. Cancer* **2,** 683 (2002).
2. Sosnovik, D. E. *et al.* Molecular MRI Detects Low levels of Cardiomyocyte Apoptosis in a Transgenic Model of Chronic Heart Failure. *Circ. Cardiovasc. Imaging* **2,** 468–475 (2009).
3. Srivastava, A. K. & Bulte, J. W. M. Seeing Stem Cells at Work In Vivo. *Stem Cell Rev. Reports* **10,** 127–144 (2014).
4. Lucignani, G. & Rodriguez-Porcel, M. In vivo imaging for stem cell therapy: new developments and future challenges. *Eur. J. Nucl. Med. Mol. Imaging* **38,** 400–405 (2011).
5. Giepmans, B. N. G., Adams, S. R., Ellisman, M. H. & Tsien, R. Y. The Fluorescent Toolbox for Assessing Protein Location and Function. *Science (80-.).* **312,** 217 LP-224 (2006).

6. Ntziachristos, V., Ripoll, J., Wang, L. V & Weissleder, R. Looking and listening to light: the evolution of whole-body photonic imaging. *Nat. Biotechnol.* **23,** 313 (2005).

7. Arranz, A. & Ripoll, J. Advances in optical imaging for pharmacological studies. *Front. Pharmacol.* **6,** 189 (2015).

8. Massoud, T. F., Massoud, T. F., Gambhir, S. S. & Gambhir, S. S. Molecular imaging in living subjects: seeing fundamental biological processes in a new light. *Genes Dev.* **17,** 545–580 (2003).

9. Achilefu, S. Lighting up Tumors with Receptor-Specific Optical Molecular Probes. *Technol. Cancer Res. Treat.* **3,** 393–409 (2004).

10. Kruger, R. A., Kiser, W. L., Reinecke, D. R., Kruger, G. A. & Miller, K. D. Thermoacoustic Molecular Imaging of Small Animals. *Mol. Imaging* **2,** 15353500200303108 (2003).

11. Emelianov, S. Y., Li, P.-C. & O’Donnell, M. Photoacoustics for molecular imaging and therapy. *Phys. Today* **62,** 34–39 (2009).

12. Wang, S., Lin, J., Wang, T., Chen, X. & Huang, P. Recent Advances in Photoacoustic Imaging for Deep-Tissue Biomedical Applications. *Theranostics* **6,** 2394–2413 (2016).

13. Wang, L. V & Hu, S. Photoacoustic Tomography: In Vivo Imaging from Organelles to Organs. *Science* **335,** 1458–1462 (2012).

14. Ntziachristos, V. & Razansky, D. Molecular Imaging by Means of Multispectral Optoacoustic Tomography (MSOT). *Chem. Rev.* **110,** 2783–2794 (2010).

15. Taruttis, A., Herzog, E., Razansky, D. & Ntziachristos, V. Real-time imaging of cardiovascular dynamics and circulating gold nanorods with multispectral optoacoustic tomography. *Opt. Express* **18,** 19592–19602 (2010).

16. Matthews, T. P., Li, L., Wang, L. V. & Anastasio, M. A. Compensation for air voids in photoacoustic computed tomography image reconstruction. in *Progress in Biomedical Optics and Imaging - Proceedings of SPIE* **9708,**

(2016).

17. Comenge, J. *et al.* Multimodal cell tracking from systemic administration to tumour growth by combining gold nanorods and reporter genes. *bioRxiv* (2017).

18. Willets, K. A. & Van Duyne, R. P. Localized Surface Plasmon Resonance Spectroscopy and Sensing. *Annu. Rev. Phys. Chem.* **58,** 267–297 (2007).

19. Jain, P. K., Lee, K. S., El-Sayed, I. H. & El-Sayed, M. A. Calculated Absorption and Scattering Properties of Gold Nanoparticles of Different Size, Shape, and Composition: Applications in Biological Imaging and Biomedicine. *J. Phys. Chem. B* **110,** 7238–7248 (2006).

20. Xia, Y. *et al.* Gold Nanocages: From Synthesis to Theranostic Applications. *Acc. Chem. Res.* **44,** 914–924 (2011).

21. Li, W. & Chen, X. Gold nanoparticles for photoacoustic imaging. *Nanomedicine (Lond).* **10,** 299–320 (2015).

22. Deán-Ben, X. L., Fehm, T. F., Ford, S. J., Gottschalk, S. & Razansky, D. Spiral volumetric optoacoustic tomography visualizes multi-scale dynamics in mice. *Light Sci. &Amp; Appl.* **6,** e16247 (2017).

23. Li, Y., Gecevicius, M. & Qiu, J. Long persistent phosphors—from fundamentals to applications. *Chem. Soc. Rev.* (2016). doi:10.1039/C5CS00582E

24. Jain, A., Kumar, A., Dhoble, S. J. & Peshwe, D. R. Persistent luminescence: An insight. *Renew. Sustain. Energy Rev.* (2016). doi:10.1016/j.rser.2016.06.081

25. Maldiney, T. *et al.* Controlling Electron Trap Depth To Enhance Optical Properties of Persistent Luminescence Nanoparticles for In Vivo Imaging. *J. Am. Chem. Soc.* **133,** 11810–11815 (2011).

26. Maldiney, T. *et al.* The in vivo activation of persistent nanophosphors for optical imaging of vascularization, tumours and grafted cells. *Nat. Mater.* **13,** 418–426 (2014).

27. Li, Z. *et al.* Direct aqueous-phase synthesis of sub-10 nm 'luminous pearls' with enhanced in Vivo renewable near-infrared persistent luminescence. *J. Am. Chem. Soc.* **137,** 5304–5307 (2015).

28. von der Haar, K., Lavrentieva, A., Stahl, F., Scheper, T. & Blume, C. Lost signature: progress and failures in in vivo tracking of implanted stem cells. *Appl. Microbiol. Biotechnol.* **99,** 9907–9922 (2015).

29. Akins, E. J. & Dubey, P. Noninvasive Imaging of Cell-Mediated Therapy for Treatment of Cancer. *J. Nucl. Med.* **49,** 180S–195S (2008).

30. Sadikot, R. T. & Blackwell, T. S. Bioluminescence Imaging. *Proc. Am. Thorac. Soc.* **2,** 537–540 (2005).

31. de Almeida, P. E., van Rappard, J. R. M. & Wu, J. C. In vivo bioluminescence for tracking cell fate and function. *Am. J. Physiol. - Hear. Circ. Physiol.* **301,** H663–H671 (2011).

32. Noser, J. A. *et al.* Cyclosporine Increases Human Immunodeficiency Virus Type 1 Vector Transduction of Primary Mouse Cells. *J. Virol.* **80,** 7769–7774 (2006).

33. Morscher, S., Driessen, W. H. P., Claussen, J. & Burton, N. C. Semi-quantitative multispectral optoacoustic tomography (MSOT) for volumetric PK imaging of gastric emptying. *Photoacoustics* **2,** 103–110 (2014).

34. Taruttis, A., Herzog, E., Razansky, D. & Ntziachristos, V. Real-time imaging of cardiovascular dynamics and circulating gold nanorods with multispectral optoacoustic tomography. *Opt. Express* **18,** 19592–19602 (2010).

35. Kean, T. J., Lin, P., Caplan, A. I. & Dennis, J. E. MSCs: Delivery routes and engraftment, cell-targeting strategies, and immune modulation. *Stem Cells International* (2013). doi:10.1155/2013/732742

36. Fischer, U. M. *et al.* Pulmonary Passage is a Major Obstacle for Intravenous Stem Cell Delivery: The Pulmonary First-Pass Effect. *Stem Cells Dev.* **18,** 683–691 (2009).

37. Chris, H. *et al.* In vivo magnetic resonance imaging of single cells in mouse

brain with optical validation. *Magn. Reson. Med.* **55,** 23–29 (2005).

38. Comenge, J. *et al.* Preventing Plasmon Coupling between Gold Nanorods Improves the Sensitivity of Photoacoustic Detection of Labeled Stem Cells in Vivo. *ACS Nano* **10,** 7106–7116 (2016).

39. Boschi, F., Spinelli, A. E., Calderan, L. & Sbarbati, A. Spontaneous Luminescence Background in Living Nu / Nu Mice. **2012,** 5–11 (2012).

40. M., I. J. & V., S. D. Kinetic analysis and modeling of firefly luciferase as a quantitative reporter gene in live mammalian cells. *Biotechnol. Bioeng.* **86,** 827–834 (2004).

Chapter 6

Conclusions and Future work

6.1 Conclusion

GNRs were synthesized by the seed-mediated growth method and the conditions were adjusted to obtain GNRs with an aspect ratio (A.R.) ≈3. The LSPR peak position obtained is around 750 nm, ideal for *in vivo* MSOT imaging since overlaps with the NIR window. As synthesized GNRs were cytotoxic due to the surfactant used in the synthesis (CTAB), which is toxic for the cells at the concentration required to stabilize the GNRs. CTAB was exchanged with poly ethylene glycol (PEG) in order to obtain biocompatible GNRs. In addition, PEGylation of GNRs also resulted in an improvement of colloidal stability. Indeed, PEG-GNRs were stable under the harsh conditions of cell culture medium, with high ionic strength and presence of a variety of molecules including proteins, sugars, etc. A two-step method was developed to modify the surface of GNRs with SH-PEG-COOH. It involved a controlled agglomeration of GNRs in acidic pH to maximize loading, followed by a second step under basic conditions to recover stability. This method allowed the surface modification of the positive CTAB-GNRs with a negative ligand, while solving irreproducibility problems from batch to batch related to the small changes in the purification of CTAB excess and improving ligand loading. SH-PEG-

COOH conferred electrostatic stability to the NPs due to the negative charge of carboxylic acids at physiologic pH. In addition, carboxylic acids can be used as scaffolds for covalent binding of biomolecules or other structures. The conjugation with BSA and TAT peptide was achieved via EDAC/NHS coupling chemistry to form an amide bond between the carboxylic acids on the surface of GNRs and amines in the biomolecules. Colloidal stability was guaranteed thorough the process by controlling the number of carboxylic acids to be activated. The main advantage of this method is the versatility since composites can be built with any structure containing amines, including other contrast agents to form a multi-modal probe.

ZGO NPs were synthesized by a single step hydrothermal approach. These NPs could be "recharged" even inside animals by exposure to a white LED lamp. NIR-light emitted by the contrast agents could be detected for up to 5 min. This enabled an imaging time window, i.e. excitation and emission measurement can be separated in time, reducing the tissue auto-fluorescence and ultimately improving signal-to-noise ratio. Surface of Cr:ZGO was modified with DMSA, achieving a stable coordination bound. DMSA has been used to modify the surface of different NP (GNPs, silver nanoparticles, iron oxide, zinc oxide nanorod arrays and CdSe quantum dots). However, to the best of our knowledge, DMSA has not previously been used to functionalize LPNPs.

Negative surface charge of PEG-COOH-GNRs enabled protein adsorption which increased the colloidal stability in physiological media and favoured uptake by cells, in contrast to its uncharged counterpart. TAT and BSA-GNRs bioconjugates were studied. While the different bioconjugates exhibited different surface charge in aqueous solution, after incubation with cell culture media, the average surface charge shifted to negative in both cases. Adsorption of proteins on the surface of the NPs is the responsible for this. Therefore, to fully understand the NP-cell membrane interactions, physicochemical properties of NPs need to be assessed before and after exposure to physiological environments. Cell uptake of ZGO was significantly increased while maintaining colloidal stability by the conjugation to DMSA.

MSCs were imaged after subcutaneous and systemic injection. For this a multimodal approach was chosen, the high resolution and penetration depth of MSOT were combined with the sensitivity and whole-body imaging that pure optical methods offer. Cells were co-labelled with PEG-COOH-GNRs and DMSA-ZGO. 7.5×10^5 labelled cells were imaged by MSOT and IVIS spectrum system after subcutaneous injection. All conditions tried, i.e. GNRs, ZGO and co-labelled cells, resulted in an obvious signal recorded by both instruments. Persistent luminescence signal recorded with co-labelled cells was lower than when ZGO NPs were labelled independently. This is expected from the mixture of two optically active materials that can interfere with each other optical properties. We believe that this decrease in intensity is very likely to be due to absorption of emitted light by GNRs. GNRs with other optical signature would minimise this effect, however they might not be as optimal for MSOT imaging.

Tracking systemically injected MSCs was far more challenging since cells were distributed along the organism. Persistent luminescence signal of labelled cells was undetectable since the intensity of the background was higher than the luminescent intensity of ZGOs. Certain food components have been reported to be responsible for this unexpected luminescence background. Persistent luminescence was restricted to *ex vivo* imaging. The *ex vivo* optical imaging of the main organs revealed that cells were accumulated in kidneys, liver and brain capillaries while lungs and spleen and heart did not show a significant signal. In addition, co-labelled cells were detected by

MSOT showing that MSCs accumulated mainly in kidneys, spinal cord and brain capillaries. Interestingly, co-labelling preformed much better than GNR-labelled cells in MSOT imaging. Confinement of GNRs in endosomes caused packing of GNRs, which was translated in plasmon coupling and reduction of absorbance intensity. Consequently MSOT intensity was reduced since the technique relies in the absorption of light by probes. Moreover, the flattening of the LSPR band made more difficult the spectral recognition in the presence of endogenous absorbers. When both NPs were incubated simultaneously, ZGOs physically separated GNRs improving like this the optical properties of GNRs in cells (GNRs were physically separated by the more abundant ZGO NPs). These results highlight the importance of checking optical properties of cells after labelling when the application relies on the SPR of GNRs.

For our experiments, we used cells previously modified to express luciferase, which allowed bioluminescence imaging of injected cells. Bioluminescence offers great sensitivity for cell tracking. In addition, cell viability can be monitored. Therefore, it is a good method to validate the results obtained using NPs as contrast agents. Results obtained by BLI showed that cells accumulated in liver, kidneys and brain capillaries being consistent with the PL *ex vivo* imaging and the MSOT *in vivo* imaging. In addition, approaches based on genetic reporters such as luciferase do not suffer from signal dilution after cell division like direct method. While GNRs-labelled cells could only be imaged for up to 19 days, BLI intensity increased with the number of cells. Therefore, this approach would be needed if long-term tumour monitoring was required.

MSOT imaging provided a much higher resolution for *in vivo* imaging than other optical-based methods. However, some organs such as lungs and stomach cannot be imaged by MSOT. Also, presence of endogenous absorbers with similar optical profile could potentially lead to misinterpretations of results. Taking a multimodal approach with a complementary imaging method such as optical imaging helps to overcome these drawbacks. BLI is a well-studied approach, providing less spatial resolution than MSOT, but very good sensitivity. However, this approach cannot be used always. For instance, primary cells have very low transfection efficiency. These cells are a niche for PLNPs. In addition, BLI is obviously restricted to preclinical models due to the need to genetically modify the cells. Thus, although it is still in the early stages, the emerging field of PLNPs has a huge potential to extend the use of luminescence for *in vivo* imaging.

6.2 Future work

The strategy used for binding molecules to PEG-COOH-GNRs can be used with any structure that has amines available. Therefore, this can be used to fabricate bimodal probes with dyes or fluorescent particles. In addition, the binding of ZGO to GNRs could be improved if problems with colloidal stability of APTES-ZGO were solved. However, our calculations indicate that we need several orders of magnitude more ZGO NPs than GNRs. Therefore, it is likely that the bimodal probe would not work for cell labelling while if the bimodal probe was needed for direct injection of probes on the blood torrent, this would be the way forward.

Our observation regarding the effect that DMSA ligand on ZGO surface might have on the enhancement of PL intensity respect to as synthesized ZGO needs to be confirmed. For this monitoring the intensity of luminescence with different number of DMSA molecules would provide more information. Ligand with different polarities could also be used to determine if polarity was the reason of this effect.

Luminescent background in mouse observed in our imaging with ZGO might be reduced if animals are fed with appropriate food for persistent luminescence measurements. This might allow imaging of ZGO-labelled cells after systemic injection too. For this, the project licence for animal experiments would need to be updated. To minimize the absorption of PL light by GNRs, GNRs absorbing at longer wavelengths in the NIR, around 850 nm, could be used to reduce the overlap of absorption. Use of cells modified to express luciferase allowed the validation of our results with bioluminescence imaging, which is an established method for preclinical imaging. Our system would make possible further validations and analysis. For example, histology exploration would be possible since gold nanoparticles offers good contrast in microscopy techniques such as photothermal microscopy. Moreover, luminescence signal of ZGO could be used also in confocal microscopy with the appropriate filters, getting rid of autofluorescence in tissues. Obviously, the metallic nature of both NPs would add contrast to electronic microscopy or would enable quantification by means of ICP-MS. In terms of multimodal imaging, other techniques such as X-ray micro-CT could be added for further exploration. Gold is a high atomic number element and therefore shows a good contrast for X-Ray based imaging. This technique offers a good resolution and no penetration depth limitations.

Finally, the use of long persistence luminescence nanoparticles for biological applications is an emerging field with many potential applications beyond preclinical imaging such as bio-detection, image guided surgery, labels for electronic microscopy and confocal microscopy, and theranostics amongst others. Advances in synthetic routes, functionalization strategies, better understanding on how luminescence can be tuned, or study cell-NPs interactions might therefore contribute to extend their uses.